University of Groningen

Enlightenment of the Universe

Aykutalp, Aycin

IMPORTANT NOTE: You are advised to consult the publisher's version (publisher's PDF) if you wish to cite from it. Please check the document version below.

Document Version
Publisher's PDF, also known as Version of record

Publication date:
2012

Citation for published version (APA):
Aykutalp, A. (2012). *Enlightenment of the Universe: the Interplay Between Dark Energy. the First Stars, and Black Holes.* Groningen: s.n.

rijksuniversiteit
groningen

Enlightenment of the Universe: the Interplay Between Dark Energy, the First Stars and Black Holes

Proefschrift

ter verkrijging van het doctoraat in de
Wiskunde en Natuurwetenschappen
aan de Rijksuniversiteit Groningen
op gezag van de
Rector Magnificus, dr. E. Sterken,
in het openbaar te verdedigen op
vrijdag 21 september 2012
om 14.30 uur

door

Ayçin Aykutalp

geboren op 14 december 1980
te Istanbul, Turkije

Promotor: Prof. dr. M. Spaans

Beoordelingscommissie: Prof. dr. A. Ferrara
Prof. dr. K. Wada
Prof. dr. J. H. Wise

"Ubi dubium ibi libertas"

– Latin proverb

Contents

Introduction

<div style="text-align: right">
1
</div>

"The evolution of the world can be compared to a display of fireworks that has just ended: some few red wisps, ashes, and smoke. Standing on a well-chilled cinder, we see the slow fading of suns, and we try to recall the vanished brilliance of the origin of the worlds."

Georges Lemaître, 1931

1.1 The Hot Big Bang Model and Structure Formation in ΛCDM

"I could be bounded in a nutshell, and count myself a king of infinite space", said William Shakespeare. One of the most striking questions in the history of mankind is what kind of universe we are living in. We were always concerned about our place in the universe and in early history we thought that we were the center of the universe. A major revolution in the view of the universe was made around the middle of the 16th century, by Polish astronomer Nicholaus Copernicus. Before Copernicus, it was believed that we had a special place in the universe. According to the Earth-centered universe of Aristotle and Ptolemy the Sun, the planets, and the stars, are attached to rigid, crystalline spheres, which revolve in perfect circles around the Earth. In his book, *'De Revolutionibus Orbium Coelestium'*, Copernicus showed that the Sun is the center of the solar system. In the Copernican system, the stars are not attached to the rigid celestial sphere and can be at different distances to the Earth. This was the first step to a cosmological universe. Shakespeare wrote Hamlet at the end of the 16th century but it was not until the 20th century that we gained a better understanding of the universe.
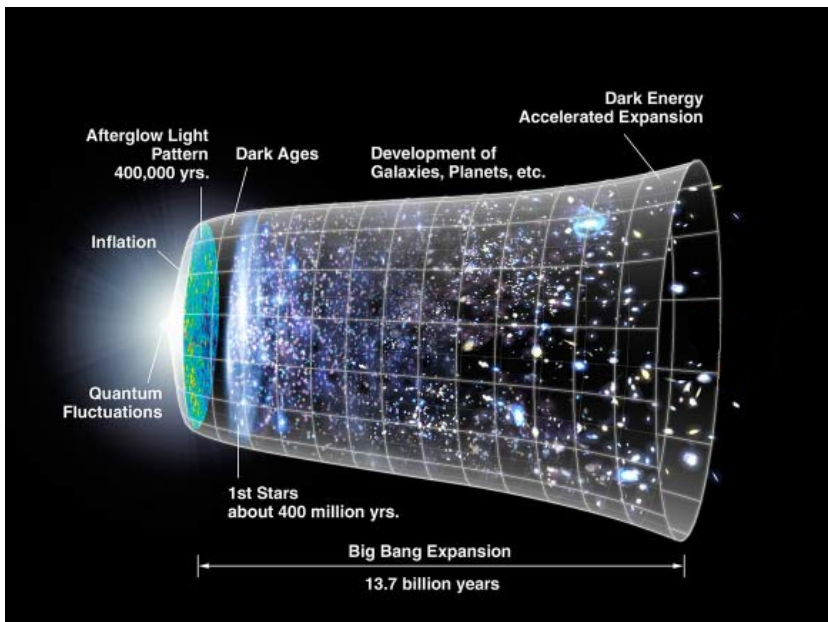

Figure 1.1 – Schematic view of the expansion of the universe. Image credit: NASA/WMAP Science Team.

In the early 20th century, Einstein developed the theory of General Relativity. In the 1920s, both Lemaître and Friedmann solved, independently, Einstein's field equations of relativity and realized that the universe could not be static; it must be either expanding or contracting. In 1929, Edwin Hubble experimentally demonstrated, by observing the recession of distant galaxies, that the universe is expanding. However, it was Lemaître who came up with the idea that if matter is receding everywhere, then it is logical to think that in a distant past the universe was in an extremely compact and compressed state, the so-called hot big bang model. The hot big bang model indicates that space has come to existence in a finite past from an extremely small volume and that the properties of the universe (density, temperature, volume), change with time. One can estimate the age of the universe, by determining how fast the universe is expanding, as 13.7 billion years (see Figure 1.1 for a schematic view of the expansion of the universe). Furthermore, observations of the expansion of the universe, the Cosmic Microwave Radiation (CMB), and the nucleosynthesis of the light elements match very well with the predictions from the hot big bang model which is now accepted as an accurate description of the universe.

1.1.1 Friedmann-Lemaître-Robertson-Walker Universe

The pillars of the hot big bang theory are the theory of General Relativity and the Cosmological Principle. Einstein's theory of general relativity is a mathematical formulation of space-time which describes the gravitational evolution of the universe in terms of space-time curvature. The Cosmological Principle states that on average the universe is homogeneous and isotropic, meaning that there is no preferred location and direction in the universe. The metric that describes a homogeneous, isotropic universe is called the Friedmann-Lemaître-Robertson-Walker (FLRW) metric and is given by:

$$ds^2 = dt^2 - a^2(t)\left[\frac{dr^2}{1 - kr^2} + r^2 d\Omega^2\right], \tag{1.1}$$

where t is the cosmic time, $a(t)$ is the scale factor that describes the dynamics of the universe (expanding or contracting), r is the comoving radial distance, k is the curvature of space which can be either 1 (spherical), 0 (flat) or -1 (hyperbolic) and $d\Omega^2 = d\theta^2 + \sin^2\theta d\phi^2$. The comoving coordinates of a point in space (r, θ, ϕ) stay constant if the expansion of the universe is perfectly homogenous and isotropic. Einstein's field equations are given by:

$$G_{\mu\nu} + g_{\mu\nu}\Lambda = \frac{8\pi G}{c^4} T_{\mu\nu}, \tag{1.2}$$

where $G_{\mu\nu}$ is the Einstein tensor, $g_{\mu\nu}$ is the metric tensor, $T^{\mu\nu}$ is the stress-energy tensor which describes mass, energy and momentum of matter and radiation, G

is Newton's gravitational constant, Λ is the cosmological constant. Here the -+++ sign convention is used. The Einstein field equations couple curved space-time to the dynamics of its matter-energy content. Solving Einstein's field equations for a space that is described by the FLRW metric leads to the Friedmann equations, which can be written for a universe with a cosmological constant Λ as

$$\left(\frac{\dot{a}}{a}\right)^2 = \frac{8\pi G}{3}\rho - \frac{kc^2}{a^2} + \frac{\Lambda c^2}{3}, \tag{1.3}$$

$$\frac{\ddot{a}}{a} = -\frac{4\pi G}{3}\left(\rho + \frac{3P}{c^2}\right) + \frac{\Lambda c^2}{3}, \tag{1.4}$$

where the dimensionless expansion factor $a(t) = \frac{R(t)}{R_o}$, c is the speed of light in vacuum, ρ and p are the mass-energy density and pressure of the universe, respectively. In the literature the first equation is called the Friedmann equation while the second equation is called the Friedmann acceleration equation. The term on left hand side of the first equation is the square of the Hubble parameter, H. For a flat universe, $k = 0$, one can derive the critical density as

$$\rho_{crit} = \frac{3H^2}{8\pi G}. \tag{1.5}$$

We can relate the cosmic density ρ to the critical density in dimensionless form as $\Omega = \frac{\rho}{\rho_{crit}} = \frac{8\pi G\rho}{3H^2}$. Then one can rewrite the Friedmann equation in the form of

$$kc^2 = a^2 H^2 (\Omega - 1). \tag{1.6}$$

This suggests that the curvature of the universe depends on the density. For $k > 0$, $\Omega > 1$ the universe is spherical (positively curved) and closed (Big Crunch), for $k < 0$, $\Omega < 1$ the universe is hyperbolic (negatively curved) and open. In the case of $k = 0$, one has a geometrically flat universe where its expansion will halt at a $\rightarrow \infty$.

For a universe consisting of radiation, matter, and vacuum energy, one can rewrite the Friedmann equation for the current time as

$$\frac{H^2}{H_o^2} = \Omega_r a^{-4} + \Omega_m a^{-3} + \Omega_k a^{-2} + \Omega_v. \tag{1.7}$$

Here H_o is defined as the value of the Hubble parameter today, Ω_r is the radiation density, Ω_m is the matter (dark + baryonic) density, $\Omega_k = 1 - \Omega$ is the "spatial curvature density" and Ω_v is the vacuum density today ($a = 1$). Each term on the right hand side dominates the universe at different times (first radiation then matter and later vacuum energy), where the universe expands as $a(t) \sim t^{1/2}$ during the radiation dominated era, $a(t) \sim t^{2/3}$ during the matter dominated era.

The observed values of matter, curvature and dark energy contents of the universe, according to the Wilkinson Microwave Anisotropy Probe 7 (WMAP 7), are

0.266 ± 0.029, 10^{-4} and 0.734 ± 0.029, respectively. This implies that a very large part of the universe's content today is in the form of dark energy. Recent observations of type Ia supernovae have shown that the rate of the cosmic expansion of the universe is accelerating (Amanullah et al. 2010, Perlmutter et al. 1999, 1998, Garnavich et al. 1998, Schmidt et al. 1998, Riess et al. 1998). This late-time phenomenon is often referred to as dark energy (DE). The nature of DE is a major challenge in cosmology and is the central interest of active research. Each component of the universe can be described by its equation of state parameter w defined by $w = \frac{P}{\rho}$. For matter $w = 0$, for radiation $w = 1/3$, and for dark energy (as a cosmological constant) $w = -1$. One can rewrite the acceleration equation of Friedmann as

$$\frac{1}{\rho}\frac{d\rho}{dt} = -3H\left(1 + \frac{P}{\rho}\right) \equiv -3H[1 + w(z)], \tag{1.8}$$

where the Hubble parameter is defined as $H^2 = \frac{8\pi}{3}\rho$. Hence, dark energy with sufficient negative pressure can drive the accelerated expansion of the universe. The equation of state parameter of dark energy is an important feature in understanding the behavior of DE. There are three popular values of w for dark energy: $w < 1/3$ (quintessence), $w = -1$ (cosmological constant), $w < -1$ (phantom energy). For time-dependent dark energy one can solve the above equation with $w = w(a)$:

$$\frac{d\rho}{dt} = -3[\rho + w(a)\rho]\frac{\dot{a}}{a} \tag{1.9}$$

$$\Rightarrow \rho \propto \exp\left\{-3\int^{a}[1 + w(a')]\frac{da'}{a'}\right\}, \tag{1.10}$$

and for constant dark energy

$$\rho \propto \exp\left\{-3(1 + w)\int^{a}\frac{da'}{a'}\right\} = \exp\{-3(1 + w)\ln a\} = a^{-3(1+w)}. \tag{1.11}$$

In the literature there are many theories on the nature of DE (Spaans 1997, Jacobson & Mattingly 2001, Zlosnik et al. 2007, Hořava 2009, Jacobson 2010, Sanders 2011). At the moment, with the present observational data, it is not possible to distinguish between different DE theories. In the near future with new observational techniques (Watson et al. 2011, Wang 2012) we expect to have higher precision and redshift ($z > 1$) measurements of dark energy that will enlighten us.

1.1.2   Structure Formation in ΛCDM

On small scales ($< 100\ h^{-1}$ Mpc) the universe is inhomogeneous and anisotropic, and we see a lot of structures like, stars, galaxies, galaxy clusters. The theory that explains the formation of these structures in the universe is called the 'Gravitational Instability Theory'. According to the gravitational instability theory the universe had an accelerated superluminal expansion in its early epoch, the so-called inflationary phase, where primordial density fluctuations were generated

out of quantum fluctuations of the vacuum (see Figure 1.2). The structures that we observe today are the result of the gravitational growth of those fluctuations. The observed fluctuations in the temperature of the CMB, $\frac{\Delta T}{T} < 10^{-5}$ (T = 2.725 K), support the idea of these small density perturbations.
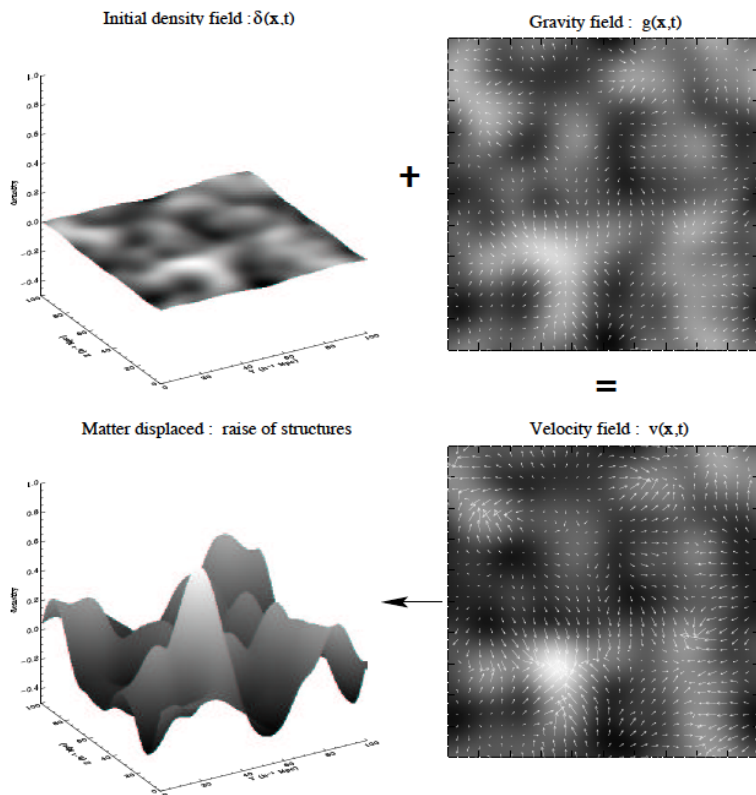
Figure 1.2 – Gravitational instability theory. The initial small density perturbations grow under the influence of gravity. Image credit: Emilio Romano-Diaz.

1.1.3   Linear Gravitational Growth

In order to derive an inhomogeneous and isotropic universe one can add small density perturbations onto a homogeneous and isotropic universe to resemble the observed fluctuations in the CMB. We can express the relative density perturbation

$$\delta(x) = \frac{\rho(r)}{\bar{\rho}}, \tag{1.12}$$

where x corresponds to co-moving spatial coordinates ($x = \frac{r}{a}$), and $\bar{\rho}$ is the mean fluid density with a corresponding peculiar velocity u ≡ v - Hr. For $\delta \ll 1$, we can solve the equations below analytically by using linear perturbation theory. For $\delta \sim 1$, we need to make a specific assumption (i.e., spherical symmetry), and for $\delta \gg 1$ the equations become highly non-linear and can only be solved numerically or with the use of higher order perturbation theory.

In the $\delta \ll 1$ regime, to follow the fluid motion one has to solve the equations of hydrodynamics which are given in co-moving coordinates as

$$\frac{\partial \delta}{\partial t} + \frac{1}{a}\nabla[(1 + \delta)u] = 0 \quad \text{Continuity equation,} \tag{1.13}$$

$$\frac{\partial u}{\partial t} + Hu + \frac{1}{a}(u.\nabla)u = -\frac{1}{a}\nabla\phi \quad \text{Euler equation,} \tag{1.14}$$

$$\nabla\phi = 4\pi G\bar{\rho}a^2\delta \quad \text{Poisson equation,} \tag{1.15}$$

where ρ is the local co-moving mass density of gas and particles (collisionless fluid), and $\bar{\rho}$ is its global average value, u is the fluid velocity vector. By introducing small perturbations and linearizing these hydrodynamical equations we get

$$\frac{\partial \delta}{\partial t} + \frac{1}{a}\nabla u = 0, \tag{1.16}$$

$$\frac{\partial u}{\partial t} + Hu + \frac{1}{a}\nabla\phi = 0, \tag{1.17}$$

$$\nabla\phi = 4\pi G\bar{\rho}a^2\delta. \tag{1.18}$$

For cold dark matter, where pressure is negligible, we obtain, by combining the equations above, a single equation for the density perturbation (Peebles 1980):

$$\frac{\partial^2 \delta}{\partial t^2} + 2H\frac{\partial \delta}{\partial t} = 4\pi G\bar{\rho}\delta. \tag{1.19}$$

This linear equation has in general two independent solutions, a growing solution usually denoted by $D_1(t)$, and a decaying solution $D_2(t)$. The general solution is

$$\delta(x, t) = A(x, t)D_1(t) + B(x, t)D_2(t), \tag{1.20}$$

with A and B arbitrary. The decaying part can be ignored when δ (x,t) is generated by vacuum fluctuations. Therefore, the density perturbation maintains its shape in comoving coordinates and grows in proportion to a growth factor $D(t)$, until it becomes non-linear. For a spatially flat, matter dominated universe, where H = $\frac{2}{3t}$, the general solution for the time evolution of density perturbations is δ (x, t) ≈ $D_1 t^{2/3} + D_2 t^{-1}$. The decaying mode becomes negligible with time and the growth rate of density perturbation becomes $\delta(x, t) \propto t^{2/3} \propto \frac{1}{1+z}$.

The above equation shows that the small density fluctuations grow with time under the influence of gravity. But the spatial dependence of the growth is not

constrained. In order to derive the spatial dependence we need to know the initial conditions at early times, which are predicted by the inflation model. According to the inflation model cosmological perturbations are (in the linear regime) Gaussian. The spatial form of the initial density fluctuations can be described in Fourier space, in terms of Fourier components

$$\delta(k) = \int d^3 x \delta(x) e^{-ikx}, \tag{1.21}$$

where $k = \frac{2\pi}{\lambda}$. In addition to Gaussianity, the distribution is assumed to be statistically homogeneous and isotropic in space. This means that the probability distribution is independent of the direction of the Fourier k modes and the variance is described in terms of the power spectrum P(k) as follows:

$$\langle \delta_k \delta_k^{*\prime} \rangle = (2\pi)^3 P(k) \delta^{(3)}(k - k'), \tag{1.22}$$

where $\delta^{(3)}$ is the three-dimensional Dirac delta function. In standard models, the expected power spectrum has a scale-invariant power-law form $P(k) \propto k^n$. The favored value for the power law index n is 1 and the spectrum following from n = 1 is referred as the Harrison-Zeldovich spectrum.

During the evolution of the early universe, until the end of the epoch of recombination, by various processes like growth under self-gravity, dissipative processes and pressure effects, the primordial power spectrum is changed. This can be expressed with the following equation

$$P(k) = P_o(k)T(k)^2 = Ak^n T(k)^2. \tag{1.23}$$

Here P_o is the initial value and A is a normalization parameter which needs to be fixed by observations. The overall effect is captured by the transfer function $T(k)$, which gives the ratio of the later time amplitude of a mode to its initial value

$$T(k) = \frac{ln(1 + 2.34q)}{2.34q}[1 + 3.89q + (16.1q)^2 + (5.96)^3 + (6.71)^4]^{-1/4}, \tag{1.24}$$

with $q \equiv \frac{k/hMpc^{-1}}{\Gamma}$, where Γ is the shape parameter. The general form of the shape parameter is given by Sugiyama (1995) as

$$\Gamma = \Omega_m h \exp\left[-\Omega_b\left(1 + \frac{\sqrt{2h}}{\Omega_m}\right)\right], \tag{1.25}$$

where Ω_b is the baryon fraction density parameter. Figure 1.7 shows the observed power spectrum of the CMB and the best fit to the WMAP data from the ΛCDM model.
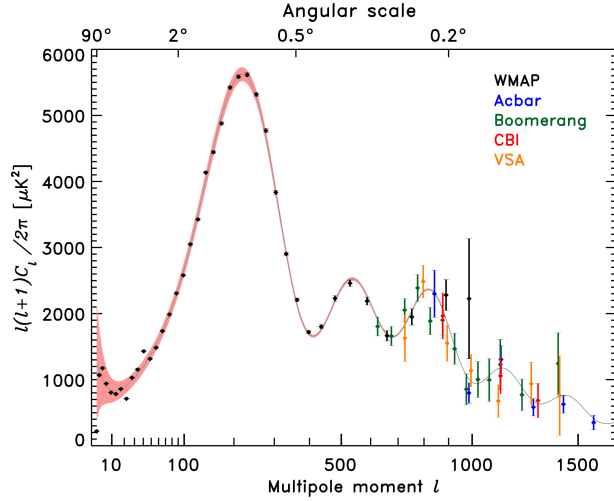
Figure 1.3 – The power spectrum of the CMB temperature anisotropy. The data shown come from the WMAP (2006), Acbar (2004), Boomerang (2005), CBI (2004), and VSA (2004) instruments. The solid line is a theoretical model. Image credit: NASA/WMAP Science Team.

1.1.4   Non-linear Growth

Once an overdense region has a $\delta > 1$, the evolution of the density growth can no longer be solved by linear perturbation theory. Instead, one needs to seek numerical solutions. In such overdense regions, the self-gravity of local matter will causes it to decouple from the Hubble flow and form bound objects, so-called dark matter halo.

In the last two decades, cosmological simulations have become an important tool for theoreticians to compute the formation of structure in the universe from primordial fluctuations. The cosmological model that currently matches the observations best is the so-called Cold Dark Matter (CDM) model. According to the ΛCDM model the Universe consists of 73% dark energy, 23% dark matter, and 4% baryonic matter. Primordial density perturbations on small scales appear to have a much higher amplitude than those on large scales. This leads to the conclusion that small clumps are the first to collapse and form structures and then these build up larger structures by mergers and the accretion of matter. This process is called hierarchical structure formation.

A powerful model of hierarchical structure formation is the Press-Schechter formalism (Press & Schechter 1974). It describes a universe where different scales collapse in a similar manner without any dependence on scale. The Press-Schechter formalism is used to estimate the number of collapsed objects (halos) as a function of mass at any given time. In this formalism, it is assumed that the dense objects

that we observe today result from the peaks in the initial density field. This formalism states that the number of halos per co-moving volume with masses in the range (M, M+dM) is

$$n(M, z)dM = \sqrt{\frac{2}{\pi}} \frac{\rho_o}{M} \frac{dv}{dM} \exp\left(-\frac{v^2}{2}\right)dM, \qquad (1.26)$$

where z is the redshift and ρ_o is the background density. In this equation, v is defined as:

$$v = \frac{\delta c}{D(z)} \sigma(M), \qquad (1.27)$$

where δc is the critical overdensity, D(z) is the linear growth factor and $\sigma(M)$ is the root variance of the primordial density field in spheres containing mass M on average, which is extrapolated to z = 0 by using linear theory. In the Press-Schechter formalism it is assumed that density peaks are perfectly spherically symmetric, although in reality this is not the case. Sheth & Tormen (1999) generalized the Press-Schechter formalism to incorporate homogeneous ellipsoidal density perturbations. In this case equation (1.22) becomes

$$n(M, z)dM = A\left(1 + \frac{1}{v'^{2q}}\right)\sqrt{\frac{2}{\pi}} \frac{\rho_o}{M} \frac{dv}{dM} \exp\left(-\frac{v'^2}{2}\right)dM, \qquad (1.28)$$

where $v' = \sqrt{av}$. The improved formalism of Sheth & Tormen (1999), reproduces the main results of Press-Schechter while correcting the discrepancies at the high and low mass extremes of the halo mass function.

1.2 The First Stars and Their Feedback Effects

1.2.1 Big Bang Nucleosynthesis

In order to understand the formation of the first stars one needs to know the conditions (temperature, density, chemical composition) under which the first stars are formed. In this, big bang nucleosynthesis (BBN) provides the deepest reliable probe of the early universe based on the standard model of particle physics.

To be able to predict the primordial abundances of the light elements (D, ^{3}He, ^{4}He, ^{7}Li), synthesized in the big bang, we need to know the current temperature and expansion rate of the universe. Then, by assuming that the universe is homogenous and isotropic, we can estimate the particle content of the universe depending only on the baryon density.

At the time nucleosynthesis begins, approximately one second after the big bang, the temperature is about 10^{10} K. At higher temperatures, due to weak interactions, neutrons and protons can interconvert and thus fix the neutron-to-proton ratio (n/p) to its thermal equilibrium value, $n/p = e^{-Q/T}$, where $Q = 1.293$ MeV is the neutron-proton mass difference. As the temperature drops due to the expansion, the neutron-to-proton interconversion rate decreases exponentially with

temperature. Once the interconversion rate becomes less than the expansion rate, the neutron-to-proton ratio 'freezes-out' at $n/p \sim 1/6$. After freeze-out the neutrons are free to β-decay, hence the neutron-to-proton ratio drops to $\simeq 1/7$.

The nucleosynthesis chain begins with the formation of deuterium in the process, $p + n \rightarrow D + \gamma$. But even though freeze-out occurs at a temperature below the deuterium binding energy, $E_B = 2.2$ MeV, due to the photo-dissociation by the high number density of photons, the reaction does not proceed until the temperature of the universe falls to 10^9 K or kT = 0.1 MeV, about 100 seconds after the big bang. Once deuterium formed, further reactions proceed to form the most stable light element, ^{4}He. Also, ^{3}He and a small amount (10^{-10}) of ^{7}Li is produced. Heavier nuclei do not form because of the absence of stable elements of atomic number 5 or 8. Hence, the constituents of the primordial gas, estimated from BBN, are D, ^{3}He, ^{4}He, and ^{7}Li. In Figure 1.4, the abundances of the light elements synthesized by the big bang are shown.

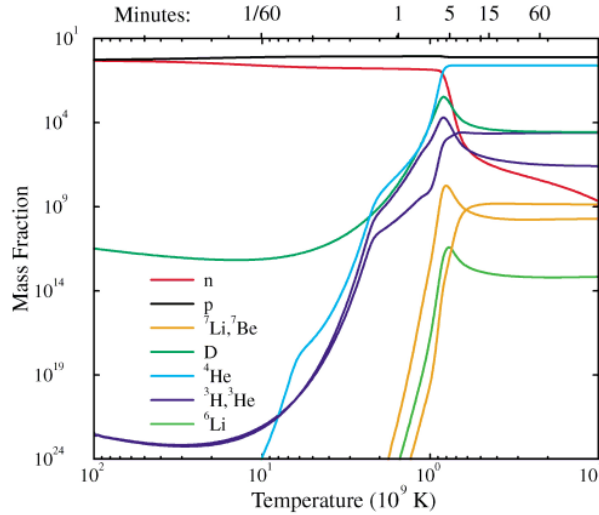**Figure 1.4** – The time evolution of the abundances of the light elements synthesized during BBN. Image credit: Burles et al. (1999).

1.2.2 Formation of the First Stars

From BBN we conclude that the primordial gas, from which the first stars are made, was metal free and there were no dust grains to couple the gas to radiation emitted by the protostar or winds from other stars. Furthermore, it is assumed

that even though magnetic fields could have been generated in the accretion disk around a primordial protostar (Tan & Blackman 2004), they could not affect the star formation process since they only become dynamically important when the latter is well underway. Therefore, theoretically the physics of the first stars are rather simple compared to the physics of present-day star formation (Abel et al. 2002, Bromm et al. 2002).

For the star formation process the important aspect is that gas in a dark halo becomes gravitationally unstable and collapses. According to the Press-Schechter formalism typical halos undergoing this process are the least massive ones. However, the Press-Schechter formalism tells us when the first dark matter halos of a given mass form, but it does not contain any information about the behavior of the baryonic matter. In order for gas to collapse, into pre-existing dark matter halos, gravity should overcome the internal pressure. One can estimate the scale on which pressure forces become significant by equating the sound-crossing timescale, with the gravitational free-fall timescale (t_{ff}). This sets a critical scale, called the Jeans length (λ_J, Jeans (1928)) at which the pressure and gravitational forces cancel out each other. It is given by,

$$\lambda_J = \frac{\sqrt{\pi}c_s}{\sqrt{G\rho}}, \tag{1.29}$$

where c_s is the sound speed. On scales smaller than λ_J, the sound-crossing timescale is shorter than the gravitational free-fall timescale, meaning that there is enough pressure support against gravity and therefore the gas does not collapse. On the other hand, on larger scales gravity wins over the pressure and gravitational collapse becomes inevitable. The Jeans mass M_J, which corresponds to the mass within a sphere of radius $\lambda_J/2$, is given by

$$M_J = \frac{4\pi}{3}\bar{\rho}\left(\frac{\lambda_J}{2}\right)^3. \tag{1.30}$$

The residual fraction of free electrons couple the gas temperature T_{gas} to the cosmic microwave background temperature T_{CMB} until a redshift of $1 + z_t \approx 1000(\Omega_h^2)^{2/5}$ (Peebles 1993). At redshift $z > z_t$ the Jeans mass is time-independent, whereas at $z < z_t$ the gas temperature declines adiabatically as $[(1+z)/(1+z_t)]^2$ and M_J decreases with decreasing redshift as

$$M_J = 3.08 \times 10^3 \left(\frac{\Omega_m h^2}{0.13}\right)^{-1/2} \left(\frac{\Omega_b h^2}{0.022}\right)^{-3/5} \left(\frac{1+z}{10}\right)^{3/2} M_\odot. \tag{1.31}$$

One thing to keep in mind is that because it is a perturbative analysis, the Jeans mass describes only the initial phase of the collapse. Therefore, it is a necessary criterion to start the collapse but not a sufficient one.

According to cosmological simulations following the ΛCDM model of hierarchical structure formation, the first stars formed at $z \sim 30$ in dark matter halos with masses of 10^5-10^6 $M_\odot$, corresponding to virial temperatures of $T_{vir} \leq 10^4$ K

(Tegmark et al. 1997, Abel et al. 2002, Bromm et al. 2002, Yoshida et al. 2003, O'Shea & Norman 2007). Once the gas has virialized in potential wells of pre-existing dark matter halos, additional cooling is required in order for the gas to collapse further and to form stars

The cooling of primordial gas depends, in the absence of metals, only on atomic and molecular hydrogen. At temperatures $T \geq 10^4$ K the important coolant is atomic hydrogen. Following the recombination of hydrogen, molecular hydrogen can form, which is the dominant coolant at temperatures between $100 < T < 10^4$ K. In order for a gas cloud to cool efficiently the cooling time (t_{cool}) should be less than t_{ff} where $t_{cool} = \frac{3nkT}{2\Lambda(n,t)}$ and $t_{ff} = (\frac{3\pi}{32G\rho})^{1/2}$. When $t_{cool} \ll t_{ff}$ the pressure cannot balance the gravitational contraction, because of radiative losses, and the cloud collapses. Here the challenge is what happens to this gas when it collapses. Does it fragment and form binary systems or even clusters of stars, or does it form a single massive star? It is suggested that such subfragmentation could occur due to the enhancement of the abundance of molecular hydrogen via three-body reactions (Palla et al. 1983), at densities above $\sim 10^8$ cm^{-3}. This can give a boost in cooling thus triggering a thermal instability which in turn can cause further fragmentation (Silk 1983). However, in their work both Abel et al. (2002) and Bromm et al. (2002) have found no further fragmentation even though they have included the three-body reactions in their chemical reaction networks. The reason for this is that the increase in the cooling is balanced by the compressional heating and therefore there is no significant drop in temperature. Hence, the Jeans mass of the cloud does not decrease, which is the necessary criterion to stop fragmentation.

The Jeans mass of the cloud scales as

$$M_J \propto \rho^{3/2(\gamma_{eff}-4/3)}, \tag{1.32}$$

where $\gamma_{eff} = 1 + \frac{dlnT}{dln\rho}$ is the effective adiabatic exponent (Spaans & Silk 2000). If $\gamma_{eff} > 4/3$, then the Jeans mass will increase during the collapse and at some point it will become comparable to the mass of the protogalaxy and the collapse will halt. For a monoatomic gas evolving adiabatically, $\gamma_{eff} = 5/3$, the collapse will be halted before protostellar densities are reached due to the increasing pressure support against gravitational collapse. Therefore, star formation is only possible if the gas can cool.

Nowadays, in the literature, the first stars are called Pop III stars. These stars might have formed in various environments and this might have caused different modes of Pop III star formation. Indeed, it has become evident that Pop III star formation might have two distinct modes: Pop III.1 and Pop III.2 stars (McKee & Tan 2008). Pop III.1 stars are the first generation of stars that are formed from the collapse of the primordial gas into DM minihalos, whereas Pop III.2 stars are the second generation of these stars that are affected by the radiation of previously formed stars. Pop III.2 stars will be less massive than Pop III.1 stars because when the gas is ionized by the previous generation of stars, HD cooling becomes important which allows the gas to cool more efficiently and therefore lowers the mass

of these stars through the Jeans mass criterion as explained above.

The chemical composition and the metallicity of the interstellar gas are the key parameters to study when investigating the formation of the first stars. Although the primordial gas is complex, we can simplify the chemistry according to the contributions of the various elements to the cooling process (see Table 1.1).

Name	Metallicity (Z)	Mass ($M_\odot$)	Formation
Pop III.1	0	$\lesssim 100$	H_2 cooling
Pop III.2	0	10-100	HD and H_2 cooling
Pop II.5	$\lesssim Z_{crit}$	$\lesssim 10$	metal line cooling
Pop II	$> Z_{crit}$	local IMF	metal enriched star formation

Table 1.1 – Typical metallicity, mass values and dominant cooling mechanisms of the first stars.

The main coolants for primordial gas with temperatures $T \geq 10^4$K are Lyman α emission of neutral atomic hydrogen (H I, 1216 Å), and helium (He II, 304 Å). Below this temperature, which is the case in the minihalos with temperatures $T_{vir} \lesssim 10^4 K$, the cooling process is dominated by molecular hydrogen (H_2), where one can calculate T_{vir} as follows

$$T_{vir} = 1.98 \times 10^4 \left(\frac{\mu}{0.6}\right)\left(\frac{M}{10^8 h^{-1} M_\odot}\right)^{2/3}\left(\frac{\Omega}{\Omega_z}\frac{\Delta}{18\pi^2}\right)^{1/3}\left(\frac{1+z}{10}\right)K \tag{1.33}$$

where μ is the mean molecular weight and Δ is the collapse overdensity.

The importance of H_2 cooling in primordial gas was first realized by Saslaw & Zipoy (1967) and Peebles & Dicke (1968). In present-day molecular clouds, H_2 formation occurs primarily on the surface of interstellar dust grains (Gould & Salpeter 1963, Cazaux & Tielens 2002, Cazaux & Spaans 2004). However, in the absence of dust H_2 forms via gas phase reactions. The reaction

$$H + H \rightarrow H_2 + h\nu \tag{1.34}$$

is not common because it is necessary to have an excited electronic state of hydrogen. This happens near the end of the re-ionization epoch (Latter & Black 1991, Rawlings et al. 1993).

$$H + H + H \rightarrow H_2 + H \tag{1.35}$$

and

$$H + H + H_2 \rightarrow H_2 + H_2 \tag{1.36}$$

are called three-body formation. In these reactions the rate coefficients are small and therefore this pathway only becomes important at high densities ($n \gtrsim 10^8$ cm^{-3}, Palla et al. (1983)). On the other hand, the dominant reactions that lead to the formation of H_2 at low densities are as follows

$$H + e^- \rightarrow H^- + h\nu, \tag{1.37}$$

$$H^- + H \rightarrow H_2 + e^-, \tag{1.38}$$

and

$$H^+ + H \rightarrow H_2^+ + h\nu, \tag{1.39}$$

$$H_2^+ + H \rightarrow H_2 + H^+. \tag{1.40}$$

For these two paths of H_2 formation at low densities, the formation rate is directly proportional to the fractional ionization of the gas. The H^- in the first reaction forms much faster than H^+ in the second reaction. Therefore, the first reaction is more efficient in forming H_2 at low densities.

One can calculate the H_2 cooling rate for given H_2 abundances, density and temperature of the gas. The first excited rotational state of H_2 lies at $\sim$ 500 K. Figure 1.5 shows that the cooling rate of H_2 falls off exponentially with decreasing temperatures, due to the large excitation energy of the first accessible excited state, and is essentially negligible below 100 K. It scales with density as $\Lambda_{H_2} \propto n^2$ at low densities, where radiative de-excitation dominates, and as $\Lambda_{H_2} \propto n$ at high densities, where collisional de-excitation dominates and the level populations approach their local thermodynamic equilibrium (LTE) values.
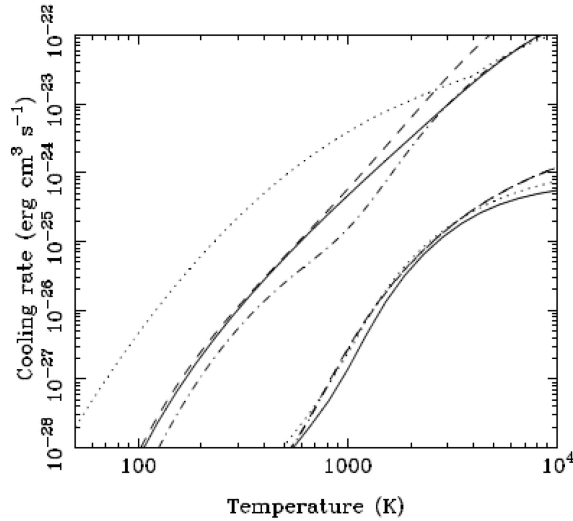
Figure 1.5 – A comparison of various parametrizations of the H_2 cooling function, plotted in units of erg cm^3 s^{-1}. Rates are computed assuming that $n \gg n_{H_2}$, and that the ortho-to-para ratio is 3:1. The lower set of lines corresponds to a gas density $n = 10^6$ cm^{-3}; the upper set corresponds to n = 100 cm^{-3}. Solid line Le Bourlot et al. (1999); dashed line Galli & Palla (1998); dotted line Lepp & Shull (1983); dash-dotted line Hollenbach & McKee (1979). Image credit: Stiavelli (2009).

Hydrogen deuteride, HD, is an important coolant below 200 K in the primordial gas. The first excited rotational state of HD lies at a temperature of $\sim$ 150 K. If there is enough HD, the gas can cool down to the temperature of the cosmic microwave background (CMB) (Nakamura & Umemura 2002, Nagakura & Omukai 2005, Vasiliev & Shchekinov 2006, Johnson & Bromm 2006, Yoshida et al. 2007). Although the primordial deuterium abundance is small relative to hydrogen ($\frac{n_D}{n_H} = 4 \times 10^{-5}$), chemical fractionation leads to an enhancement of the ratio, $\frac{n_{HD}}{n_{H_2}} \approx 10^{-3}$ (Puy et al. 1993, Galli & Palla 1998, Stancil et al. 1998).

Molecular hydrogen does not have a permanent electric dipole moment while the HD molecule has and that makes HD a better coolant than H_2. The dominant reactions that lead to HD formation are

$$H_2 + D^+ \rightarrow HD + H^+ \tag{1.41}$$

and

$$D + H_2 \rightarrow HD + H. \tag{1.42}$$

Here the first reaction is endothermic (absorbs energy) by 462 K. At low temperatures the HD cooling rate per molecule is greater than that of H_2 (Glover & Abel 2008). The efficiency of HD cooling depends on whether the gas is ionized or not. In Pop III star formation calculations, the fractional ionization is small and the temperature of the gas is not low enough for chemical fractionation to become efficient. Therefore, we can neglect the effect of HD cooling. On the other hand, in an initially ionized gas HD will form in high abundances (Shapiro & Kang 1987). In their work, Nagakura & Omukai (2005), found that the gas would re-collapse upon ionization and form significant amounts of HD due to the presence of free electrons. Johnson & Bromm (2006) showed that when primordial gas is significantly ionized the cooling from HD is sufficient to lower the temperature to the level of the CMB and therefore this can give rise to Pop III.2 stars (see Figure 1.6).

When the primordial gas is enriched by metals as a result of Pop III SNe then one has to take into account the cooling from the fine-structure lines of metals. Many atoms have fine-structure lines. The relative motion of any orbiting electron and a charged nucleus creates a torque on the magnetic moment associated with the intrinsic spin of the electron. Because the electrons of H and He atoms are described by single-particle wavefunctions without any associated orbital angular momentum ($l = 0$), and the electric ground states of these atoms do not have internal torque there is no fine-structure splitting in these atoms. On the other hand, atoms like C, O, Si, Fe,... have fine-structure lines which enhance cooling in the metal enriched primordial gas. The final fate of the massive first stars, as predicted by theoretical work, is shown in Figure 1.7.

1.2.3 Feedback Effects

When the first stars form they will influence their surroundings. This is called a feedback effect. Feedback is a backreaction of a process onto itself or onto the
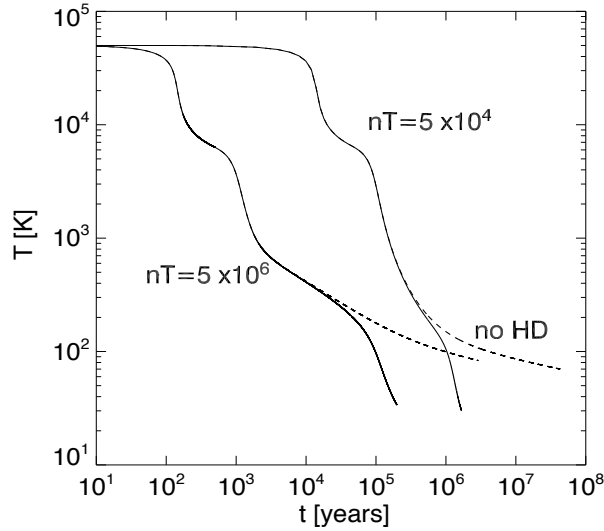
Figure 1.6 – Effect of HD cooling. Thermal evolution of an ionized gas with an initial temperature of 5×10^4 K under isobaric conditions with and without HD cooling (solid and dashed lines, respectively). Once a temperature of ≤ 300 K is reached, HD cooling dominates and the gas cools to essentially to CMB temperature, whereas gas with H$_2$ cooling does not cool below 60 K. Image credit: Yoshida et al. (2007).

causes that have produced it. It can be negative or positive. We can classify the feedback effects from the first stars into three groups: mechanical, chemical and radiative feedback.

1.2.3.1 Radiative Feedback

The radiation from the first stars will influence their surroundings by heating and ionizing/dissociating the gas. It is believed that the first stars are massive and emit copious amounts of UV (and some X-ray) radiation. Depending on the energy of the radiation, radiative feedback can be either negative or positive. If the radiation is soft UV (11.18-13.6 eV) photons can propagate great distances in the intergalactic medium (IGM) and build up a UV background which dissociates the fragile molecular hydrogen. In the absence of H$_2$ gas cannot cool efficiently and collapse, therefore the star formation becomes delayed or quenched (Haiman et al. 1997, 2000, Ciardi et al. 2000, Mackey et al. 2003, Yoshida et al. 2003, Wise & Abel 2008, Johnson et al. 2008).

Recent work by several authors, has shown that the H II ionization front expels gas when Pop III stars are formed in a minihalo of $10^6 M_\odot$ (Abel et al. 2007, Alvarez et al. 2006, Kitayama et al. 2004, Whalen et al. 2004). However, the net
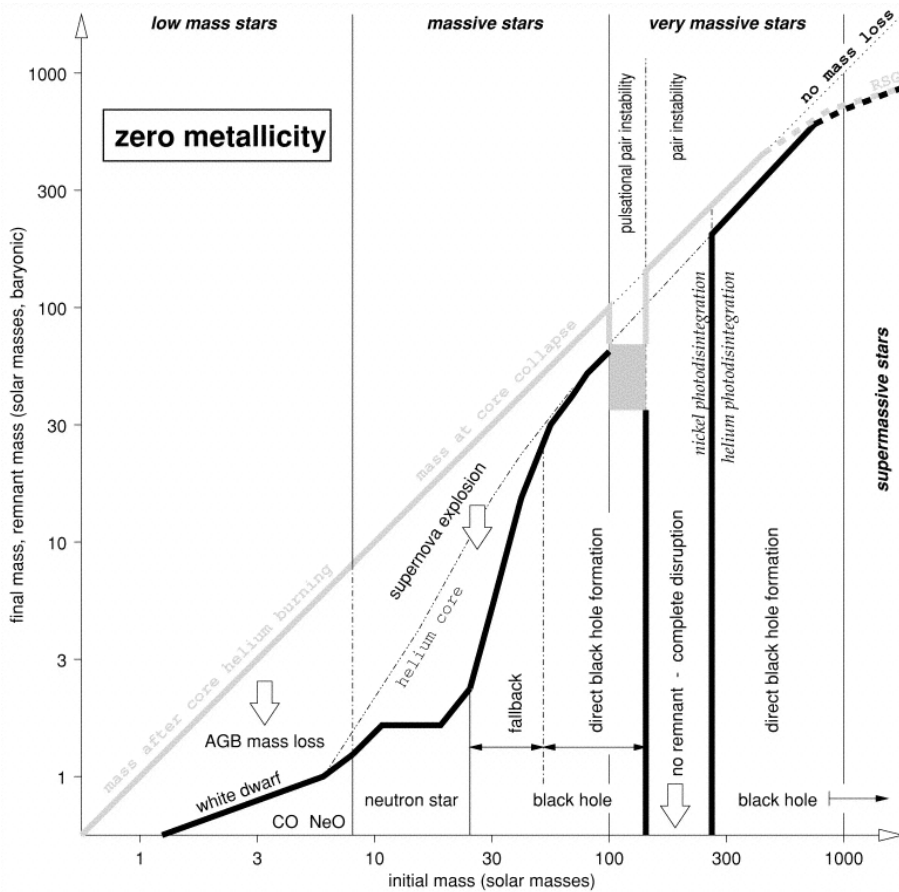
Figure 1.7 – Initial-final mass function of the non-rotating first stars by Heger & Woosley (2002). The x-axis is the initial stellar mass and the y-axis is the final mass of the collapsed remnant (thick black curve) and the mass of the star when the event begins that produces that remnant (thick gray curve). Since no mass loss is expected for metal-free stars before the final stage, the gray curve is approximately the same as the line of no mass loss (dotted-line). Exceptions are ~ 100-140 $M_\odot$ where the pulsational pair instability ejects the outer layers of the star before it collapses, and above ~ 500 $M_\odot$, where pulsational instabilities in red supergiants may lead to significant mass loss.

effect of an H II region on the star formation is not known. This is because, even though initially the gas in the H II region will be heated to T > 10^4 K and suppress the star formation (Oh & Haiman 2003) later on, due to the high electron fraction produced by the photoionization, it will enhance the formation of molecular hydrogen, and this can allow star formation in the regions where otherwise

stars would not form. Also, as mentioned in section 1.2.2, due to the formation of deuterium hydride (HD) in the relics of H II regions the gas can cool efficiently to temperatures even below T < 100 K and this leads to low mass Pop III star formation (Johnson & Bromm 2006, 2007, Nagakura & Omukai 2005, O'Shea et al. 2005, Yoshida et al. 2007).

Moreover, accretion onto black hole remnants of the massive first stars can produce X-ray photons. This has a positive feedback effect by enhancing the free electron abundance, which in turn gives rise to gas phase H_2 formation and hence leads to efficient cooling of the gas and the formation of stars (Kuhlen & Madau 2005).

1.2.3.2   Chemical Feedback

Chemical feedback is related to the critical metallicity of the gas which leads to a transition in the star formation history. SNe of the massive first stars are crucial for understanding the metal enrichment of the ISM/IGM and the fate of the structure of the universe and star formation. Metal enriched primordial gas enhances cooling and is therefore believed to govern the underlying physics of the transition from Pop III to Pop II stars. Due to enhanced cooling by metals and dust the Jeans mass of protostars is lowered significantly, thus resulting in less massive stars. Chemical feedback has recently been studied by several authors (Bromm et al. 2001, Schneider et al. 2002, Omukai et al. 2005, Clark et al. 2008, Smith & Sigurdsson 2007). These studies have shown that metal line cooling is important in a non-zero metallicity gas, compared to H_2 and HD, for metallicities on the order of 10^{-3} (Bromm & Loeb 2003b) or even $10^{-5} - 10^{-6}$ (Jappsen et al. 2007). In the paper of Bromm et al. (2001), the critical metallicity for the transition between Pop III and Pop II stars was found to be $10^{-3.5} Z_\odot$, but this threshold is the point where metal line cooling becomes more important than H_2 cooling. There is also an important contribution to the cooling by the collisional coupling of warm gas and cool dust grains, provided the gas density exceeds 10^4 cm^{-3}. In their work Schneider et al. (2002) find that when the metallicity is in the range of $10^{-6} < Z/Z_\odot < 10^{-4}$ the fragmentation occurs on sub-Solar mass scales, hence the transition from a top-heavy IMF to a Salpeter IMF.

On the other hand, the epoch of Pop II stars depends on the number of Pop III stars that explode as pair instability supernovae (PISN), the metal ejection efficiency, and mixing in the intergalactic medium (IGM), as well as on the initial mass function. Since this is a complicated process, the use of a single critical metallicity can be misleading. Therefore, the patchy distribution of metals that is formed by the first SNe should be taken into account by using different cooling prescriptions for different metallicities.

1.2.3.3 Mechanical Feedback

Mechanical feedback affects the subsequent star formation process in different ways. At the end of their lifes, massive first stars lead to SNe. These SNe might blow-away or blow-out the gas from the halo which is the necessary fuel to form stars (Mac Low & Ferrara 1999, Nishi & Susa 1999, Bromm et al. 2003, Springel & Hernquist 2003, Wada & Venkatesan 2003). The SNe have a dramatic effect, especially for smaller mass dark matter halos ($M < 5 \times 10^6$ $M_\odot$), due to their shallower potential wells, by blowing away the gas and hence quench the star formation. On the other hand, according to the work of Mori et al. (2002) and Bromm et al. (2003), more massive halos appear to contain their gas reservoir better against the energy input from the SNe. In their work, Mori et al. (2002) considered a 10^8 $M_\odot$ system at $z = 9$ which has experienced multiple SNe and find that, depending on the stellar distribution, less than 30 % of the available SN energy is converted into kinetic energy and causes the blow-away of the gas from the halo. Similarly, Bromm et al. (2003) ran simulations which include PISN explosions ($E \sim 10^{53}$ erg) and type II SNe ($E \sim 10^{51}$ erg). They have shown that, while the more energetic case of PISNe results in blowing away of the gas, the less energetic type II SNe allows the gas to remain in the halo.

On the other hand, shocks can compress gas and increase the density so that gas cools down more efficiently and give rise to additional star formation (Vishniac 1983, Mackey et al. 2003, Salvaterra et al. 2004). This way, mechanical feedback has a positive effect. Furthermore, these SNe do enrich their surroundings by metals which in turn has a significant effect on the cooling ability of the gas (chemical feedback) and thus the mass of the subsequent stars (Vader 1986, Mac Low & Ferrara 1999, Fujita et al. 2004).

1.3 Formation of the First Galaxies, Supermassive Black Holes and Active Galactic Nuclei

In the literature, the first galaxies are defined as the halos that can maintain self-regulated star formation in a multi-phase interstellar medium and retain gas photoheated by the first stars (Dijkstra et al. 2004b, Mac Low & Ferrara 1999, Madau et al. 2001, Oh & Haiman 2002, Scannapieco et al. 2002, Wada & Venkatesan 2003). The feedback effects from the first stars play a crucial role in shaping the first galaxies. Chemical feedback effects from SNe enrich the medium by metals, ionizing radiation heats the gas and mechanical feedback blows away or blows out the gas and, hence, defines the fate of the host halo (see Section 1.2.3). According to cosmological simulations of hierarchical structure formation, these halos are assembled at redshift $z > 10$ with masses of $M > 10^7$ $M_\odot$.

Observations of high redshift ($z>6$) quasars suggest that they are powered by supermassive black holes (SMBHs) with masses on the order of 10^9 $M_\odot$ (Fan et al.

2003, 2006a, Kurk et al. 2007). These SMBHs are thought to be formed (in less than
1 billion years) through the accretion of gas onto seed black holes of masses between 10^2 - 10^5 M$_\odot$. Although the origin of these seed black holes is still an open
question, there are two plausible scenarios for the formation of these seed black
holes: a) they are the remnants of the first stars (M$_{BH}$ ~ 10^2 M$_\odot$, Johnson & Bromm
(2007)) or b) they are formed by the direct collapse of isothermal gas in atomic
cooling halos (M$_{BH}$ ~ 10^5 M$_\odot$, Bromm & Loeb (2003a), Spaans & Silk (2006), Wise
et al. (2008)) at the centers of the first galaxies.

The radiation in these quasars and active galactic nuclei (AGN) is thought
to come from a gaseous accretion disk surrounding the SMBHs (Salpeter 1964).
Studies of galactic nuclei at different wavelengths have revealed the presence of
large masses within small radii that can currently only be explained by the existence of central black holes. AGNs are highly luminous nuclei, which can outshine
their host galaxies, and show emission lines that are broader than the absorption
lines in normal galaxies. These emission lines arise from a small nucleus, cover a
wide range of ionization, and radiate throughout the entire electromagnetic spectrum, from the radio to the X-ray regime. In general, an object is defined to be an
AGN if one or more of the following properties are observed: a compact nuclear
region, brighter than normal, non-thermal continuum emission, strong emission
lines, and variations in the emission lines on short time scales. AGNs are classified according to their observational properties and in the unified model of AGNs
there are two basic types, depending on their optical and radio luminosity, called
radio-quiet and radio-loud. In each type, there is a wide range of variety in the
observed properties due to the orientation of the system relative to the observer:
e.g., Seyferts, quasars, blazars, optically violent variables... (see Table 1.2).

Table 1.2 – AGN Unification Model

Radio	Orientation	
Properties	Face-On	Edge-On
Radio-Quiet	Seyfert 1	Seyfert 2
	QSO	FIR galaxy
Radio-Loud	BL Lac	FR I
	BLRG	NLRG
	Quasar /OVV	FR II

The underlying structure of all AGNs is intrinsically similar within the unification model. There is a SMBH at the center with a mass of ~ 10^6 - 10^{10} M$_\odot$, surrounded by an accretion disk where the UV-optical continuum emission primarily
arises. The relativistic jets emerge along the disk axis and emit Doppler-boosted
radiation via synchrotron and inverse Compton mechanisms. The jets and the accretion disk both are thought to contribute to the X-ray emission. The broad emission lines are produced in relatively dense (electron densities of n$_e$ $\approx$ 10^{11} cm^{-3})

gas clouds at a few thousand astronomical units (AU) from the black hole with a characteristic full width half maximum (FWHM) ~ 1500-10000 km s^{-1} and are prominent in the UV-optical spectra of AGNs. On parsec scales, this entire system is embedded in a dusty inhomogeneous torus that is opaque over most of the electromagnetic spectrum. The torus absorbs radiation from the central source and re-emits it in the infrared. Narrow emission lines are produced in low density clouds with FWHM < 300-800 km s^{-1} at the torus scale and beyond (see Figure 1.8).
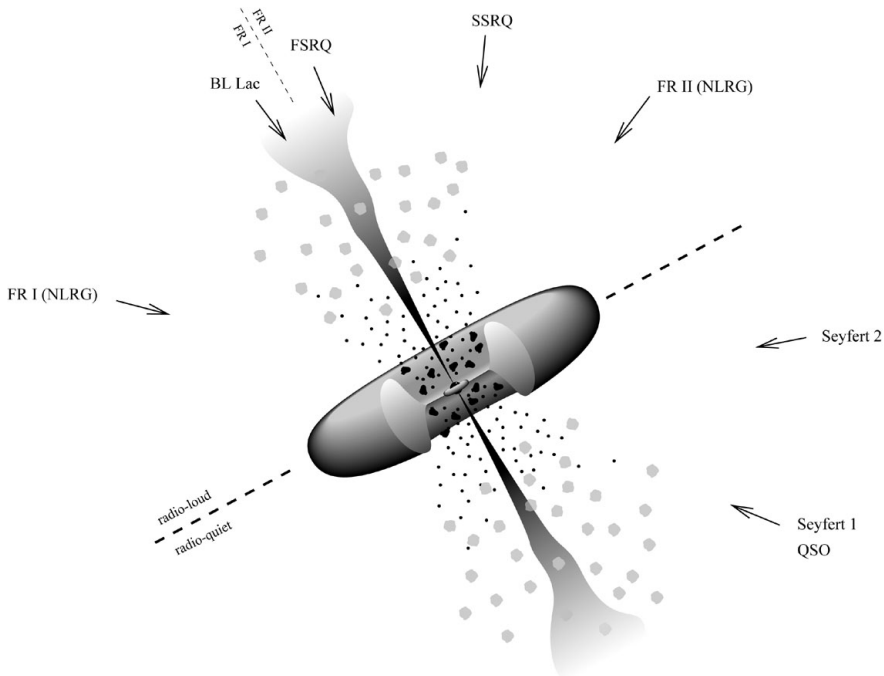

Figure 1.8 – The unification model for AGNs. With an orientation angle of 30°, where the narrow-line and broad-line regions are visible, Seyfert 1 galaxies are observed. At larger angular offsets, the broad-line region will be hidden by the torus, which corresponds to Seyfert 2 galaxies. Blazars have jets that are close to the line-of-sight. Perpendicular to the jet, the full extent of the jets may be seen particularly at low frequencies, giving rise to a morphology typical of radio galaxies. Image credit: Urry & Padovani (1995).

In the last decade, the growth of SMBHs in the centers of galaxies, and their role in shaping the evolution of galaxies and regulating the star formation history has become a central topic for cosmology. Dynamical studies of central black holes in nearby galaxies reveal that there is a relation between the central black hole mass and the bulge mass (M_{BH} / M_B ~ 10^{-3} Magorrian et al. (1998)) and veloc-

ity dispersion of the stellar component of the host galaxy ($M_{BH} \propto \sigma^4$, Ferrarese &
Merritt (2000), Gebhardt et al. (2000)). These relations support the idea that there
is a strong link between the formation and evolution of galaxies, and the growth of
SMBHs at their centers. However, the underlying physics of the observed relation
is still unknown. Several efforts have been made to explain the origin of this rela-
tion by using semi-analytical modeling (Kauffmann & Haehnelt 2000, Wyithe &
Loeb 2003) and N-body hydrodynamic simulations. Numerical simulations have
shown that the gravitational tidal torques excited during major mergers lead to
rapid inflows of gas into the centers of galaxies (Barnes & Hernquist 1991, 1996)
which can be the mechanism to trigger quasar activity and starbursts in galax-
ies. Also, it has been long known that intense star formation in galactic nuclei
preceeds quasar activity, which led to the theory that an evolutionary sequence,
caused by gas rich mergers, connects starbursts, quasars, SMBH growth, and the
formation of red elliptical galaxies (Hopkins et al. 2006, 2008, Tacconi et al. 2008,
Narayanan et al. 2009, 2010), as shown in Figure 1.9. The growth of SMBHs dur-
ing a quasar phase can be traced by the luminosity function of QSOs as a function
of redshift (Soltan 1982). The peak activity of luminous QSOs occurs at z ~ 2-3,
where the majority of the most massive galaxies were also forming most of their
stars. The average black hole mass in units of Solar mass increases with increas-
ing redshift, meaning that there are fewer low-mass black holes at high redshifts,
and the average accretion rate decreases towards lower redshift. This observed
anti-hierarchical behavior of AGN evolution indicates that SMBHs and their host
galaxies co-evolve. Walter et al. (2004) estimated the dynamical mass of high red-
shift quasars from the size and line width of the CO emission and found the SMBH
spheroidal bulge mass ratio to be an order of magnitude higher than what we ob-
serve in local galaxies. This indicates that there is an evolution in the M_{BH} - M_{bulge}
relation throughout cosmic time.

In their work, Hopkins et al. (2006) suggest that the accretion of gas, trig-
gered by mergers and/or interactions of galaxies, onto the black hole leads to
starbursts and quasar activity. Initially, due to the ubiquitous presence of dust
around the black hole, the quasar activity is obscured. Later on, when the black
hole dominates the energetics of the central region, the energy input from the
quasar quenches further star formation and expels the gas shrouding the quasar.
This slows down the further growth of the SMBH and stops the quasar activity,
which in turn leads to the formation of a normal spheroidal galaxy (see Figure
1.10). Observational support for this theory comes from the fact that in the local
universe, ultraluminous infrared galaxies (ULIRGs) have bolometric luminosities
similar to bright quasars and are often in mergers (Sanders et al. 1986, Sanders
& Mirabel 1996). Also, observations of low-redshift quasars show a connection
between galaxy mergers and quasar activity (Heckman et al. 1984, Bahcall et al.
1996). Moreover, there is observational evidence that ULIRGs form the birthplaces
of QSOs (Sanders et al. 1988, van der Werf et al. 2011).

In order to understand the origin of the Magorrian relation, AGNs are key to
study. The accretion of gas onto the central black hole yields a luminous source
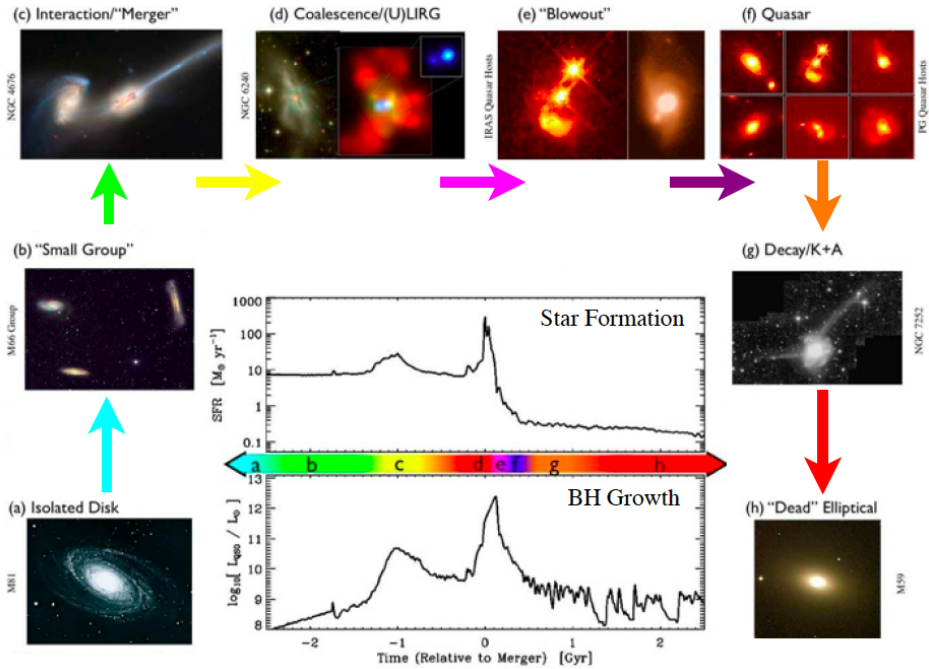
Figure 1.9 – Schematic outline of the evolutionary sequence of starbursts, AGN, quasars and red elliptical galaxies. Image credit: Hopkins et al. (2008).
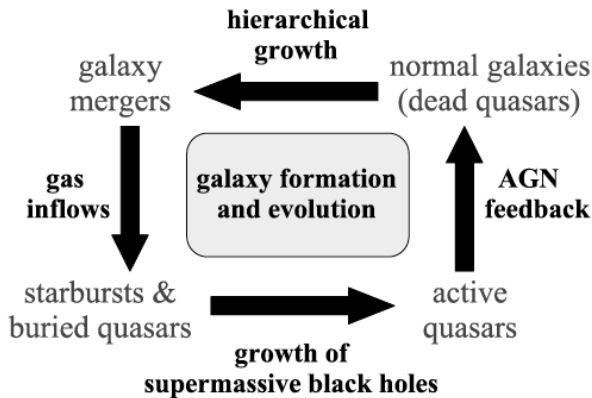

Figure 1.10 – Schematic representation of a "cosmic cycle" for galaxy formation and evolution regulated by black hole growth in mergers. Image credit: Hopkins et al. (2006).

of X-ray, UV, and optical photons. In this, UV and X-ray radiation drive the chemistry of the accreting and star-forming gas, and affect the thermodynamics of the ISM. In their work, Hopkins & Quataert (2010) find that AGN activity is more tightly coupled to nuclear star formation than to the global star formation rate of a galaxy. Furthermore, Pérez-Beaupuits et al. (2011) have estimated that the temperature of AGN molecular gas, exposed to X-rays, is a factor ~ 5 higher than gas in a starburst of equal bolometric power. This has severe consequences for star formation, which depends on the ability of interstellar gas to cool and form dense molecular clouds since the Jeans mass (M_J) scales with the temperature of the ambient gas as $M_J \propto T^{3/2}$. Moreover, X-rays have small cross-sections, hence they can penetrate large columns ($N > 10^{22}$ cm^{-2}) and thus provide information on the innermost regions of AGNs. In their work, Wada et al. (2009), include the effects of X-rays using the XDR models of (Meijerink & Spaans 2005), and show that XDR physics may change the distribution of H_2 around an AGN. They also found that the density and temperature of the torus are highly inhomogeneous, and that the velocity field is turbulent. Furthermore, Di Matteo et al. (2005) argue that a merger generates a burst of star formation and leads to strong inflows that feed gas to the SMBH and thereby power the quasar. Hence, the energy released by the quasar expels enough gas to inhibit further star formation and quenches the growth of the black hole. However, none of these studies have taken into account the effect of X-ray irradiation from the AGN onto the ambient gas, and the subsequent effects on galaxy evolution, in a self-consistent manner.

1.3.1   This Thesis

In this thesis I study the nature of dark energy, effects of UV background and X-ray radiation on the formation of the first stars, and the origin of the Magorrian relation at high redshift galaxies.

In chapter 2, we test the proposed connection between the dark energy density and the total number of macroscopic black holes in the entire universe by Spaans (1997). For this we take the type II SN rate density data from Hopkins & Beacom (2006) for $z = 0 - 6$ and use it to calculate the change in the number of type II SNe. Then by assuming that the bulk of stellar mass black holes is formed in type II SNe, we associate it to the change in the total number of black holes in the universe, which then we relate to the dark energy density of the universe.

In chapter 3 we investigate the effect of UV background radiation on the formation of a multi-phase ISM and hence the first stars. In this we perform 3D hydrodynamical simulations using tabulated PDR tables for non-zero metallicities and different UV background radiation fields. The UV background is crucial because it can dissociate H_2 and heat dust grains. Therefore, it is an important parameter in the star formation process. In our work, we consider pre-enriched minihalos with metallicities of $Z/Z_\odot = 10^{-4}$, 10^{-3}, 10^{-2}, 10^{-1} under an impinging UV radiation field of $G_0 = 10^{-1}$ and 10^{-2}. Here $G_0 = 1$, in Habing units, corre-

sponds to a flux of 1.6×10^{-3} erg cm^{-2} s^{-1}.

In chapter 4 we implement the XDR/PDR chemical network and use the Enzo radiation transport module *Moray* (Wise & Abel 2011a) to calculate the transfer of the X-ray radiation field produced by a black hole in order to study the physical conditions near an AGN. We tabulate XDR grids for a wide range of flux, density and column values and follow the radiative transfer upto a few 100 pc from the black hole. In this, we perform two simulations, one with X-rays and one without, where we insert a black hole with a mass of 5×10^4 M$_\odot$ at redshift 15 and follow the evolution for 100 Myr to study the importance of the X-ray radiation from the AGN on the star formation.

In chapter 5, we investigate how the accretion rate of central black holes evolves through cosmic time, what the effects are of X-ray irradiation from the AGN on the ambient gas, and how the relative contributions of AGN and supernova feedback onto the host galaxy evolve through time. For this, we use the modified code as discussed in chapter 4 and add a metallicity dependence as well as a star formation recipe. We run a simulation where we switch on a black hole at redshift 15 and follow its evolution until $z = 5$. These simulations enable us to study the effect of X-ray radiation on different metallicity environments, accretion flows onto the black hole, star formation and their chemical and mechanical feedback effects on the surrounding medium.

Testing the Proposed Connection Between Dark Energy and Black Holes

"Nature's purpose is to count,
patiently and persistently,
every fibre in space-time's fabric."
Marco Spaans, 2012

A. Aykutalp & M. Spaans
To be submitted 2012

Abstract

In 1997, an extension of general relativity was proposed that predicts the dark energy density Λ to vary linearly with the total number of macroscopic black holes in the entire universe. We explore this prediction and find that Λ must be roughly constant after the bulk of the stellar mass black holes are in place, so for a redshift z smaller than unity. Conversely, the highest black hole formation rate corresponds to the peak in the cosmic star formation history, earlier than $z = 1$. This yields a fast declining Λ, by a factor of about 5, from redshift 1 to 3. At even earlier times, before many stars were formed, the value of Λ should be much smaller than its current value. These predicted effects are all consistent with current data, and near future observations can definitively confirm or disprove the link between the dark energy density and the total number of black holes in the entire universe.

2.1 Introduction: Dark Energy and Theories of Gravity

The expansion of the universe appears to be accelerating, as indicated by the magnitude-redshift relation of type Ia supernovae (Amanullah et al. 2010, Perlmutter et al. 1999, 1998, Garnavich et al. 1998, Schmidt et al. 1998, Riess et al. 1998). This phenomenon is usually referred to as dark energy and constitutes one of the big mysteries in cosmology. Dark energy seems to be fundamentally connected to the dynamics of space-time itself. The simplest expression of dark energy is in the form of a positive cosmological constant term on the left hand (geometric) side of the Einstein equation. The origin of such a constant is not specified by general relativity (GR), though, leaving one with an incomplete description of space-time dynamics.

The success of Einstein gravity is overwhelming. Hence, any alternative theories should take great care in preserving the beautiful features of GR, while pursuing the mystery of dark energy. Often, creative and compelling ideas notwithstanding, ad hoc elements or unconstrained parameters and fields are part of modified gravity theories, e.g., vector-tensor theory,quintessence, M-theory, Einstein-aether theory, MOND (Jacobson & Mattingly 2001, Jacobson 2010, Zlosnik et al. 2007, Hořava 2009, Sanders 2011).

An extension of GR has been proposed in Spaans (1997), S97 from hereon. This theory leads to a unique and testable prediction for dark energy, while fully preserving GR, without the introduction of any additional degrees of freedom. The S97 paper is somewhat technical (it uses the mathematics of algebraic topology) and we therefore provide an extensive summary of its salient physical properties below.

2.2 Physical Aspects of the S97 Model

The Einstein equation has many symmetries, but it is not invariant under local conformal (scale changing) transformations. As a result, one finds larger metric fluctuations when one goes to smaller spatial scales. In fact, at the Planck scale of $l_P \sim 10^{-33}$ cm, these fluctuations in space-time become huge (even singular) and space-time should take the form of a quantum foam with Planck mass ($m_P \sim 10^{-5}$ g) black holes (BHs), so-called mini BHs, popping out off and into the vacuum (Wheeler 1957). Space-time thus enjoys the presence of mini BHs at the Planck scale, i.e., is multiply connected. A fundamental problem with the quantum foam is that it fluctuates violently on a Planck time of $t_P \sim 10^{-43.5}$ sec and is therefore difficult to conceive as a stable structure. It is important to realize here that GR is a local geometric theory. Hence, it allows for freedom in the (global) topology of space-time.

Topology studies the countable properties of geometric configurations which remain invariant under certain transformations, such as bending, stretching or

twisting. In topology, shapes or surfaces are considered to be equivalent if any continuous change can be continuously undone, this is called a homeomorphism. For example, a circle is equivalent to a square, a coffee cup is equivalent to a donut. For the donut example, see fig. 2.1, the important point is that there is one closed loop, which survives any continuous deformation. This is different from geometry, which deals with differentiable transformations (shape preserving diffeomorphisms).
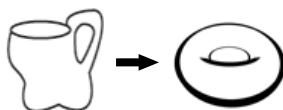

Figure 2.1 – An illustration of a homeomorphism: A continuous deformation between a donut and a coffee cup.

S97 seeks stability for the quantum foam through GR, which is the natural low energy limit of any quantum gravity theory, and space-time topology. Specifically, the Schwarzschild solution for a macroscopic BH can be used as the low energy limit of the quantum foam in a topological sense. That is, as a low energy limit that allows for changes in the geometry of space-time but one that also assures all local observers to count the same number of event horizons. I.e., the connectivity of space-time, so the topology of the event horizon, does not change if one makes a BH larger. Furthermore, such a countable quantity like the number of BHs is invariant under continuous deformations (homeomorphisms) of space-time, as above.

This kind of a low energy limit uses the fact that all BHs can be described geometrically by just their mass, charge and spin, while they all possess a closed surface as well (the event horizon), irrespective of their local geometry. Furthermore, BHs have a black body temperature (Hawking 1975) and small BHs are much warmer than large BHs (the effective temperature goes as 1/mass). However, mini BHs in the quantum foam are transient in that they are continuously created and destroyed. Hence, if GR is to be a proper low energy limit of the quantum foam (with a well defined number of event horizons for all observers), the existence of mini BHs must somehow be subject to the presence of macroscopic BHs. Afterall, only the latter can exist (much) longer than a local Hubble time under Hawking evaporation.

In S97, the quantum foam stability problem is solved by allowing only macroscopic (long lived) BHs to *induce* mini BHs in every local Planckian volume $\sim l_{\mathrm{P}}^3$. One needs to consider distinct Planckian volumes here since quantum physics

forces space-time to be quantized at the Planck scale (an observer cannot measure with a better accuracy than $\sim l_P$). These induced mini BHs are created with a (possibly time dependent) probability δ in every Planckian volume. This, currently tiny, probability δ for a single Planckian volume to enjoy the temporary presence of mini BHs must be linear in the number of macroscopic BHs (so counting event horizons) and independent of geometry (so volume). The latter property forces all local Planckian volumes in the quantum foam to respond as one to the presence of macroscopic BHs, irrespective of whether the universe is expanding (and thus adding Planckian volumes). I.e., dark energy is *purely topological* in nature and every observer witnesses the same local topological changes in the Planckian quantum foam (so space-time has uniform statistics), subject only to how the low energy GR limit drives the formation of macroscopic BHs globally.

One may think that this almost instantaneous response (within a time slice) of the dark energy everywhere to BH formation leads to causality violations, but this is not the case: In S97, the equations of motion for the topology of the universe are derived. These equations contain no spatial information and are first order in the discretized time variable $t = nt_P$, for integers $n \geq 1$ that distinguish different time slices of thickness t_P. I.e., for any time t_1 labelling the complete three-space of the universe, the solution one Planck time later only depends on the global topology at time t_1. Also, under a continuous transformation one can always deform three-space in such a manner that any two three-space points are brought within each other's vicinity. Subsequently, information on the creation of any BH can thus be brought into the vicinity of any local observer as well. Furthermore, this freedom of continuous three-space deformation assures that no such information needs to be exchanged faster than the speed of light to inform every local Planckian volume, no matter how distant from the BH, of the topology changing event. After all, the distance between the two aforementioned three-space points can be made as small as a Planck length by the deformation. One should realize here that BHs and observers are not moved physically during such continuous deformations. Rather, it is space-time itself that deforms and facilitates the transfer of BH number information through topological identifications between space-time points.

The latter can best be imagined as loops that provide short-cuts through four-space between any two points in three-space. These loops can be constructed by taking a line segment (a path) and identifying two points along it to create a loop as an alternative route. Doing this for three dimensions, one constructs a three-torus where each surface of the cube connects to the opposite one through the fourth dimension (time). Along these short-cuts information travels at maximally the speed of light, obeying local Lorentz invariance, but across arbitrary three-space distances. Creating these short-cuts through four-space between all pairs of Planckian volumes allows topological information to be exchanged causally within *the same* given time slice of thickness t_P. The resulting structure is a lattice of three-tori (see S97 for further details). Hence, wherever a BH is formed in some time slice its effect on the dark energy density in that time slice is transferred purely topologically through these identifications, without the need for causality

violations and expressed solely by an update on the total number of BHs. This testable topological aspect of dark energy augments the local geometric approach of GR, and fully preserves the latter, while it assigns countable numbers (BH horizons) to entire time slices. Time is relative of course and one may freely choose any foliation for the time slices since the number of BHs is a covariant quantity.

Because topology allows one to identify all space-time points as above, it is the total number of macroscopic BHs in the entire universe, so in all of three-space for every time slice, that is pertinent to the dark energy density. Therefore, the spatial distribution of macroscopic BHs, or the actual volume of our evolving universe, is irrelevant. In all, S97 finds the dark energy density Λ to be linearly proportional to the total number of macroscopic BHs in the entire three-volume of the universe, $N_{\mathrm{BH}}(z)$, at a given redshift z. In this, redshift is a distinctive measure of time in the usual 3 + 1 decomposition for the evolution of the three-geometry and three-topology of space-time. Algebraically,

$$\Lambda(z) = \delta(z)\frac{m_{\mathrm{P}}}{l_{\mathrm{P}}^3}, \qquad (2.1)$$

where

$$\delta(z) = N_{\mathrm{BH}}(z)\frac{l_{\mathrm{P}}^3}{l_{\mathrm{I}}^3}, \qquad (2.2)$$

and l_{I} the size of the universe (after inflation, marking the transition to the low energy GR limit) when the first BH forms that exists for longer than a local Hubble time. I.e., l_{I} is *frozen in* when the quantum foam stabilizes and each induced mini BH contributes about $m_{\mathrm{P}} \sim 10^{-5}$ g of mass per Planckian volume l_{P}^3. Equation 2.1 shows that, for $N_{\mathrm{BH}}(z)$ independent of redshift, any local observer concludes that the dark energy density Λ in g cm^{-3} remains constant as the universe expands. Conversely, the dark energy density scales linearly with the total number of macroscopic BHs that are present in the entire three-volume of the universe at a given redshift. Induced mini BHs can drive the expansion of the universe, so constitute a negative pressure, because their creation as three-dimensional spatial objects requires an increase in four-space volume to actually embed them. formed event horizon is a closed surface to an external observer.

The absolute value of Λ is only roughly estimated in S97 due to uncertainty in N_{BH} today and l_{I}. However, the exact value of Λ is not important here because this paper concentrates only on the evolution of the dark energy density with the total number of BHs in the entire universe. Of course, the observable universe may be smaller than the entire universe, which is relevant for measuring the total number of BHs through observations. If we assume that the observable universe is the entire universe, then one can estimate l_{I} as follows. Today's dark energy density is $\sim 10^{-29}$ g cm^{-3} and the universe presently contains 10^{19} macroscopic BHs. The latter number follows if one assumes that 1 in 10^3 stars yields a BH, for a Salpeter initial mass function (IMF), and that there are 10^{11} galaxies with each 10^{11} stars. Hence, with these numbers $l_{\mathrm{I}} \sim 2 \times 10^{14}$ cm.

The S97 theory provides solutions for the evolution of the very early universe's topology. The number of mini BHs increases exponentially during the quantum gravity phase of the universe (so before the first macroscopic BH is formed and the quantum foam is stabilized). Therefore, mini BHs can drive an inflationary period at these early unstable times, with a dark energy density that corresponds to about one mini BH per Planckian volume ($\delta \sim 1$).

In all, one has the local space-time quantum foam that (Wheeler 1957) envisioned, but globally constrained by the total number of macroscopic BHs in the entire universe. The value of $N_{BH}(z)$ thus controls the temporal variations in the dark energy density, in the spirit of Mach's principle, where global properties of the universe determine local ones.

2.3 Testing the Connection Between Dark Energy and Macroscopic Black Holes

The universe appears to be approximately flat based on WMAP7 cosmological observations (Komatsu et al. 2011) and Λ is about 0.734 ± 0.029 in units of the critical density $\rho_c = 1.88 \times 10^{-29}$ g cm^{-3}. As discussed above, the dark energy density of our universe is linearly proportional to the total number of macroscopic BHs in three-space at any redshift. Very practically, this means that if the number of BHs in the entire universe at redshift 1 is twice higher than at redshift 2, then Λ in g cm^{-3} doubles from $z = 2$ to $z = 1$. This paper focuses on the putative evolution in Λ. Therefore, it is only necessary to compute how the total number of BHs in the universe changes with redshift, irrespective of what the current value of Λ is.

The bulk of the stars, and thus stellar BHs in the universe appears to be present as early as $z = 1$, when a $(1 + z)^4$ decline ensues in the cosmic star formation rate (Hopkins & Beacom 2006). This is earlier than current type Ia supernova (SN) detections probe, hence one expects to find an effectively constant Λ for $z < 1$. It is relevant here that type Ia SNe occur with a delay of close to 3 Gyr relative to regular star formation. Conversely, given the rapidity with which massive stars/BHs are produced around $z = 1 - 3$, this epoch should exhibit a strong decrease in the number of BHs, and thus Λ, from $z = 1$ to $z = 3$.

These qualitative expectations can be quantified as follows. Hopkins & Beacom (2006), their figure 7, derive the comoving type II SN rate density from the star formation history of the universe. These authors adopt a type II SN mass range of 8-50 $M_\odot$ and the "BG" and "SalA" (Salpeter) IMFs of Baldry & Glazebrook (2003). We use their $z = 0 - 6$ data for a Salpeter IMF to estimate the evolution of the dark energy density from today's value back to higher redshift, in terms of the comoving type II SN rate density dn_{SN}/dt (in yr^{-1} Mpc^{-3}). In this, we assume that stellar mass BHs are produced by type II SNe with some constant efficiency ϵ. The comoving type II SN rate density is used here because such an expansion-corrected coordinate system allows one to approximate the relative change in the

total number of BHs that are formed in the universe at a given redshift, as follows.
The used data, and thus the derived evolution of $\Lambda(z)$, pertain to the observable
universe only. Hence, we assume that the observable universe gives a good statis-
tical representation of the entire universe as far as the change in the total number
of macroscopic BHs in evolving three-space is concerned. We thus seek $\Lambda(z)$ nor-
malized to its present value $\Lambda(0)$, which corresponds to the current number of
BHs in the observable universe.

The ratio $\Lambda(z)/\Lambda(0)$ can now be expressed analytically, in terms of dn_{SN}/dt for
observers that measure the rate of type II SNe in their comoving volume, as

$$\frac{\Lambda(z)}{\Lambda(0)} = \frac{\int_6^z dt(z)\, \epsilon\, dn_{SN}/dt}{\int_6^0 dt(z)\, \epsilon\, dn_{SN}/dt}, \tag{2.3}$$

and is independent of the constant BH formation efficiency ϵ. We perform the in-
tegrals in equation 2.3 for a flat cosmology and the same cosmic time interval as
used by Hopkins & Beacom (2006), $t(z) = \frac{1}{H_0}\int_0^z \frac{dz}{(1+z)[\Omega_m(1+z)^3+\Omega_\Lambda]^{\frac{1}{2}}}$. We use redshift
as a coordinate, but there is no pertinent dependence of our results on coordinate
system because of the normalization in 2.3. Any observer, whatever its coordinate
system, will find the dimensionless ratio of two numbers to be covariant. One may
worry about BHs that are formed beyond our horizon. However, as explained
above, these BHs do contribute to the dark energy density in our comoving vol-
ume, but without violating causality. At the same time, the right hand side of 2.3
is empirical. So, even though we, as observers, have a special perspective on (the
history of) the universe in our current time slice, we can still derive the change in
the total number of BHs, as three-space evolves, if we live in a representative co-
moving volume. I.e., one that enjoys the same time dependence of BH formation
as the whole universe. Figure 2.2 shows the evolution of $\Lambda(z)/\Lambda(0)$.

It is found that $\Lambda(z)/\Lambda(0)$ changes by less than $\sim 30\%$ more recently than a red-
shift of unity. Furthermore, a rapid decline in the dark energy density by a factor
of 5 occurs from $z = 1 - 3$. The shading in figure 2.2 represents the observational
uncertainty in deriving the type II SN rate from the cosmic star formation history
(Hopkins & Beacom 2006). For redshifts $z > 5$ the shading indicates that a sig-
nificant amount of star/BH formation may occur at very early times (but see the
discussion section). The value of the equation of state parameter, $w = \frac{p}{\rho}$ (for pres-
sure p and density ρ) is estimated to be $-1.023 \pm 0.09(\text{stat}) \pm 0.054(\text{sys})$ (Amanullah
et al. 2010, Astier et al. 2006) and $-1.061^{+0.069}_{-0.068}$ (Sullivan et al. 2011), for $z < 1$. In
figure 2.2, we see that $\Lambda(z)/\Lambda(0)$ is roughly constant and slightly decreasing with
increasing redshift for $z < 1$. This is consistent with observational data, because
a constant $w = -1.1$ corresponds to an allowed change in $\Lambda(z)/\Lambda(0)$ of about 30%.
The latter follows from the conservation equation

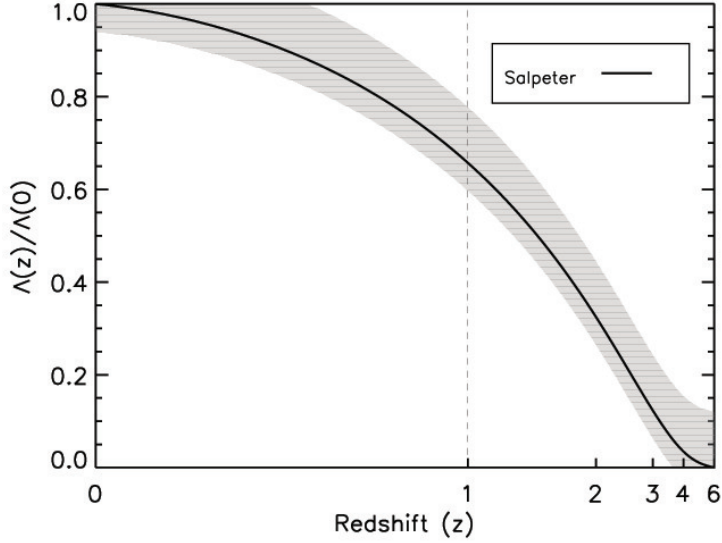$$\frac{d\rho/dt}{\rho} = -3H(1 + p/\rho) = -3H[1 + w(z)], \tag{2.4}$$

Figure 2.2 – Redshift evolution of Λ derived from the type II SN rate data of Hopkins & Beacom (2006). The shading represents the observational uncertainty in deriving the type II SN rate.

with the Hubble parameter squared $H^2 = 8\pi\rho/3$ (Linder 2003). If one expands $1 + w$ as $1 + w \approx \delta w$, the relative change in ρ over a local Hubble time is about $(H\rho)^{-1}d\rho/dt = -3\delta w$, for constant δw. Indeed, figure 2.2 shows that Λ decreases by about 30%, for a constant $w \approx -1.1$, from $z = 0$ to $z = 1$. Furthermore, the sharp drop in $\Lambda(z)$ for $z > 1$ then shows that no constant value of w can mimic dark energy behavior for $z \sim 0 - 2$ if the total number of stellar mass BHs controls the vacuum energy density. Also, Amanullah et al. (2010) point out that although $-w$ is close to unity there is room for evolution for $z > 1$. This is because the SN Ia data only weakly constrain dark energy for such early times. Similar constraints are provided by Seljak et al. (2005), based on SNe, SDSS and CMB data, as well as by Li et al. (2012), based on SN legacy survey data.

Furthermore, recent WMAP7 work by Komatsu et al. (2011), provides limits on the properties of time dependent dark energy parameterized by $w(a) = w_0 + w_a(1 - a)$ (Chevallier & Polarski 2001, Linder 2003), where a is the scale factor ($a = \frac{1}{1+z}$). In their table 4, these authors estimate $w_0 = -0.93 \pm 0.12$ and $w_a = -0.38^{+0.66}_{-0.65}$, for a flat universe. Their 13% uncertainty in w_0 is easily accommodated in our figure 2.2, while the fiducial range of w_a allows for the factor of 5 change in Λ over $z = 1 - 3$. Indeed, because the bulk of the stellar mass BHs appears not to have formed before $z = 1$, we expect to have $w < -1$ for $z > 1$.

2.4   Discussion

One can estimate the number of BHs at $z \sim 6$ from the soft X-ray background (0.5-2 keV), which is partly produced by accreting black holes at $z > 6$. This is relevant because the Hopkins et al. (2006) data stop around a redshift of 6. Dijkstra et al. (2004a) estimate an upper limit for the BH mass density of $4 \times 10^4 \, M_\odot \, \mathrm{Mpc}^{-3}$. This translates into 10^{14} BHs for the observable universe at $z \sim 6$, if the Pop III IMF is dominated by stars of $10 - 100 \, M_\odot$ (Bromm et al. 2002, Abel et al. 2002). This is orders of magnitude smaller than the number of BHs in the observable universe at $z = 0$, $N_{\mathrm{BH}} \sim 10^{19}$. Since the bulk of the stellar mass BHs is not assembled at $z > 5$, stellar origin BHs should play no role in the dark energy density at those early times.

A top-heavy IMF may aid the formation of BHs. Studies by Hocuk & Spaans (2010, 2011) indicate that star formation within $r_c = 100(M/10^7 M_\odot)^{1/2}$ pc of a supermassive ($M > 10^5 \, M_\odot$) BH, accreting at 10% of Eddington, leads to a top-heavy IMF with as much as 5-10% of all stars formed being more than $8 \, M_\odot$. This can provide an additional boost to the BH production rate at $z > 2$ when quasars accrete rapidly, while also being consistent with the SN neutrino constraints for $z < 1$ (Hopkins & Beacom 2006). If obscured infrared and sub-mm bright high-redshift galaxies harbor a large (50%) fraction of all star formation in the early universe (for $z \sim 2 - 3$), then the peak in the cosmic type II SN rate may be higher and wider than expected (Casey et al. 2011). Subsequently, this would cause a factor of about 2 higher $\Lambda(z)/\Lambda(0)$ than shown by the grey area in figure 2.2 around $z \sim 3$.

Of course, mergers between BHs may suppress the total number of macroscopic BHs, and thus the magnitude of Λ. The merger rate of stellar mass BHs, which form the bulk of the BH population in the universe (rather than supermassive ones), in BH-BH binaries, is about $500 \, \mathrm{yr}^{-1}$ (O'Leary et al. 2007). Given that presently roughly 3 BHs are formed per second in the observable universe, assuming again that about 0.1% of all formed stars yield a BH (for a Salpeter IMF), this is unlikely to decrease Λ significantly.

The present number of BHs in the universe could be declining if numerous primordial black holes were created during the quantum gravity phase of the universe and are evaporating around this time (Page & Hawking 1976). Such primordial BHs can survive, and dominate by number today, only if they are more massive than $M_0 \sim 2 \times 10^{15}$ g. For $M > M_0$, primordial BHs withstand Hawking evaporation for more than a local Hubble time since the latter scales $\propto M^3$. However, it is likely that the mass function of primordial BHs scales more steeply than $1/M$. Consequently, the total number of primordial BHs declines with cosmic time (S97). This would lead to a strongly diminishing Λ with decreasing redshift, inconsistent with current observational constraints.

High precision measurements of w, w_0 and w_a, as cited in the great efforts above, will continue to decrease their error bars to the few percent level for $z < 1$ type Ia SNe. They can thus probe the modest but real decrease in Λ shown in figure 1 for $z = 0 - 1$. Furthermore, a combination of type Ia SNe, galaxy clus-

tering and weak lensing may be quite powerful to constrain systematics in this (Wang 2012). Of course, the bulk of the evolution in Λ lies at $z > 1$. In this light, it has been shown recently that active galactic nuclei (AGN) can be used for high redshift (upto $z \sim 4$) measurements of dark energy, using reverberation mapping (Watson et al. 2011). This novel, and very timely, technique is particularly well suited to sample the $\Lambda(z)/\Lambda(0)$ curve for $z = 1 - 3$, because AGN can be seen to much higher redshift than type Ia SNe. This method could thus also confirm or disproof the linear scaling between the dark energy density and the total number of macroscopic BHs.

The Complexity that the First Stars Brought to the Universe: Fragility of Metal Enriched Gas in a Radiation Field

"It is the stars, The stars above us, govern our conditions".
William Shakespeare, King Lear, Act IV, Scene 3

Chapter 3 – THE COMPLEXITY THAT THE FIRST STARS BROUGHT TO THE
UNIVERSE: FRAGILITY OF METAL ENRICHED GAS IN A RADIATION FIELD

Abstract

The initial mass function (IMF) of the first (Pop III) stars and Population II (Pop II) stars is poorly known due to a lack of observations of the period between recombination and reionization. In simulations of the formation of the first stars, it has been shown that, due to the limited ability of metal-free primordial gas to cool, the IMF of the first stars is a few orders of magnitude more massive than the current IMF. The transition from a high-mass IMF of the first stars to a lower-mass current IMF is thus important to understand. To study the underlying physics of this transition, we performed several simulations using the cosmological hydrodynamic adaptive mesh refinement code Enzo for metallicities of 10^{-4}, 10^{-3}, 10^{-2}, and 10^{-1} $Z_\odot$. In our simulations, we include a star formation prescription that is derived from a metallicity dependent multi-phase interstellar medium (ISM) structure, an external UV radiation field, and a mechanical feedback algorithm. We also implement cosmic ray heating, photoelectric heating, and gas–dust heating/cooling, and follow the metal enrichment of the ISM. It is found that the interplay between metallicity and UV radiation leads to the coexistence of Pop III and Pop II star formation in non-zero metallicity ($Z/Z_\odot \geq 10^{-2}$) gas. A cold ($T < 100$ K) and dense ($\rho > 10^{-22}$ g cm^{-3}) gas phase is fragile to ambient UV radiation. In a metal-poor ($Z/Z_\odot \leq 10^{-3}$) gas, the cold and dense gas phase does not form in the presence of a UV radiation field of $F_0 \sim 10^{-5} - 10^{-4}$ erg cm^{-2} s^{-1}. Therefore, metallicity by itself is not a good indicator of the Pop III–Pop II transition. Metal-rich ($Z/Z_\odot \geq 10^{-2}$) gas dynamically evolves two to three orders of magnitude faster than metal-poor gas ($Z/Z_\odot \leq 10^{-3}$). The simulations including supernova explosions show that pre-enrichment of the halo does not affect the mixing of metals.

3.1   Introduction

In the last two decades, cosmological simulations have become an important tool for theoreticians to simulate the structure formation in the universe from the primordial density fluctuations. The cosmological model that currently matches the observations of the cosmic microwave background (CMB) best is the so-called cold dark matter (CDM) model. According to hierarchical structure formation (Press & Schechter 1974), small clumps are the first to collapse and form structures, and then through mergers and the accretion of matter they build up larger structures. Cosmological simulations, based on the CDM model of hierarchical structure formation, predict that the first stars $(30-300 M_\odot)$ have formed at redshifts z $\sim 20-30$, in dark matter halos with masses of $\sim 10^6 \, M_\odot$ (Tegmark et al. 1997, Abel et al. 2002, Bromm et al. 2002, Yoshida et al. 2003, O'Shea & Norman 2007).

In the current literature, the first stars are called Population III (Pop III) stars. The metallicity of Pop III stars is so low that metal cooling does not have any effect on their formation. In the simulations of the formation of Pop III stars, it has been shown that, due to the limited ability of metal-free primordial gas to cool, the initial mass function (IMF) of Pop III stars is a few orders of magnitude more massive than the current IMF (Abel et al. 2002, Yoshida et al. 2006, Bromm et al. 2002). More recently, it has been suggested that Pop III stars are not necessarily that massive and can be in the range $10-100 \, M_\odot$ (Tumlinson 2006, 2007a,b, Hosokawa et al. 2011). On the other hand, from observations of the nearby universe we know that the present day stellar mass scale is $\sim 0.3 \, M_\odot$ (Kroupa 2002, Chabrier 2003).

The chemistry of zero metallicity (primordial) gas has been studied by a number of authors (Dalgarno & Lepp 1987, Abel et al. 1997, Galli & Palla 1998, Abel et al. 2001, Glover 2008, Glover & Abel 2008, Turk et al. 2011a). Once the gas has virialized in the potential wells of dark matter halos, additional cooling is required for the further collapse of the gas and to form stars. The formation of a star depends on the ability of interstellar gas to cool and form dense molecular clouds. The modest cooling ability of primordial gas leads to high masses for Pop III stars. The cooling efficiency of star forming gas will be significantly affected by the addition of radiation and metals after the formation of the first stars. Hence, the chemical composition and the radiation environment of interstellar gas are the key parameters to study.

The main coolants for primordial gas with temperatures $T \geq 10^4$ K are Lyα emission of neutral atomic hydrogen (H I, 1216 Å), and ionized helium (He II, 304 Å). Below this temperature, the dominant coolant in primordial gas is molecular hydrogen (H_2). Saslaw & Zipoy (1967) realized the importance of gas phase H_2 formation in a primordial gas for the formation of protogalactic objects. At low densities ($n < 10^8$ cm^{-3}), H_2 can form via intermediate ions H_2^+ and H^-. The cooling rate of H_2 (Λ_{H_2}) scales with density as $\Lambda_{H_2} \propto n^2$ at low densities ($n < 10^4$ cm^{-3}), where radiative de-excitation dominates, and as $\Lambda_{H_2} \propto n$ at high densities ($n > 10^4$ cm^{-3}), where collisional de-excitation dominates. Molecular hydrogen does not have a

permanent electric dipole moment while the hydrogen deuteride (HD) molecule
does, which makes HD a better coolant than H_2. Although the primordial deu-
terium abundance is small relative to hydrogen ($n_D/n_H = 4\times10^{-5}$), chemical frac-
tionation leads to an enhancement of the ratio, $n_{HD}/n_{H_2} \approx 10^{-3}$ (Puy et al. (1993),
Galli & Palla (1998), Stancil et al. (1998)). If primordial gas is significantly ionized
then HD cooling can lower the temperature to the level of the CMB at $z \sim 10 - 20$
(Johnson & Bromm 2006).

When the first stars form, the universe becomes much more complex. Accord-
ing to their initial masses, they will either explode as core-collapse supernovae
($10M_\odot < M_* < 140M_\odot$) or as pair instability supernovae (PISN; $140\ M_\odot < M_* <$
$260\ M_\odot$, Heger & Woosley (2002)). Through these supernova explosions (SNe), the
interstellar medium (ISM), and the intergalactic medium (IGM) will be enriched
with metals. From that point on one has to take into account the cooling from
the fine-structure lines of metals and the rotational transitions of molecules like
CO. Moreover, gas–dust heating/cooling can be important as well, in the sense
that dust grains will be heated to at least the CMB temperature. Dust allows the
efficient formation of H_2 and HD (Cazaux & Spaans 2004, 2009), and may colli-
sionally heat/cool the gas depending on the sign of gas temperature minus dust
temperature (Schneider et al. 2002). Also, dust grains attenuate UV radiation. For
$z > 10$, CMB photons can be an excitation source (radiative pumping) of atomic
and molecular levels (Smith et al. 2009). This allows the CMB temperature to act
as a thermodynamic floor, below which gas cannot cool, provided that collisional
de-excitation dominates the removal of population from excited states (Spaans
& Silk (2000, 2005)). Furthermore, SNe will initiate shock waves that propagate
through the ISM. These shock waves can heat up the ISM and cause a delay in the
formation of the next generation of stars or can compress the gas, which makes it
collapse and hence give rise to further star formation (Bromm et al. 2003, Springel
& Hernquist 2003, Whalen et al. 2008) .

The aim of this work is to (1) compute at what metallicity a cold and dense gas
phase emerges and (2) assess the sensitivity of this phase to background UV radi-
ation. This paper is structured as follows. In Section 3.2, we detail our cosmolog-
ical/hydrodynamic simulation. Specifically, we discuss the relevant cooling and
heating processes for star formation and the global characteristics of early star for-
mation in primordial galaxies. In Section 3.3, we highlight the implications of our
findings. Finally, in Section 3.4 we discuss our results and present our conclusions.

3.2   Simulations

In this work, we use the cosmological adaptive mesh refinement code Enzo (Bryan
& Norman 1997, O'Shea et al. 2004). We perform simulations in a three-dimensional
periodic box with a side length of 1 $h^{-1}Mpc$, initialized at z = 99. The size of the
root grid is 128^3 with three nested subgrids, each refined by a factor of two. The

finest grid has an effective resolution of 1024^3 with a side length of 125 $h^{-1}kpc$. This resolution results in a dark matter and baryonic matter resolution of 2 and 0.4 $M_\odot$, respectively. Refinement is restricted to the finest grid and occurs during the simulations whenever the baryonic matter, or dark matter density, is greater than the mean density by a factor of four or eight, respectively. The maximum level of refinement that is reached in the finest grid is eight. Refinement occurs such that the Jean length is always resolved by at least eight cells, this ensures that we meet the Truelove criterion, which requires the Jeans length to be resolved by at least four cells on each axis (Truelove et al. 1997). The virial mass of our progenitor halo at redshift z = 21 is $M_{vir} = 3.4 \times 10^6$ $M_\odot$, where M_{vir} is the mass in a sphere that encloses an average dark matter overdensity of 200. We use Wilkinson Microwave Anisotropy Probe five-year cosmological parameters (Komatsu et al. 2009), which have the following values: $\Omega_\Lambda = 0.7208$, $\Omega_m = 0.233$, $\Omega_b = 0.0462$, $\sigma_8 = 0.9$, and $h = 0.701$. Here, Ω_Λ is the vacuum energy, Ω_m is the matter density, Ω_b is the baryon density, σ_8 is the variance of random mass fluctuations in a sphere of radius 8 h^{-1} Mpc, and h is the Hubble parameter in units of 100 km s^{-1} Mpc^{-1}. We focus on a single halo with a dark matter mass of $\sim 10^9$ $M_\odot$ at $z \sim 5$ which is expected to be a typical mass for the halo population at that redshift.

For the analysis of our cosmological simulations we use YT, a cross-platform analysis toolkit written in Python(Turk 2008, Turk et al. 2011b).

3.2.1 Cooling and Heating Processes in the ISM

Metal enriched gas cools more efficiently by fine-structure lines of [C II] (157.74 μm), [O I] (63.18 μm, 145.5 μm), [Si II] (34.8 μm), [Fe II] (25.99 μm, 35.35 μm), and rotational lines of CO than by HD or H_2 emission (Santoro & Shull 2006). In the outermost layers of a star-forming cloud, the so-called photon dominated region (PDR), temperatures can increase up to 1000 K due to a strong UV radiation field, and cooling results from the fine-structure lines of [C II] and [O I]. Deeper into the cloud, the temperature decreases to $\sim$ 30 K through the balance between cosmic ray and dust heating and low-J CO rotational line cooling.

In our simulations, the gas is homogeneously pre-enriched to some non-zero metallicity at redshift of z = 30. We perform a series of simulations using cooling models for four different metallicities, 10^{-4}, 10^{-3}, 10^{-2}, and 10^{-1} $Z_\odot$, derived from the chemical network of Meijerink & Spaans (2005). In their PDR code, they include cooling from fine-structure lines of carbon (C^+ and C), oxygen (O), molecular lines from species like carbon monoxide (CO), H_2, HD, and water (H_2O). All level populations are computed under statistical equilibrium and the chemistry includes gas phase and grain surface formation of H_2 and HD (Cazaux & Spaans 2004, 2009) and line trapping using the multi-zone escape probability method of Poelman & Spaans (2005). The cooling tables that we use, depend on FUV radiation field strength, ambient gas velocity dispersion, temperature, metallicity, and H_2 abundance. As such, they provide an accurate treatment of the thermal

and chemical balance of low-metallicity PDRs. The radiation field strength (G_0) here is the flux between 6–100 eV and it extends beyond 13.6 eV according to a starburst99 spectrum for a Salpeter IMF, i.e., the H II region is computed as part of the PDR. Typically, the UV flux diminishes very quickly beyond 13.6 eV. The cooling tables enjoy a range in irradiation ($G_0 = 10^{-2}, 10^{-1}, 10^0, 10^1, 10^2, 10^3, 10^4$), H_2 abundance ($f_{H_2} = 10^{-5}, 10^{-4}, 10^{-3}, 10^{-2}, 10^{-1}, 0.2, 0.4, 0.5$) and metallicity ($10^{-4}$, $10^{-3}, 10^{-2}, 10^{-1}, 1\ Z_\odot$). We adopt Milky Way like abundance ratios based on the values of Asplund et al. (2005) and Jenkins (2004). A summary of our simulations is listed in Table 3.2.

At high column densities cooling and heating can be suppressed due to optical depth and dust opacity effects. In the case of an optically thick medium, a large part of the emitted photons are thus reabsorbed. This results in a lower critical density where the critical density is defined as the density at which the radiative de-excitation rate equals the collisional de-excitation rate. At densities much below the critical density ($n \ll n_{cr}$), radiative de-excitation dominates over collisional de-excitation, whereas at high densities ($n > n_{cr}$), collisions dominate the de-excitation process and the gas is in local thermodynamic equilibrium (LTE). Radiation is trapped if the opacity is concentrated on small physical scales which is the case in our simulations for the warm and dense gas. Since we do not resolve these PDR sub-structures in our simulations we approximate these opacity effects as follows.

We adopt a turbulent coherence length L of 0.3 pc and a local turbulent velocity dispersion of $dV = 3$ km s^{-1} to mimic the properties of a turbulent region. This yields a formal velocity gradient dV/L for scales larger than L. When the cooling is either optically thin ($\tau \ll 1$) or optically thick ($\tau \gg 1$) the choice of dV and L is not important. For the radiative transfer in the cooling lines (under statistical equilibrium), we use the multi-zone escape probability code of Poelman & Spaans (2005) . Each zone in a PDR is treated this way, and a correction to the cooling and heating rates due to line trapping and optical depth effects is derived. See Wada et al. (2009) for more details.

For an incident UV radiation field, photo-electric emission from (small) dust grains and polycyclic aromatic hydrocarbons is the dominant heating source in the neutral ISM. Dust grains can absorb an FUV photon which leads to the ejection of an electron, carrying some of the photon energy away in the form of kinetic energy. Then, through elastic collisions this excess kinetic energy heats up the gas. In our simulations we add photoelectric heating through

$$\Gamma_{\text{grain}} = 10^{-24} \epsilon G'_{0,\text{dust}} n_H \text{ erg cm}^{-3} \text{ s}^{-1}. \tag{3.1}$$

Here, $G'_{0,dust}$ is the radiation field attenuated by dust absorption and is given by

$$G'_{0,dust} = G_0 \exp(-1.8 A_v) \tag{3.2}$$

where $G_0 = 1$, in Habing units, corresponds to a flux of 1.6×10^{-3} erg cm^{-2}s^{-1}, A_v is the line-of-sight visual extinction at optical wavelengths caused by interstellar

dust and the total number density of hydrogen is, $n_{\rm H} = n({\rm H}) + 2n({\rm H_2})$ (Bakes & Tielens 1994, Meijerink & Spaans 2005). ϵ is the heating efficiency, dependent on G_0, the kinetic gas temperature T_k, and the electron density n_e as $G_0 T_k^{1/2}/n_e$, and is given by

$$\epsilon = \frac{4.87 \times 10^{-2}}{[1 + 4 \times 10^{-3}(\frac{G_0 T_k^{1/2}}{n_e})^{0.73}]} + \frac{3.65 \times 10^{-2}(\frac{T_k}{10^4})^{0.7}}{[1 + 2 \times 10^{-4}(\frac{G_0 T_k^{1/2}}{n_e})]}. \tag{3.3}$$

On the other hand, gas and dust temperatures are not equal in the ISM. At high number densities, $n_H > 10^{4.5} (\frac{Z}{Z_\odot})^{-1}$, gas–dust heating/cooling becomes important and therefore we add gas–dust heating/cooling into our simulations as given by (Meijerink & Spaans 2005);

$$\Gamma_{\rm coll} = 1.2 \times 10^{-31} {\rm n}_{\rm H}^2 (\frac{T_k}{100})^{1/2} (\frac{1000\text{\AA}}{a_{\rm min}})^{1/2} \times [1 - 0.8 \exp(\frac{-75}{T_k})](T_d - T_k), \tag{3.4}$$

where T_d is the dust temperature, T_k is the gas temperature, and a_{min} is the minimum grain size which we take as 1 μm (Nozawa et al. 2003).

Deeper into a cloud the UV radiation is attenuated by dust and cosmic ray heating becomes important. Ionization by cosmic rays produces energetic electrons. Glassgold & Langer (1973) and Cravens & Dalgarno (1978) calculated that about 8 eV of heat is deposited in a molecular gas per primary ionization. Including helium ionization, Tielens & Hollenbach (1985) find for the heating rate

$$\Gamma_{\rm CR} = 1.5 \times 10^{-11} \zeta {\rm n}({\rm H_2}) \text{ erg cm}^{-3} \text{ s}^{-1}, \tag{3.5}$$

where ζ is the cosmic ray ionization rate per H_2 molecule. In our simulations, we scale ζ with the derived star formation rate (SFR) of our simulations such that for an SFR of 1 $M_\odot$ yr^{-1} and a Salpeter-like IMF between 1 and 100 $M\odot$, we take ζ to be 3×10^{-17}s^{-1} (Spaans & Silk 2005).

3.2.2 Star Formation

In order to understand the underlying physics of the transition from a high-mass IMF of Pop III stars to a lower mass current IMF we have run simulations for different metallicities and different UV radiation backgrounds and have incorporated the metal yields of SNe.

In our simulations where star formation is included, a star particle is formed when a grid cell has a density exceeding 0.01 cm^{-3} and a temperature below 10^4 K. We follow the hydrodynamic transport of metals produced by the SNe to the enrichment of halos. We do not use the chemical network of Enzo, except for the non-equilibrium formation of H_2 (rate equation method of Anninos et al. (1997)) but our $\Lambda(G_0, f_{H_2}, Z/Z_\odot)$ cooling tables instead.

In order to compute the metal yield by the first stars we need to decide on

Table 3.1 – Simulation Parameters

Run	L (Mpc)	Metallicity $z_\odot$	SFFB	G_0 Habbing
Z1-G1	1	10^{-1}	No	10^{-2}
Z2-G1	1	10^{-2}	No	10^{-2}
Z3-G1	1	10^{-3}	No	10^{-2}
Z4-G1	1	10^{-4}	No	10^{-2}
Z1-G10	1	10^{-1}	No	10^{-1}
Z2-G10	1	10^{-2}	No	10^{-1}
Z3-G10	1	10^{-3}	No	10^{-1}
Z4-G10	1	10^{-3}	No	10^{-1}
ZS2	1	10^{-2}	Yes	10^{-2}
ZS4	1	10^{-4}	Yes	10^{-2}

Table 3.2 – Column 1: Simulation name; Column 2: Simulation box size; Column 3: Simulation pre-enrichment; Column 4: Star formation and feedback; Column 5: UV background strength.

some parameters like the mass of the halo, IMF of the first stars, star formation efficiency, and the number of SNe. From their simulations of pre-galactic structure formation, Machacek et al. (2001) determined that the minimum mass of a halo that hosts a massive primordial star is

$$\frac{M_{min}}{M_\odot} = \exp(\frac{f_{cd}}{0.06})(1.25 \times 10^5 + 8.7 \times 10^5 F_{LW,-21}^{0.47}), \qquad (3.6)$$

where M_{min} is the minimum halo mass that contains a cold dense core; f_{cd} is the fraction of gas that is cold ($T < 0.5\ T_{vir}$) and dense ($\rho > 330\ \mathrm{cm}^{-3}$), and F_{LW} is the flux within the Lyman–Werner (LW) bands in units of $10^{-21}\ \mathrm{erg\ s}^{-1}\ \mathrm{cm}^{-2}\ \mathrm{Hz}^{-1}$. We choose $f_{cd} = 0.02$ for a typical UV background of $J = 10^{-21}\ \mathrm{erg\ s}^{-1}\ \mathrm{cm}^{-2}\ \mathrm{Hz}^{-1}\ \mathrm{sr}^{-1}$, so that a halo with a minimum mass of $4.16 \times 10^6\ M_\odot$ can support cold dense gas which will eventually form a primordial star. Note here that $J = J_{-21}$ corresponds to a total UV flux of $F_0 \simeq 4 \times 10^{-5}\ \mathrm{erg\ s}^{-1}\ \mathrm{cm}^{-2}$ or $G_0 \simeq 2.5 \times 10^{-2}$. For a Salpeter like IMF, $G_0 \simeq 1$ corresponds to an SFR of about 3 $M_\odot\ \mathrm{yr}^{-1}\ (10\ \mathrm{kpc})^{-2}$.

High redshift, low mass galaxies are conjectured to have properties similar to those of local dwarf galaxies. In these galaxies the star formation efficiency, $f_\star$, ranges from 0.02 to 0.08 (Taylor et al. 1999). In this work we take $f_\star = 0.05$.
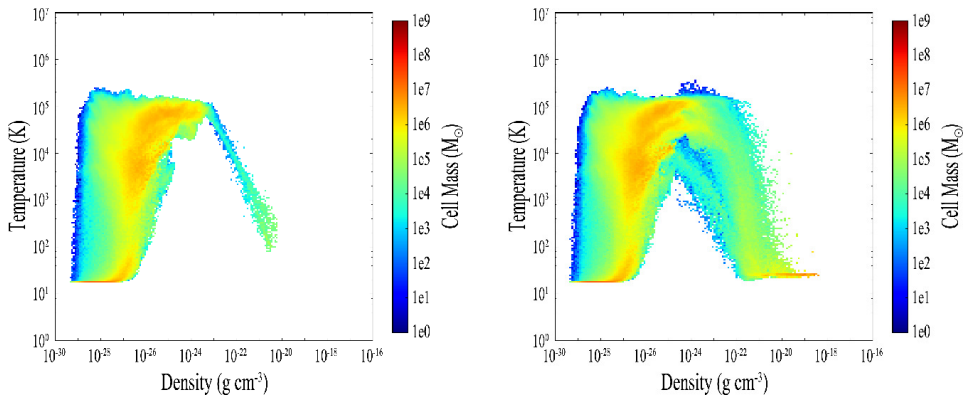
Figure 3.1 – Density–temperature profile of the central 50 kpc of a halo at redshift z ∼ 5 for metallicities of $Z/Z_\odot = 10^{-4}$ (left) and $Z/Z_\odot = 10^{-2}$ (right) for a radiation field of $G_0 = 10^{-2}$.

3.3 Results

3.3.1 Multi-phase ISM

In our cosmological simulations for the Z2–G1 and Z4–G1 runs we find (as expected) that gas in the high-metallicity case cools down to lower temperatures and has higher densities than in the low-metallicity case. This is shown in Figure 3.1 where we plot the density–temperature profile of a halo at redshift z ∼ 5 for metallicities of $Z/Z_\odot = 10^{-4}$ (left) and $Z/Z_\odot = 10^{-2}$ (right) and a radiation field of $G_0 = 10^{-2}$. In the high-metallicity case there is more gas in the central 50 kpc. This is because the cooling is more efficient, so that the gas has less pressure support against gravity and the halo accretes more material. When we look at the high densities ($\rho > 10^{-23}$ g cm^{-3}) in these plots it is clear that in the high-metallicity case there is a lot more gas at low temperatures than in the low-metallicity case. This gas is identified as the cold and dense gas phase of the multi-phase ISM. The key feature here is that the redshift at which a multi-phase ISM is established depends on metallicity. This is shown in Figure 3.2 where we plot the density–temperature profile of the same halo as shown in Figure 3.1 at z ∼ 20 for metallicities of $Z/Z_\odot = 10^{-4}$ (left) and $Z/Z_\odot = 10^{-2}$ (right). We see here that the cold dense phase is completely lacking in the Z4–G1 run whereas it is already present in the Z2–G1 run. This means that metal-rich gas cools more efficiently and therefore the multi-phase ISM is established at earlier times in the higher metallicity case than in the lower metallicity case. These results are consistent with those of Jappsen et al. (2009), although they did not include background UV radiation.

Due to the shorter cooling time a halo in the metal-rich case evolves dynamically faster and becomes more compact at z = 5 compared to a metal-poorer halo. The effect of metallicity on a halo can be seen in Figure 3.3, which shows slices of
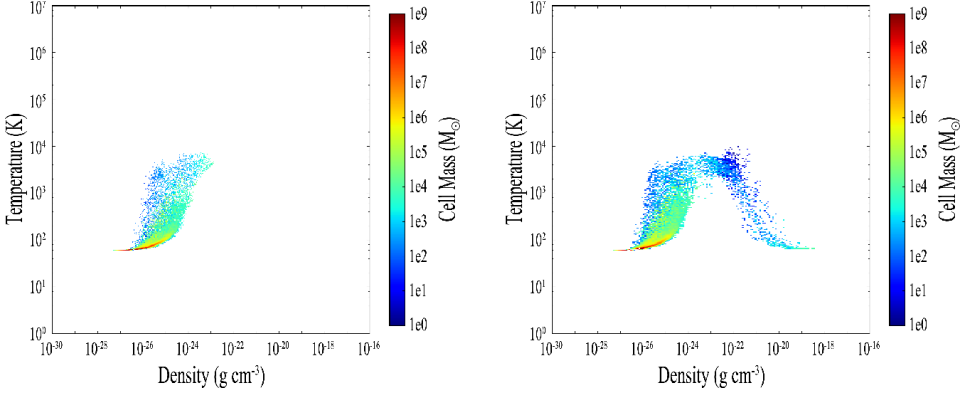
Figure 3.2 – Density–temperature profile of the central 50 kpc of a halo at redshift z ∼ 20 for metallicities of $Z/Z_\odot = 10^{-4}$ (left) and $Z/Z_\odot = 10^{-2}$ (right) for a radiation field of $G_0 = 10^{-2}$.

the density, temperature, and the Jeans mass (M_J) of the central 1 kpc of a halo for the Z4–G1 (top), Z2–G1 (middle), and Z1–G1 (bottom) runs in the x–z (left column) and x–y (right column) planes at redshift 5. We compute the Jeans mass as

$$M_J = \left(\frac{5k_bT}{G\mu m_H} \right)^{3/2} \left(\frac{3}{4\pi\rho} \right)^{1/2} , \qquad (3.7)$$

where ρ is the mass density, G is the gravitational constant, k_b is the Boltzmann constant, T is the temperature, μ is the mass per particle, and m_H is the hydrogen mass. Because the high-metallicity gas ($Z/Z_\odot \geq 10^{-2}$) cools to lower temperatures, the Jeans mass in those runs is two orders of magnitude smaller than in the low-metallicity ($Z/Z_\odot = 10^{-4}$) case. We also see that the Jeans masses for metallicities $Z/Z_\odot = 10^{-2}$ and $Z/Z_\odot = 10^{-1}$ are comparable. This is because above a metallicity of about $Z/Z_\odot = 10^{-2}$ the cooling efficiency of ambient gas no longer increases strongly with a rise in metallicity (Spaans & Meijerink 2008). In Figure 3.4, we plot the density–temperature profile of the central 50 kpc of a halo at $z \sim 5$ for the Z1–G1 run. The phase diagrams of the runs Z1–G1 (Figure 3.4) and Z2–G1 (Figure 3.1, right) are indeed similar.

3.3.2   UV Background Radiation

In order to see the effect of a UV radiation field on the evolution of gas we performed multiple simulations with different background radiation fields for the same metallicity. In Figure 3.5, we plot the density–temperature profile of the central 2 kpc of a halo at $z \sim 8$ for metallicities of $Z/Z_\odot = 10^{-3}$ (top) and $Z/Z_\odot = 10^{-2}$ (bottom) with two different background radiation fields of $G_0 = 10^{-2}$ (left) and
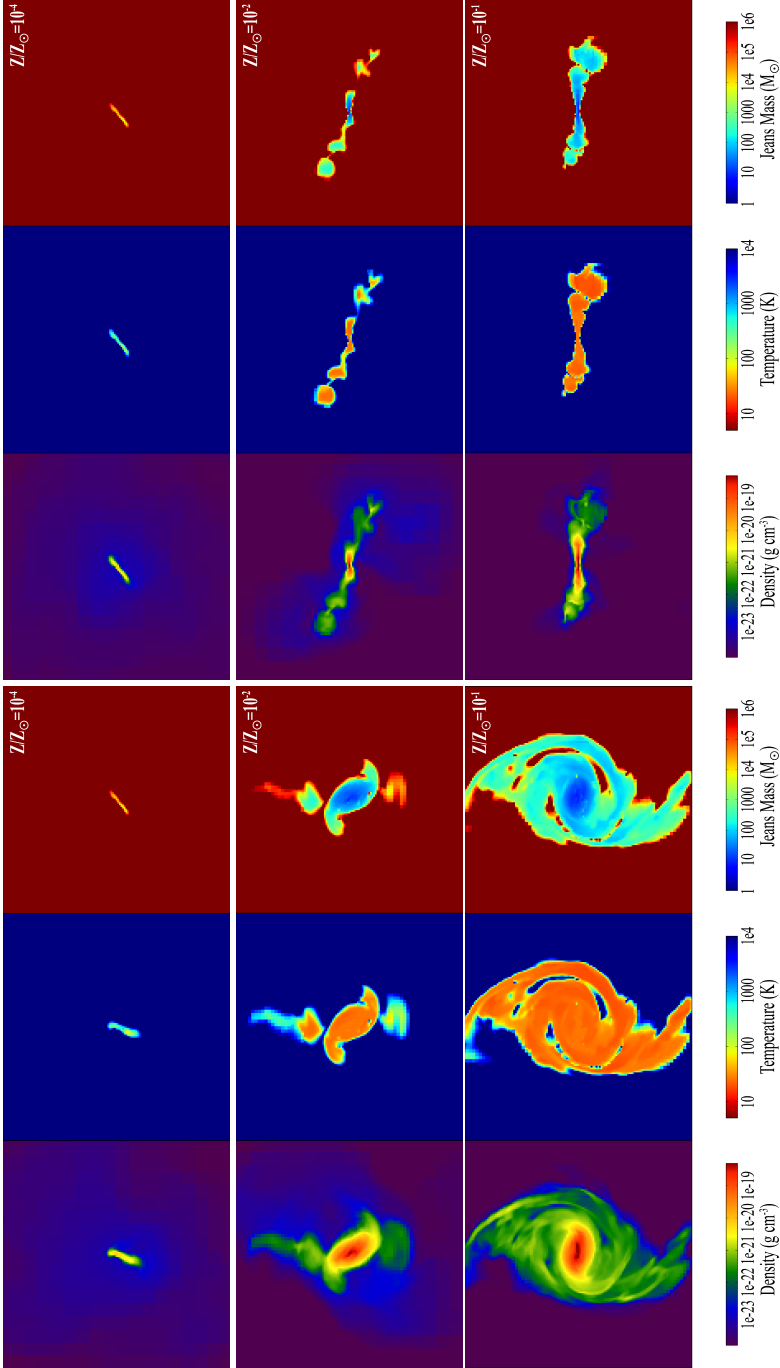
Figure 3.3 – From left to right: Slices of density, temperature and Jeans mass of the central 1 kpc of a halo at redshift 5 for metallicities of $Z/Z_\odot = 10^{-4}$ (top), $Z/Z_\odot = 10^{-2}$ (middle), and $Z/Z_\odot = 10^{-1}$ (bottom) in the x-z (left column) and x-y (right column) plane for a radiation field of $G_0 = 10^{-2}$.
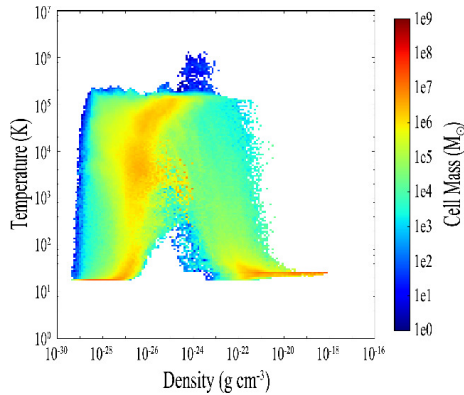
Figure 3.4 – Density-temperature profile of the central 50 kpc of a halo at redshift z ∼ 5 for
a metallicity of $Z/Z_\odot = 10^{-1}$ and a radiation field of $G_0 = 10^{-2}$.

$G_0 = 10^{-1}$ (right). When we increase the radiation field for a metallicity of $Z/Z_\odot =$
10^{-3}, the cold and dense phase does not form anymore, which is clearly seen in
the phase diagrams of Figure 3.5 : At densities above $\rho = 10^{-23}$ g cm^{-3} there is no
cold gas present anymore in the Z3-G10 run (top right). This is because gas can-
not cool down as efficiently as in the lower radiation field case due to more heat
input and dissociation of H_2 and CO. Thus, the halo takes more time to collapse
and become condensed. In our simulations we followed the halo until redshift
z = 5, and in the Z3–G10 run the gas has still not collapsed at this redshift. On
the other hand, in the $Z/Z_\odot = 10^{-2}$ case the cold dense phase survives regardless
of irradiation. This indicates that the cold dense phase is fragile to UV radiation
for metallicities of $Z/Z_\odot \leq 10^{-3}$ and robust to UV radiation for metallicities of $Z/Z_\odot$
$\geq 10^{-2}$.

As is shown in Figure 3.6, where we plot the density profile of the central 2
kpc of a halo for the Z3–G1 (top left), Z3–G10 (top right), Z2–G1 (bottom left),
and Z2–G10 (bottom right) runs, the effect of UV irradiation on the model galaxy
morphology is large for $Z/Z_\odot = 10^{-3}$ and quite modest for $Z/Z_\odot = 10^{-2}$. In fact, we
see that in the case of low metallicity and strong radiation field (Z3–G10, top right)
the compact disk-like structure is no longer formed, while in the higher metallic-
ity and strong radiation field (Z2–G10, bottom right) the disk-like structure is still
present. This is because the high-metallicity gas is able to cool faster so that it
collapses and reaches higher densities earlier in its evolution, and thus builds up
column density to protect the cold and dense phase.

In Figure 3.7, we plot the redshift at which a multi-phase ISM is established
depending on the metallicity and the radiation field. We find that, to first order,
the cold and dense phase survives if the ratio F_0/Z is smaller than ∼ 10^{-2} erg cm^{-2}
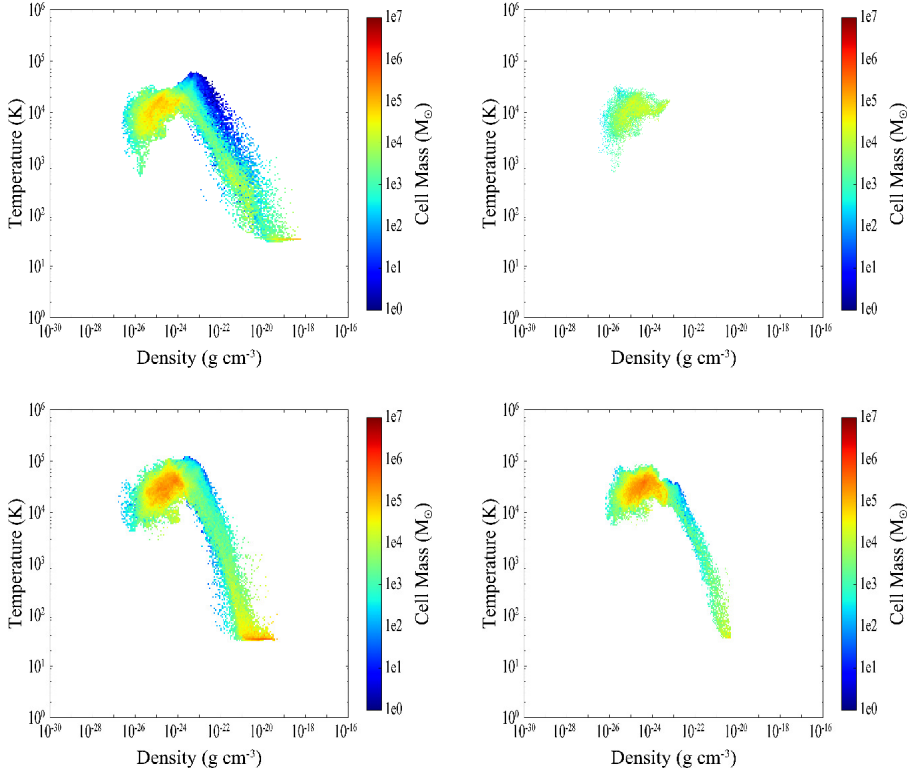s^{-1} in solar units.

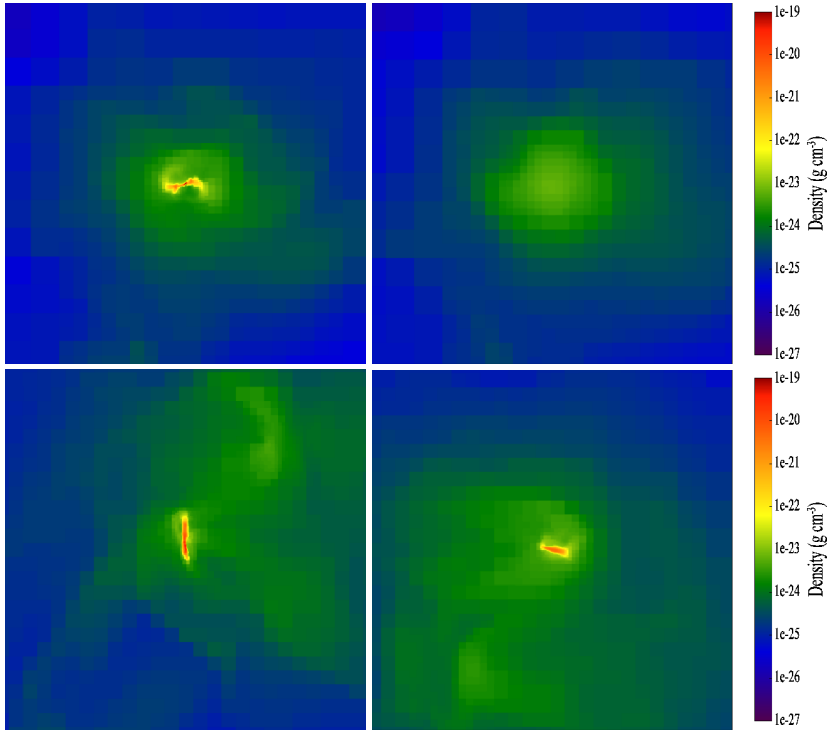**Figure 3.5** – Density–temperature profile of the central 2 kpc of a halo at zz = 7.88 for a metallicity of $Z/Z_\odot = 10^{-3}$ with radiation fields of $G_0 = 10^{-2}$ (top left) and $G_0 = 10^{-1}$ (top right), and a metallicity of $Z/Z_\odot = 10^{-2}$ with radiation fields of $G_0 = 10^{-2}$ (bottom left) and $G_0 = 10^{-1}$ (bottom right).

All this has a significant influence on the subsequent star formation. The Jeans mass sets a typical value for a cloud to collapse gravitationally and fragment, depending on both temperature and density of the medium. Although the metal-enriched gas has a higher cooling efficiency than metal-poor gas, under the influence of a background radiation field the gas will stay hot and the Jeans mass will remain high. Therefore, the UV radiation background is a key parameter to take into account when studying the transition from Pop III to Pop II stars. In our simulations we see that including a constant radiation background raises the critical density value for this transition from $Z_{cr} \sim 10^{-3.5} Z_\odot$ to $Z_{cr} \sim 10^{-2} Z_\odot$ if $F_0 > 10^{-2}$ erg s^{-1} cm^{-2}.

Figure 3.6 – Density slices of the central 2 kpc of a halo at redshift z = 7.88 for a metallicity of $Z/Z_\odot = 10^{-3}$ with radiation fields of $G_0 = 10^{-2}$ (top left) and $G_0 = 10^{-1}$ (top right), and a metallicity of $Z/Z_\odot = 10^{-2}$ with radiation fields of $G_0 = 10^{-2}$ (bottom left) and $G_0 = 10^{-1}$ (bottom right) in the $x - z$ plane.
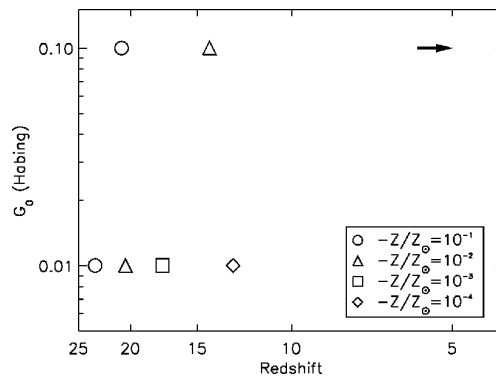

Figure 3.7 – Radiation field strength vs. redshift. Symbols mark the redshifts where a cold dense gas phase is established. The arrow represents the runs with $Z/Z_\odot = 10^{-3}$ and $Z/Z_\odot = 10^{-4}$, for a radiation field of $G_0 = 10^{-1}$, which do not develop a cold dense gas phase before z = 5.

3.3.3 Dynamics

When we look at the density slices of the Z1–G1 and Z2–G1 runs in Figure 3.3 in the $x - z$ plane we see an elliptical spiral structure and in the $x - y$ plane a flattened structure. This is a disk-like distribution in three dimensions and is more extended and massive in the Z1–G1 run ($M = 5 \times 10^9 \, M_\odot$) than in the Z2–G1 run ($M = 3.4 \times 10^9 M_\odot$). Because the gas cools faster in the halo of the Z1–G1 run, more gas is accreted and it settles faster into a disk than in the Z2–G1 run.

In Figure 3.8, which is a volume rendering plot, we show the three-dimensional density snapshots of the Z1–G1 (top), Z2–G1 (middle), and Z2–G10 (bottom) runs for redshifts z = 7.88 (left), z = 6.24 (middle), and z = 5 (right). We see that in the Z1–G1 run more structures are formed and generally they have higher densities than in the Z2–G1 and Z2–G10 runs. When we look at the middle and bottom plots we clearly see the effect of UV irradiation on the evolution of a halo. In the Z2–G10 run, structures are more fluffy and take more time to become dense and compact due to the heat input. In these plots fluffiness is represented by the spatial extent of the different colors. Although the halo in the Z1–G1 run experiences multiple and more violent mergers as well as a higher rate of gas accretion, due to the faster cooling the halo at redshift 5 is denser and more compact than the Z2–G1 case. In Figure 3.9, we plot the amount of mass for the densities indicated along the x-axis and for redshifts z = 7.88 (left), z = 6.24 (middle), and z = 5 (right). In these plots it is clearly seen that there is more mass at higher densities in the Z1–G1 run than the Z2–G1 run.

In Figure 3.10, we plot the fraction of the halo gas mass that has a Jeans mass (M_J) below a certain threshold value for the Z1–G1 (black–dashes) and Z2–G1 (red–dots) runs. The profile of the low-metallicity case starts with a much steeper rise at low Jeans mass thresholds but then levels off for higher Jeans mass thresholds more rapidly than the high metallicity case. This initial steep rise seems to be due to a lack of low Jeans masses ($< 30 \, M_J$) in the central 1 kpc halo of the Z2–G1 run. The fact that at any given threshold there is always a larger fraction of gas in the Z1–G1 run shows that the Jeans mass is generally lower in the high metallicity case than in the low-metallicity case.

As previously mentioned, Figure 3.3 shows a disk-like structure for metallicities $Z/Z_\odot = 10^{-2}$ and $Z/Z_\odot = 10^{-1}$. In order to see if this disk-like structure is stable we plot the time evolution of specific angular momentum (see Figure 3.11). In this plot we see that the specific angular momentum increases with time indicating that the disk-like structure becomes more rotationally supported. We also see several peaks which are caused by recent merger events.

Next, we plot the spin parameter evolution of our main halo for the Z4–G1 run (see Figure 3.12) . The spin parameter represents the degree of rotational support available in a gravitational system. We compute the dimensionless spin parameter (Peebles 1969) as

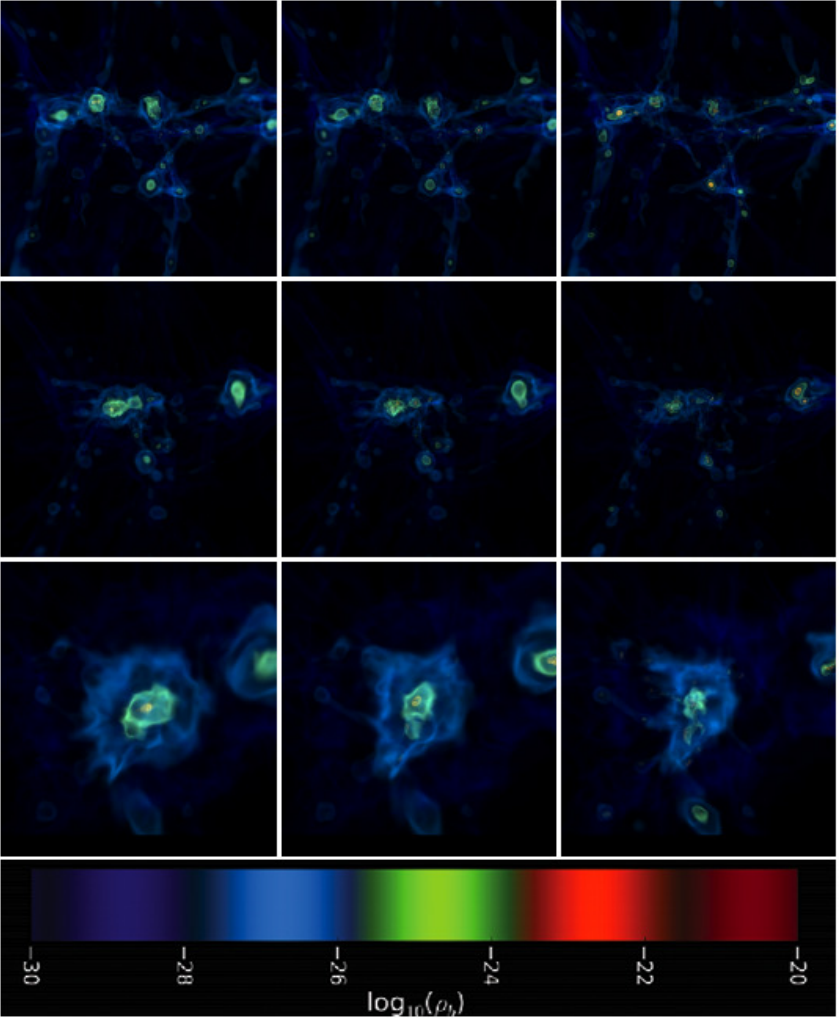$$\lambda \equiv \frac{|L| \sqrt{|E|}}{GM^{(5/2)}} \tag{3.8}$$

Figure 3.8 – Three-dimensional, volume rendered, density snapshots of the runs for metallicities of $Z/Z_\odot = 10^{-1}$ (top) and $Z/Z_\odot = 10^{-2}$ (middle) for a radiation field of $G_0 = 10^{-2}$ and $Z/Z_\odot = 10^{-2}$ (bottom) for a radiation field of $G_0 = 10^{-1}$ at redshifts $z = 7.88$ (left), $z = 6.24$ (middle), and $z = 5$ (right). Size of the box for redshifts 7.88 and 6.24 is 60 kpc, and for redshift 5 is 10 kpc.
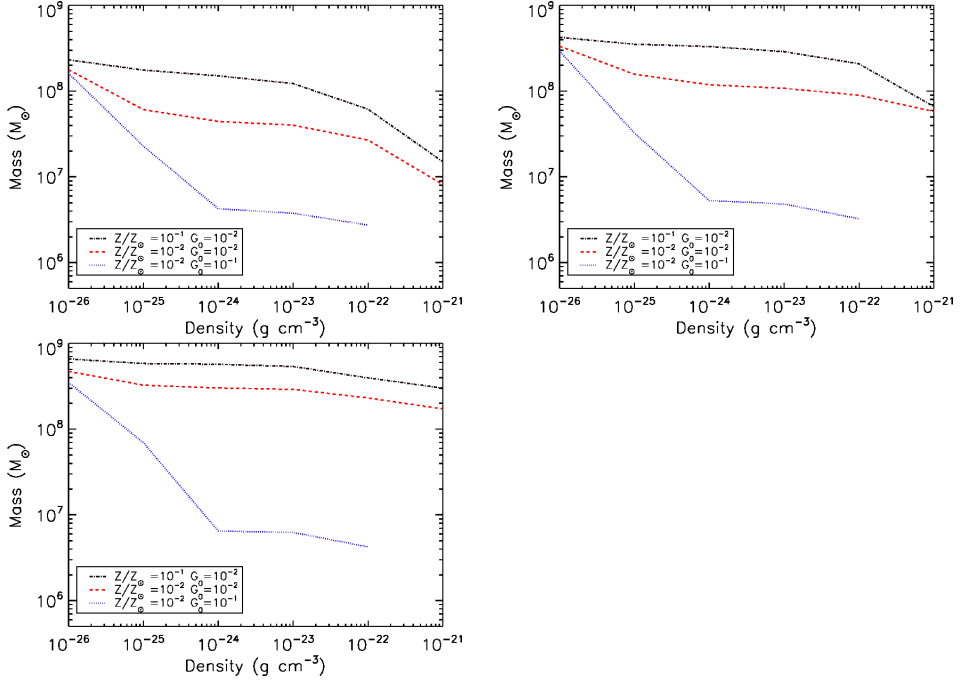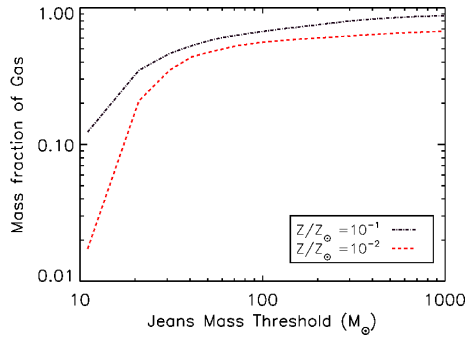
Figure 3.9 – Gas mass vs. density threshold of the central 10 kpc for metallicities of $Z/Z_\odot = 10^{-1}$ and $Z/Z_\odot = 10^{-2}$ for a radiation field of $G_0=10^{-2}$ and $Z/Z_\odot = 10^{-2}$ for a radiation field of $G_0 = 10^{-1}$ at redshifts z = 7.88 (top-left), z = 6.24 (top-right), and z = 5 (bottom).

Figure 3.10 – Gas mass fraction vs. Jeans mass threshold for metallicities of $Z/Z_\odot = 10^{-1}$ (black dots) and $Z/Z_\odot = 10^{-2}$ (red dashes) at redshift z = 5 for the central 1 kpc.
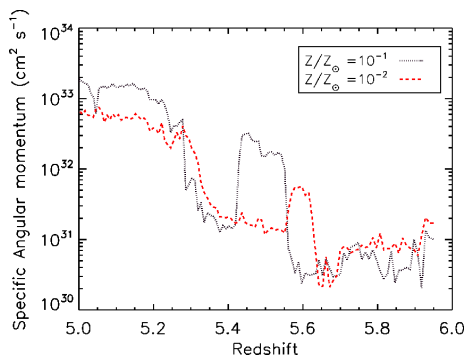
Figure 3.11 – Specific angular momentum vs. redshift for metallicities of $Z/Z_\odot = 10^{-1}$ (black
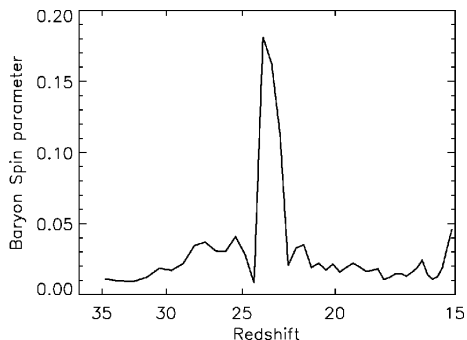dots) and $Z/Z_\odot = 10^{-2}$ (red dashes) for the central 1 kpc.

Figure 3.12 – Evolution of the spin parameter of the main halo for a metallicity of $Z/Z_\odot = 10^{-4}$.

where L is the angular momentum, E is the energy, M is the mass of the object,
and G is the gravitational constant. Barnes & Efstathiou (1987) have calculated
that the mean spin parameter is $< \lambda > = 0.05$ and it has been shown that halos
which have suffered a recent major merger tend to have a higher spin parameter
than the average (e.g., Hetznecker & Burkert (2006)). As is shown in Figure 3.12,
the spin parameter of our halo peaks around redshift z = 24, where a recent major
merger occurred, and overall it has a value of ≈ 0.04.

In Figure 3.13, we show the mass radial profiles of the Z1–G1 and Z2–G1
runs, top and bottom, respectively. In both runs, the inner parts of the halo are
dominated by baryonic matter. On the other hand, in the Z2–G1 run dark matter
takes over at a smaller radius (700 pc) than in the Z1–G1 run (950 pc). This is
because in the Z1–G1 run the halo is larger and more massive baryonically than
in the Z2–G1 run. Once more, this shows that the halo evolves dynamically slower
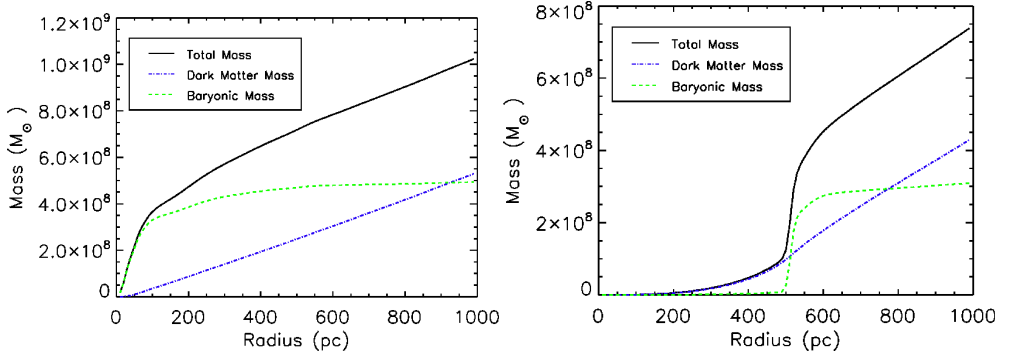in the low metallicity run.

Figure 3.13 – Mass vs. radius plots for metallicities of $Z/Z_\odot = 10^{-1}$ (left) and $Z/Z_\odot = 10^{-2}$ (right) for a radiation field of $G_0 = 10^{-2}$ at redshift z = 5. The lines represent the total (black solid), gas (green dashes), and dark matter (blue dot-dashes).

In Figure 3.14, we plot the mass-weighted rotational velocity (L/r) versus enclosed gas mass (top) and the ratio of rotational velocity to circular velocity versus enclosed gas mass (bottom) for the Z1–G1 and Z2–G1 runs. In both cases the typical rotational speed is 2 − 3 times lower than the circular velocity which means that the collapse of the halo is not delayed by rotational support (Wise et al. 2008).
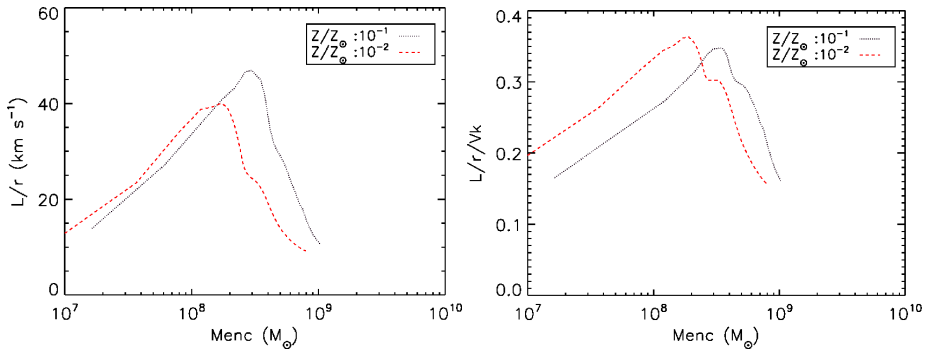

Figure 3.14 – Mass-weighted rotational velocity (L/r) vs. enclosed gas mass (left) and the ratio of the rotational velocity and circular velocity against enclosed gas mass (right) plots for metallicities of $Z/Z_\odot = 10^{-2}$ (red dashes) and $Z/Z_\odot = 10^{-1}$ (black dots) at redshift z = 5.

3.3.4 Star Formation and Feedback

When we include star formation and mechanical feedback in our simulations we see that, in the case of $Z/Z_\odot = 10^{-4}$ pre-enrichment, the halo is further enriched up to $Z/Z_\odot = 10^{-1}$ by the SNe of the first stars as early as $z \sim 18$. In Figure 3.15,
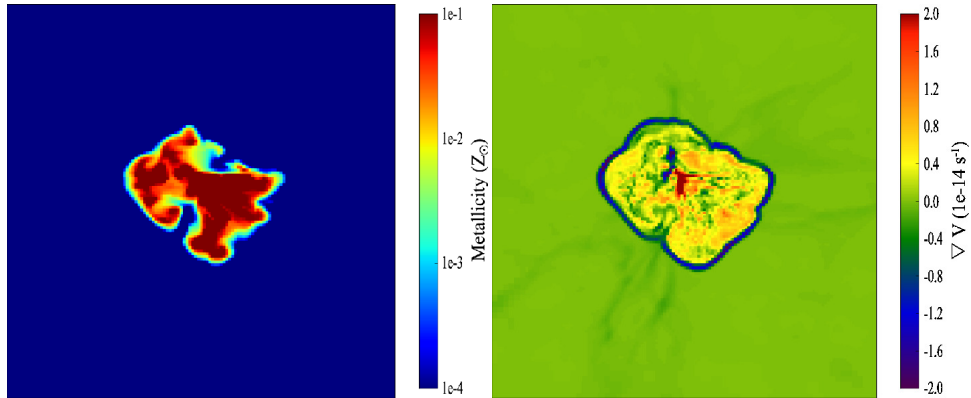
Figure 3.15 – Slices of metallicity fraction (left) and velocity divergence (right) of the central 10 kpc of a halo for $Z/Z_\odot = 10^{-4}$ at z = 18 in the $y - z$ plane.

we present the metal fraction (top) and the velocity divergence (bottom) of the central 10 kpc around the halo a short time after the first Pop III SN exploded. In the velocity divergence plot, we see a clear ring-like structure with a large velocity gradient. This is due to the multiple outflows driven by SNe that collide with inflowing material. Also, the highest outflow velocities are right behind the shock front as expected.

In Figure 3.16, where we plot time snapshots of temperature, density, and metallicity fraction of the central 25 kpc right after the first SNe, it is seen that the gas is heated to $\geq 10^4$ K and expelled from the halo and hence infall of the outer halo gas onto the central core of the halo is quenched. The distribution of metals, provided by SNe, is very patchy. In the center of the halo, there are regions present with high metallicities, $Z/Z_\odot = 0.1$, while in the outskirts of the halo the gas is still poor in metals. This indicates that SN feedback efficiently suppresses star formation in our enriched halos, irrespective of the ambient UV field.

On the other hand, after the first SNe go off we do not see any significant difference in the distribution of metals in the halo for the pre-enriched runs with $Z/Z_\odot = 10^{-4}$ and $Z/Z_\odot = 10^{-2}$, as shown in Figure 3.16. This indicates that the higher densities in the high-metallicity run do not have any effect on the mixing of metals in the halo. There might be a cooling instability effect on the mixing of the metals produced by the SNe with the surroundings that we are not taking into account, but since the SN feedback is strong we think that this effect is negligible.
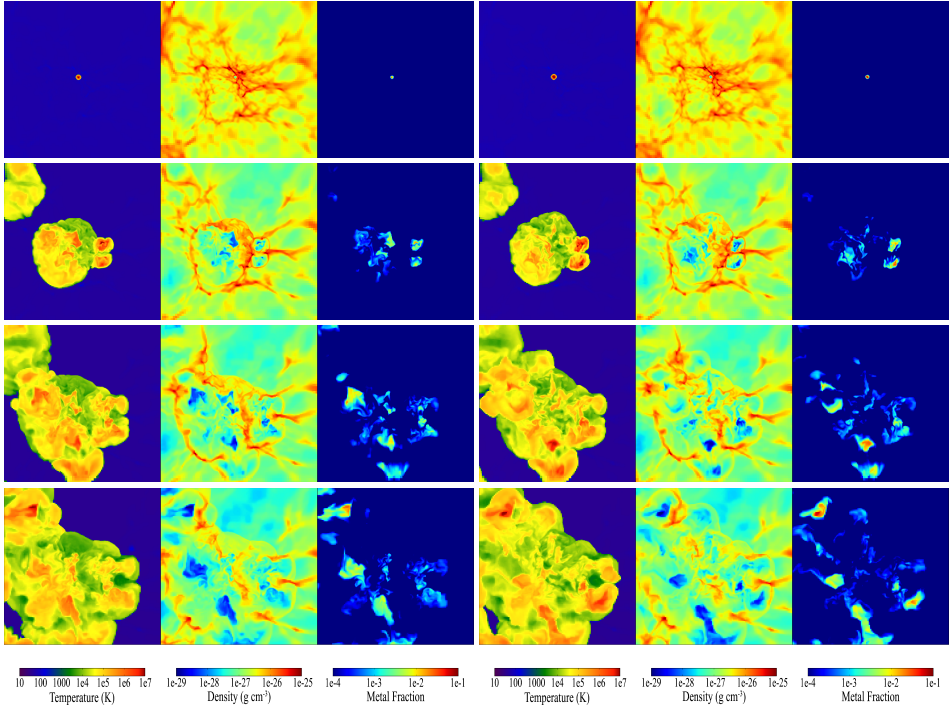
Figure 3.16 – From left to right: Slices of temperature, density, and metallicity fraction of the central 25 kpc for pre-enrichment metallicities of $Z/Z_\odot = 10^{-4}$ (left column) and $Z/Z_\odot = 10^{-2}$ (right column) for a radiation field of $G_0 = 10^{-2}$ at redshifts z = 18.7, 15, 13.4, and 12.3 (from top to bottom, respectively) in the $y - z$ plane.

3.4   Conclusions and Caveats

We summarize our results as follows.

1. The redshift at which a multi-phase ISM is established depends on metallicity. In the absence of UV radiation, this critical metallicity is consistent with Bromm & Loeb (2003b) and Smith & Sigurdsson (2007), and is $(Z/Z_\odot)_{crit} \sim 10^{-3.5}$.

2. Above a metallicity of 1% Solar the cooling efficiency of ambient gas no longer increases with a rise in metallicity (Spaans & Meijerink 2008), and therefore the Jeans masses in halos that are pre-enriched to metallicities of $Z/Z_\odot = 10^{-2}$ and $Z/Z_\odot = 10^{-1}$ are comparable.

3. The cold dense gas phase is fragile to UV radiation for metallicities of $Z/Z_\odot \leq 10^{-3}$ and robust to UV radiation for metallicities of $Z/Z_\odot \geq 10^{-2}$. Thus, the

metal-poor star-forming ISM is fragile to UV radiation, and inclusion of a constant radiation background raises the critical metallicity value for the Pop III–Pop II transition from $Z_{cr} \sim 10^{-3.5} Z_\odot$ to $Z_{cr} \sim 10^{-2} Z_\odot$ when $F_0 > 10^{-5}$ erg s^{-1} cm^{-2}, which is in good agreement with the values that are found for the suppression of H_2 by Shang et al. (2010). This is because H_2 is one of the main drivers of ion–molecule chemistry in metal-enriched gas and without it cooling is dominated by the fine-structure lines of [C II] and [O I] rather than CO.

4. All the indicators for the dynamical evolution show that the halo evolves dynamically faster for $Z/Z_\odot \geq 10^{-2}$ and that the cold and dense gas phase in high metallicity halos survives (violent) mergers due to the enhanced cooling.

5. Pre-enrichment does not affect mixing of the metals that are produced by the first SNe.

For future work, our simulations can be improved in several ways. We reach down to a maximum resolution of 75 and 7 pc with and without star formation feedback in our simulations, respectively. This is not enough to resolve the smallest gas fragments that will eventually turn into stars and to follow the collisional coupling between gas and dust. Our simulations also assume a constant ambient UV background field which might not be realistic because the UV radiation will originate from specific stellar sources. These sources are most likely to form in high-density areas and it would therefore be better to tie the UV background radiation to these sources at the time of their formation.

Another improvement can be made by adjusting the way we pre-enrich the simulations. Currently we assume one metallicity for a specific simulation. We do this so that we can confidently study specifically the metallicity effects on the evolution of our halo. However, the distribution of metals, that are formed by the first SNe, is not uniform but inhomogeneous. Therefore, in the near future we will perform simulations that consider patchy pre-enriched halos.

The Response of Metal Rich Gas to X-Ray Irradiation from a Massive Black Hole at High Redshift: Proof of Concept

"How far that little candle throws his beams!
So shines a good deed in a naughty world."
William Shakespeare, The Merchant of Venice, Act V, Scene i 89-90, 1596

A. Aykutalp, J. H. Wise, R. Meijerink, M. Spaans
Submitted to ApJ, 2012

Chapter 4 – The Response of Metal Rich Gas to X-Ray Irradiation from a Massive Black Hole at High Redshift: Proof of Concept

Abstract

Observational studies show that there is a strong link between the formation and evolution of galaxies and the growth of supermassive black holes (SMBH) at their centers. However, the underlying physics of this observed relation is poorly understood. Active galactic nuclei (AGN) in which interstellar material is still rapidly accreting onto SMBHs, are key to the study of this relation. Here, UV and X-ray radiation from the accretion disk influence the chemistry of the accreting and star-forming gas and affect the thermodynamics of the ISM. In order to study the effects of X-ray radiation on the surroundings of the black hole, we implement the XDR code of Meijerink & Spaans (2005) into Enzo and use the radiation transport module *Moray* to calculate the radiative transfer for a polychromatic spectrum. As a proof of concept, we investigate the effects of X-ray irradiation, produced by a central massive black hole (MBH) with a mass of $M = 5 \times 10^4$ $M_\odot$ at z = 15, on ambient gas with solar and zero metallicity. In this, we used XDR tables for solar metallicity and for a wide range of X-ray flux $F_X = 10^{-1.25} - 10^{5.5}$ erg cm^{-2} s^{-1}, density $n = 10 - 10^6$ cm^{-3} and column density $N_H = 10^{20} - 10^{24}$ cm^{-2} values. We find that in the solar metallicity case, due to high opacity of the metals, the energy deposition rate in the central region (< 20 pc) is much higher and hence the temperatures in the center are more than an order of magnitude higher (10^{5-6} K) than in the zero metallicity case. Moreover, due to the cooling ability and high intrinsic opacity of solar metallicity gas, column densities of 10^{24} cm^{-2} are reached at a radius of 20 pc from the BH. These column densities are about 3 orders of magnitudes higher than in the zero metallicity case. Furthermore, in the zero metallicity case an X-ray induced H ɪɪ region is formed already after 5.8 Myr. This causes a significant outflow of gas ($\sim 8 \times 10^6$ $M_\odot$) from the central region, with the gas reaching outflow velocities up to ~ 100 km s^{-1}. At later times, ~ 23 Myr after we insert the MBH, we find that the solar metallicity case also develops an X-ray induced H ɪɪ region, but delayed by ~ 17 Myr.

4.1 Introduction

Most galaxies today are thought to host supermassive black holes (SMBHs) in their centers (Kormendy & Richstone 1995, Richstone et al. 1998, Kormendy & Gebhardt 2001). Dynamical studies of central black holes in nearby galaxies reveal that there is a relation between the central black hole mass and the bulge mass ($M_{BH}/M_B \sim 10^{-3}$, Magorrian et al. (1998)) or the velocity dispersion ($M_{BH} \propto \sigma^p$, p $\sim$ 4, Ferrarese & Merritt (2000), Gebhardt et al. (2000)) of the stellar component of the host galaxy. More recent studies have shown that the value of p varies between $4 - 6$ depending on the type of the galaxy (Graham et al. 2011, McConnell et al. 2011). These relations suggest that there is a strong link between the formation and evolution of galaxies, and the growth of SMBHs at their centers.

The black hole masses of quasars observed at high redshifts ($z > 6$) are on the order of 10^9 $M_\odot$ (Fan et al. 2003, 2006a, Kurk et al. 2007). These SMBHs are thought to be formed (in less than 1 billion years) through the accretion of gas onto seed black holes of masses between 10^2 - 10^5 $M_\odot$. The origin of these seed black holes (Bromm & Loeb 2003a, Spaans & Silk 2006) is still an open question. However, the existence of quasars with inferred black hole masses in excess of 10^9 $M_\odot$ implies that black hole growth should be dominated by high accretion rates (≥ 0.1 Eddington) during their quasi-stellar object (QSO) phase.

The amount of gas available for the SMBHs to accrete depends on the mergers or interactions with galaxies, which drive large quantities of gas into galaxy centers (Barnes & Hernquist 1991), star formation and feedback processes. Observational (Merloni 2004) and theoretical (Hopkins et al. 2006) studies indicate that there is an evolution in the relation between the black hole mass and the host stellar mass such that at high redshifts ($z > 6$), the ratio between the black hole mass and the host stellar mass is on the order of $0.02 - 0.1$, which is more than one order of magnitude larger than the ratio measured in local galaxies (Murray et al. 2009).

The growth of SMBHs during a quasar phase can be traced by the luminosity function of QSOs as a function of redshift (Soltan 1982). The peak activity of luminous QSOs occurs at $z \sim 2 - 3$, where the majority of the most massive galaxies were also forming most of their stars. On the other hand, the peak activity of lower luminosity active galactic nuclei (AGN) occurs at $z \sim 0.7 - 1$. X-ray selected AGN serve as a population to robustly determine the luminosity function and evolution of unobscured AGN. However, the obscured fraction of AGN depends on X-ray luminosity as well as redshift. Therefore, this obscured fraction might affect the peak determination (Comastri & Brusa 2008). The average black hole mass increases with increasing redshift, meaning that there are fewer low-mass black holes at high redshifts, and the average accretion rate decreases towards lower redshift. This observed anti-hierarchical behavior of AGN evolution indicates that SMBHs and their host galaxies co-evolve.

The underlying physics of the observed relation between the formation and evolution of galaxies and their central SMBHs is still unknown. Several efforts

have been made to explain the origin of this relation by using semi-analytical modeling (Kauffmann & Haehnelt 2000, Wyithe & Loeb 2003) and N-body SPH simulations (Springel et al. 2005a,b, Di Matteo et al. 2005). Numerical simulations have shown that the gravitational tidal torques excited during major mergers lead to rapid inflows of gas into the centers of galaxies (Barnes & Hernquist 1991, 1996) which can be the mechanism to trigger quasar activity and starbursts in galaxies. Observations of low-redshift quasars show a connection between galaxy mergers and quasar activity (Heckman et al. 1984, Bahcall et al. 1996). In the local universe, ultraluminous infrared galaxies (ULIRGs) have bolometric luminosities similar to bright quasars and are often in mergers (Sanders et al. 1986, Sanders & Mirabel 1996), and there is observational evidence that ULIRGs form the birthplaces of QSOs (Sanders et al. 1988, van der Werf et al. 2011).

Di Matteo et al. (2005) argue that a merger generates a burst of star formation and leads to strong inflows that feed gas to the SMBH and thereby power the quasar. Hence, the energy released by the quasar expels enough gas to inhibit further star formation and quenches the growth of the black hole. Also, Hopkins & Quataert (2010) find that nuclear star formation is more tightly coupled to AGN activity than the global star formation rate of a galaxy.

AGN, in which interstellar material is still rapidly accreting onto SMBHs, are key to the study of the Magorrian relation. The accretion of gas onto the central black hole yields a luminous source of X-ray, UV, and optical photons. Here, UV and X-ray radiation influence the chemistry of the accreting and star-forming gas and affect the thermodynamics of the ISM. AGN are thought to be partially obscured by dusty interstellar matter (ISM). X-rays (1 – 100 keV) have smaller absorption cross sections than UV photons and, therefore, can penetrate large columns ($N > 10^{22}$ cm^{-2}). Hence, they provide a probe of the innermost regions of AGNs. Furthermore, the main heating mechanism in X-ray dominated regions (XDRs) is photoionization (Coulomb heating with thermal electrons), whereas in photon dominated regions (PDRs) it is photoelectric heating. Hence, the heating efficiency in XDRs and PDRs is $\sim$ 30% and 0.1 – 1%, respectively (Meijerink & Spaans 2005). Pérez-Beaupuits et al. (2011) have post-processed the 3-D hydrodynamical models of an AGN torus (Wada et al. 2009) by using the chemical network of Meijerink & Spaans (2005). They estimated the X-ray flux emanating from the black hole and found that X-ray irradiation affects the thermodynamics of the AGN torus up to 100 pc. They have calculated that the temperature of AGN gas, exposed to X-rays is a factor $\sim$ 5 higher than gas in a starburst of equal bolometric power. This has strong effects for star forming clouds, since the Jeans mass (M_J) scales with the temperature of the ambient gas as $M_J \propto T^{3/2}$. Therefore, this might inhibit star formation in the central galactic regions or change the initial mass function [IMF, Hocuk & Spaans (2010, 2011)]. Moreover, Wada et al. (2009) studied the molecular gas disks around AGN and have suggested that XDR physics may change the distribution of H_2 around an AGN. Recent work by Kim et al. (2011) focused on galaxy formation with feedback-regulated star formation and black hole growth. In their simulations they have taken into account the ra-

diative feedback from the central massive black hole (MBH) and found that radiative feedback from the MBH locally suppresses star formation and self-regulates its growth. However, they use a monochromatic spectrum for X-ray photons and have a limited chemical network. Here we define a SMBH M $>$ 10^6 M$_\odot$ and a MBH M = $10^2 - 10^6$ M$_\odot$.

In order to study the effects of X-ray irradiation from an accreting black hole in the central region of a galaxy, we perform 3-D cosmological hydrodynamic simulations with and without XDR physics, by implementing the XDR/PDR chemical network of Meijerink & Spaans (2005) into Enzo. This work is the first part of a trilogy where we investigate the effects of X-ray irradiation by an AGN on ambient gas. We will study the Magorrian relation and derive observational diagnostics to find the X-ray fingerprints in the high redshift universe in two subsequent papers. Here, for a proof of concept, we show that X-ray physics has been succesfully included into Enzo. We further show that treating radiative feedback from the central MBH with a self-consistent XDR/PDR network and a polychromatic energy distribution is crucial to assess the relation between AGN and their host galaxies. In this study, we concentrate on the effects of X-rays on the multi-phase ISM near the central black hole. This will help us to better understand the conditions of star formation near an AGN and hence the interplay between stellar feedback and radiative feedback from the central BH.

This paper is structured as follows. In Section 2 we detail our implementation of the XDR code into Enzo and the treatment of the polychromatic spectrum. We further discuss the relevant cooling and heating processes in XDRs. In Section 3 we describe the set-up of the simulations. In Section 4 we present the results and implications of our simulations. Finally, in Section 5 we discuss our results. We present some of the outputs of our chemical network in the Appendix.

4.2 XDR Implementation

4.2.1 Black Hole Radiation

We set up our intrinsic specific X-ray flux (F$_i$) to have a spectral shape of the form

$$F_i(E) = F_0 \left(\frac{E}{1\mathrm{keV}} \right)^{-\alpha} \exp(-E/E_c) \ \mathrm{erg} \ \mathrm{s}^{-1} \ \mathrm{cm}^{-2} \ \mathrm{eV}^{-1}, \qquad (4.1)$$

where F_0 is the constant that determines the total X-ray flux in the spectrum, E ($\geq$ 1 keV) is the energy, $\alpha = 0.9$ is the characteristic spectral index of the power law component of Seyfert 1 galaxies (Pounds et al. 1990, Madejski et al. 1995, Zdziarski et al. 1995), and E$_c$ = 100 ke V is the cut-off energy (Madejski et al. 1995). In order to determine F_0, one needs an independent estimate of the bolometric X-ray flux F$_X$. We estimate the central F$_X$ by assuming that only 10% of the total luminosity

(L_{bol}) is emitted in X-rays (Schleicher et al. 2010),

$$F_X = \int_{\geq 1\text{keV}} F_i(E)dE = 0.1 \times L_{bol}/4\pi r^2 = 0.1 F_{bol}, \qquad (4.2)$$

where r is distance from the central black hole. We assume that the MBH has a radiative efficiency of $\epsilon = 0.1$ and thus has a luminosity $L = \epsilon \times L_{edd} = 1.2 \times 10^{37}(\epsilon/0.1)M/M_\odot$ erg s^{-1} and accretes at

$$\dot{M} = \frac{L_{Edd}}{\epsilon c^2}. \qquad (4.3)$$

We set $M_{BH} = 5 \times 10^4$ M$_\odot$, which gives a bolometric flux $F_{bol} = 4 \times 10^3$ erg s^{-1} cm^{-2} at our finest resolution of 3.6 pc. The UV part of the AGN spectrum is produced by the usual multi-color (Shakura & Sunyaev 1973) accretion disk, with a viscosity parameter of $\alpha = 0.1$.

In our XDR models only X-rays with E $\geq$ 1 keV are considered. Therefore, we take the integral of equation 4.1 over this energy range and equate it to the estimated bolometric flux to find $F_0 \approx 0.8$ erg s^{-1} cm^{-2} eV^{-1}. Furthermore, with increasing distance from the AGN, the X-ray flux does not solely decrease by $1/r^2$ but also by attenuation along the line of sight. This attenuation is determined by the opacity, which is a function of energy and position

$$\tau(E, \mathbf{r}) = \sigma_{\text{pa}}(E)N_H(\mathbf{r}), \qquad (4.4)$$

where $\sigma_{pa}(E)$ is the photoelectric absorption cross section per hydrogen nucleus, and $N_H(\mathbf{r})$ is the total column density of hydrogen between the central black hole and the position $\mathbf{r}$. Taking this opacity effect into account we calculate the total X-ray flux for a given column density as

$$F_X = \int_{\geq 1\text{keV}} F_0\left(\frac{E}{1\text{keV}}\right)^{-\alpha} e^{-E/E_c} e^{-\tau(E,\mathbf{r})} dE \qquad (4.5)$$

4.2.2 Radiative Feedback

We use the Enzo radiation transport module *Moray* (Wise & Abel 2011a) to calculate the transfer of X-ray radiation field produced by the black hole. *Moray* solves the radiative transfer equation with ray tracing that is adaptive in spatial and angular coordinates. The ray normal directions are determined by HEALPix (Hierarchical Equal Area isoLatitude Pixelation; Górski et al. 2005). The rays originate from point sources and are progressively split when the angular sampling becomes too coarse, which can happen when the ray either propagates to larger radii or encounters a fine resolution AMR grid.

The rays are traced through the grid in a typical fashion (e.g., Abel et al. 1999), in which we calculate the next cell boundary crossing. In each ray segment crossing a single cell, we solve the radiative transfer equation for a ray,

$$\frac{1}{c}\frac{\partial P}{\partial t} + \frac{\partial P}{\partial r} = -\kappa P, \qquad (4.6)$$

where P is the monochromatic photon flux associated with the ray and $\kappa = \kappa(\mathbf{r}, t)$ is the absorption coefficient. In the static case, its solution has a simple exponential analytic solution and the photon flux of the ray is reduced by

$$dP = P \times (1 - e^{-\tau}), \tag{4.7}$$

where τ is the optical depth (see above) across the ray segment. Because *Moray* equates the photoionization rate to the absorption rate, it is photon conserving (Abel et al. 1999, Mellema et al. 2006). Thus, the photoionization and photoheating rates are, respectively,

$$k_{\mathrm{ph}} = \frac{dP}{n_{\mathrm{abs}} V_{\mathrm{cell}} dt_P} \tag{4.8}$$

and

$$\Gamma_{\mathrm{ph}} = k_{\mathrm{ph}}(E_{\mathrm{ph}} - E_i) \tag{4.9}$$

where V_{cell} is the cell volume, E_{ph} is the photon energy and E_i is the ionization energy of the absorbing material. In each cell, the resulting k_{ph} and Γ_{ph} values are the sum from all rays that cross that cell, which then are inputs into the chemistry rate equations and energy equation.

4.2.3 Treatment of a General Input Spectrum

In the original release of *Moray* (Wise & Abel 2011a), radiation is discretized into energy bins. Since then, a more general approach of Shapiro et al. (2004) and Mellema et al. (2006) has been implemented that can consider arbitrary (polychromatic) spectral shapes. In this method, the radiative transfer equation is numerically solved before the simulation, giving a relative intensity I_ν as a function of neutral hydrogen column density N_H. The relative ionizing photon flux

$$I_\nu(N_H) = \int_{\nu_{\mathrm{th}}}^\infty \frac{L_\nu \sigma_\nu \exp(-\sigma_\nu N_H)}{h\nu} \, d\nu \tag{4.10}$$

for H ɪ, He ɪ, and He ɪɪ is computed and stored for 300 column densities, equally log-spaced over the range $N_H = 10^{12-25} \mathrm{cm}^{-2}$. ν_{th} is the ionization energy threshold for each absorbing species. Also, the average photon energy

$$\langle E \rangle = \frac{\int_{\nu_{\mathrm{th}}}^\infty h\nu I_\nu(N_H) \, d\nu}{\int_{\nu_{\mathrm{th}}}^\infty I_\nu(N_H) \, d\nu} \tag{4.11}$$

is pre-calculated as a function of hydrogen column density N_H. The attenuation across each segment is thus $dP = I_\nu(N_H + dN_H) - I_\nu(N_H)$, which is determined by interpolating from pre-calculated tables. These values of dP and $\langle E \rangle$ are used in Equations (4.8) and (4.9), resulting in a solution that retains the full spectral shape until the source radiation is fully attentuated.

4.2.4 XDR Physics

The dominant parameter that drives the chemical and thermal structure of the gas in XDRs is the ratio of the X-ray energy deposition rate to gas density, H_X/n. This occurs because the molecular destruction and heating rates per unit volume due to X-ray induced ionizations are proportional to nH_X, whereas the molecular formation and cooling rates are generally proportional to n^2 times a rate coefficient (Maloney et al. 1996).

The main heating mechanism in XDRs is photoionization. The rate at which photoionizations happen depends on the cross-section, which is a function of the frequency of the radiation and the properties of the atom. The absorption cross section of X-rays roughly scales with energy as $\sim 1/E^3$, which allows X-rays to penetrate deep into interstellar clouds. A photon with an energy of 1 keV penetrates a hydrogen column of about 10^{22} cm^{-2} for solar metallicity.

UV radiation is absorbed by outer-shell electrons, whereas X-ray photons are absorbed by inner-shell electrons. When an electron from an inner shell (e.g., the K-shell) is ejected it leaves the atom behind in an excited state with an inner shell vacancy and more energy than is required to remove the least bound electron. The inner shell vacancy can be filled by an outer-shell electron (e.g., an L-shell electron). The excess energy then can be shed in one of two ways: by emitting photons (fluorescence) or by ejecting outer electrons, which is referred to as the Auger effect.

When inner-shell ionization is followed by Auger ionization, two high energy electrons are produced; the first from the primary ionization; with an energy equal to the photon energy minus the binding energy of the ejected electron, and the second from Auger ionization which has an energy equal to the difference in binding energies of electrons in the inner and outer shell minus the binding energy of the outer shell electron. This can be hundreds or thousands of eV. In an ionized gas, these suprathermal electrons undergo frequent elastic collisions with thermal electrons and their kinetic energy is converted into heat.

In a predominantly neutral gas, these suprathermal electrons can collisionally excite and/or ionize ions before interacting with free electrons. These secondary ionizations are more important for H, H_2 and He than the primary ionizations, which is a consequence of the large primary photo-electron energies (Meijerink & Spaans 2005). The importance of secondary ionization is determined by the ionization fraction $x = n(H^+)/n(H)$ since the probability that a fast electron will share its energy with a free electron, compared to its probability of striking an atom or molecule, is proportional to this fraction. The ratio of secondary to primary ionizations is ~ 26, depending on the chemical composition of the gas (Dalgarno et al. 1999). If the ionization fraction of the gas is $x > 0.9$, then most of the kinetic energy goes into heat through Coulomb interactions with the ambient thermal electrons. If $x < 0.9$, then approximately 40% of the primary photo-electron energy goes into secondary ionization and excitation (H I excitation, mainly Lyα) whether the gas is atomic (Shull & van Steenberg 1985) or molecular (Voit 1991).

The heating efficiency of a molecular gas is larger than that of a mostly neutral atomic gas. When H_2 is ionized by a fast electron and recombines dissociatively, about 10.9 eV of the ionization energy can go into kinetic energy. On the other hand, an H_2^+ ion can react on with a hydrogen molecule to produce H_3^+, which may then either recombine dissociatively or react with other species. Due to the strong exothermic nature of the recombination reaction, Glassgold & Langer (1973) argue that for every H_3^+ ion formed about 8 eV goes into gas heating.

In general, ro-vibrational H_2 cooling is important in XDRs due to the high gas temperatures ($T_g > 1000$ K). The ro-vibrational bands of molecular hydrogen can be excited by the nonthermal electrons produced through X-ray ionization and thermal collisions with e^-, H and H_2. Collisional de-excitation of vibrationally excited H_2 can be an important heating source when non-thermal electrons dominate the excitation (at low H_X/n). These excited H_2 molecules can also enhance chemical reactions with an activation barrier (Meijerink & Spaans 2005).

XDRs are exposed to X-rays as well as FUV photons. Internally generated FUV photons are produced when energetic nonthermal electrons collide with atomic and molecular hydrogen. These collisions result in the emission of Lyα and Lyman-Werner band photons, and significantly affect the chemistry of the X-ray irradiated gas clouds. If the electron fraction of the gas is x $\leq$ 0.01, then about 40% of the energy deposited by X-rays results in the production of these internal FUV photons. Thus, the dense interiors of X-ray irradiated clouds can chemically resemble photodissociation regions with significant abundances of neutral oxygen as well as singly ionized iron, silicon and carbon (Maloney et al. 1996).

Most of the FUV photons that are locally produced by the nonthermal electrons will be absorbed by dust grains. The resulting temperature of the dust grains is proportional to the locally absorbed X-ray energy per hydrogen atom (H_X). Therefore, if the dust abundance is high, then there is less energy per dust particle and the average dust temperature T_d drops and is given by

$$T_d = 1.5 \times 10^4 (H_X/x_d)^{0.2} \text{ K,} \tag{4.12}$$

where $x_d = 1.9 \times 10^{-8}$ is the grain abundance (for solar metallicity) and H_X is in erg s^{-1} (Yan 1997). The minimum grain size is set to $a_{min} = 10$Å. In XDRs, the dust temperature for the same impinging flux by energy is lower than in PDRs (Meijerink & Spaans 2005). Also, in XDRs the gas heating efficiency is $10 - 50\%$ whereas it is $0.1 - 1\%$ in PDRs. Furthermore, the chemistry in XDRs is less stratified, with C^+, C, CO co-existing over large columns, than in PDRs.

At high temperatures (T > 5000 K) the gas cooling is dominated by collisional excitation of Lyα, and forbidden and semi-forbidden transitions of [O I] ($\lambda\lambda$ 6300, 6363 μm), [C I] ($\lambda\lambda$ 9823, 9850 μm), [Fe II]($\lambda\lambda$ 1.26, 1.64 μm), and [Si II] ($\lambda\lambda$ 6716, 6731μm).

The cooling below a few 1000 K is dominated by the fine-structure lines of [OI] 63 μm, [SiII] 35 μm, [CII] 158 μm, [CI] 269 and 609 μm. Rotational and vibrational transitions of H_2, H_2O, and CO may also be important when these molecules are

abundant. Cooling lines may become optically thick and such column density dependent transfer effects are included using a non-local escape probability method (Poelman & Spaans 2005). At high densities, and if the grain temperature is less than the gas temperature, gas-grain collisions can be a source of gas cooling and grain heating. For further details, we refer the interested reader to Meijerink & Spaans (2005).

4.2.5   Modifications to the 2005 XDR Code

The XDR code as described in Meijerink & Spaans (2005) has been modified by including all the heavy elements up to iron with abundances $> 10^{-6}$. As a result, the elements treated in the chemistry of the code were extended with Ne, Na, Ar and K. In the original XDR code, the doubly ionized states of C, N, O, S, and Fe were included. Here, we treat the singly and doubly ionized states of all elements, also He^{2+}. Most of the additional reactions were adopted from Ádámkovics et al. (2011), who give an elaborate description on the X-ray ionization of heavy elements. We followed their method to determine the secondary ionization rates of He^{2+}, which were scaled to those for hydrogen, by using the peak electron impact cross sections as obtained from Tarawa & Kato (1987). The primary ionization rates were obtained from Verner & Yakovlev (1995), where we assumed that no Auger ionization is possible, implying that only one electron is released per absorbed X-ray photon.

4.3   Simulations

In this work, we use the cosmological adaptive mesh refinement (AMR) code Enzo-2.0 [1] (Bryan & Norman 1997; O'Shea et al. 2004) that is modified to include XDR physics. We perform simulations in a three-dimensional periodic box with a side length of 3 h^{-1} Mpc, initialized at $z = 99$. The size of the root grid is 128^3 with three nested subgrids, each refined by a factor of two. The finest grid has an effective resolution of 1024^3 with a side length of 375 h^{-1} kpc. Refinement is restricted to the finest grid and occurs during the simulations whenever the baryonic matter, or dark matter density, is greater than the mean density by a factor of four. The maximum level of refinement that is reached in the finest grid is 10, allowing us to have a resolution of 3.6 pc. We use Wilkinson Microwave Anisotropy Probe seven-year cosmological parameters (Komatsu et al. 2009), which have the following values: $\Omega_\Lambda = 0.734$, $\Omega_m = 0.266$, $\Omega_b = 0.0449$, $\sigma_8 = 0.81$, and $h = 0.701$. Here, Ω_Λ is the vacuum energy, Ω_m is the matter density, Ω_b is the baryon density, σ_8 is the variance of random mass fluctuations in a sphere of radius 8 h^{-1} Mpc, and h is the Hubble parameter in units of 100 km s^{-1} Mpc^{-1}.

In order to see the impact of X-ray radiation from the central MBH on the surrounding gas, we have performed two simulations. In these simulations we use

---

[1] http://enzo-project.org

the primordial chemical network of Enzo until z = 15, where the most massive halo with a mass of 2×10^8 M$_\odot$ forms. At z = 15, we insert a MBH with a mass of 5×10^4 M$_\odot$, in order to be roughly consistent with the Magorrian relation, and consider its radiative feedback afterwards. In one of the runs, we start using the XDR tables compiled for solar metallicity gas (hereafter referred to XDR$_S$), and in the other one, we keep using the primordial chemical network of Enzo (hereafter referred to XDR$_Z$).

Our XDR chemical network consists of more than 170 species. We have constructed tables of XDR solutions for species abundances and temperatures for solar metallicity and for a wide range of X-ray flux F$_X$ = $10^{-1.25}$ – $10^{5.5}$ erg cm^{-2} s^{-1}, density n = $10 - 10^6$ cm^{-3} and column density N$_H$ = 10^{20} – 10^{24} cm^{-2}. This large parameter space enables us to model the ISM properties close to an AGN properly. We use Enzo's 9 species (H, H$^+$, H$^-$, He, He$^+$, He^{2+}, H$_2$, H$_2^-$, and e$^-$) non-equilibrium chemical network for zero metallicity gas. In the XDR$_S$ case, we run both the XDR routine and the chemical network of Enzo and compare the computed temperatures to determine if the cell is X-ray dominated. We take the highest value of the two found temperatures and continue to iterate for the next step. By doing this we naturally determine the maximal effect that X-rays have on exposed gas. This way, our proof of concept runs do not require any ad hoc metallicity distribution. In a follow-up paper we will include metal production by supernova explosions.

We choose solar metallicity for our XDR tables since this is a good approximation for regions around SMBHs, even inside $z \sim 6$ AGNs (Jiang et al. 2007). Moreover, attenuation of X-ray photons in a non-zero metallicity ISM has never been done before for a high redshift accreting MBH, and here we show that we can treat the impact of X-rays on such non-zero metallicity ambient gas. By choosing solar metallicity, we seek to highlight the full range of effects that metals introduce in X-ray exposed gas.

Furthermore, in our tables, we also store the abundances of all species that Enzo's chemical network is using, attached to the corresponding temperature values. For a given unattenuated flux, we create a table of attenuated fluxes as a function of column density. Combined we thus have an XDR grid of models in n, F$_X$, and N$_H$ (varying metallicity will be presented in paper II) that uses *Moray* to compute the full (chemical, thermal and hydrodynamic) response of X-ray exposed gas at non-zero metallicity. In the code, we calculate the column densities between the cell and MBH and incident flux with *Moray*, take the corresponding flux values from the pre-calculated tables and apply the radial dependence. By using the flux, density, and column density computed in Enzo, we find the corresponding temperature values and the species abundances from the pre-computed XDR grid tables for each cell and feed these back into Enzo. We stop the simulations after $\sim$ 40 Myr at z = 13.5. This is long enough for ambient gas in a radius of a few hundred pc to be affected by X-rays emanating from the 5×10^4 M$_\odot$ MBH and to find (if at all) an equilibrium again.

For the analysis of our cosmological simulations we use *yt*, a cross-platform
analysis toolkit written in Python (Turk et al. 2011b).

4.4   Results & Implications

In the simulations that we perform, as a proof of concept, we see significant differ-
ences between the solar metallicity and zero metallicity cases. Below we explain
the physical processes that play a role in causing the differences in the ISM prop-
erties of the modeled halos.

Shortly after we insert a MBH, we already note considerable differences be-
tween the two runs in the central region around the MBH. In Figure 4.1, we plot
the density-temperature histograms, within a sphere of 200 pc diameter, for the
XDR_S (left column) and XDR_Z (right column) runs at redshifts z = 14.95, 14.78,
14.54 and 13.54 from top to bottom. At z = 14.78, phase diagrams show that there
is less gas present in the XDR_Z case than in the XDR_S case. This difference in the
gas mass, in the inner 200 pc, becomes even more pronounced at redshift z = 14.54.
To estimate the amount of gas that is missing in the zero metallicity case we com-
pare the enclosed gas mass (see Figure 4.2) of both simulations as a function of
radius at redshift z = 14.78 (left) and z = 14.54 (right). We calculate the difference
in enclosed gas mass (blue dot-dashed line in Figure 4.2) in the inner 200 pc to be
8×10^6 $M_\odot$ between the XDR_S and XDR_Z cases, at z = 14.78. Furthermore, when
we look at the 2D density and temperature radial profiles (see Figures 4.3 and 4.4)
of the XDR_S and XDR_Z cases we see significant differences in the inner 20 pc while
at larger radius (R > 500 pc) the differences become less pronounced (see section
4.4.2).

The missing mass in the inner 200 pc of the XDR_Z run can be explained as
follows. In the XDR_S case because of the metals, X-rays see a high opacity, about a
factor of 3 − 30 higher than for zero metallicity gas. Because metals like C, N, O, Si,
and Fe have such large cross sections, for inner shell absorptions (see Figure 5.3 in
Meijerink (2006) for E > 1 keV and Morrison & McCammon (1983)), they lead to
an "opacity wall", if column densities exceed 10^{22} cm^{-2}. Thus, the energy deposi-
tion rate into the medium close to MBH is high and the X-ray power is dissipated
locally. On top of that, the cooling ability of solar metallicity gas is high. There-
fore, the cooling time is short beyond the opacity wall. Combined, large column
densities of 10^{24} cm^{-2} are reached in the central region as metal enriched gas falls
in and builds up sufficient column to shield itself from irradiation. However, in
the XDR_Z case, in the absence of metals, the X-rays penetrate to larger columns.
Thus, the energy deposition rate into the medium close to the MBH is significantly
less and X-ray power is dissipated globally. Moreover, the maximum column den-
sity is 4 orders of magnitude less than in the XDR_S case. This difference in column
densities is shown in Figure 4.5, where we plot the 2D column density-radius pro-
files for both cases at redshift z = 14.95 and 14.54. In this plot it is easily seen that
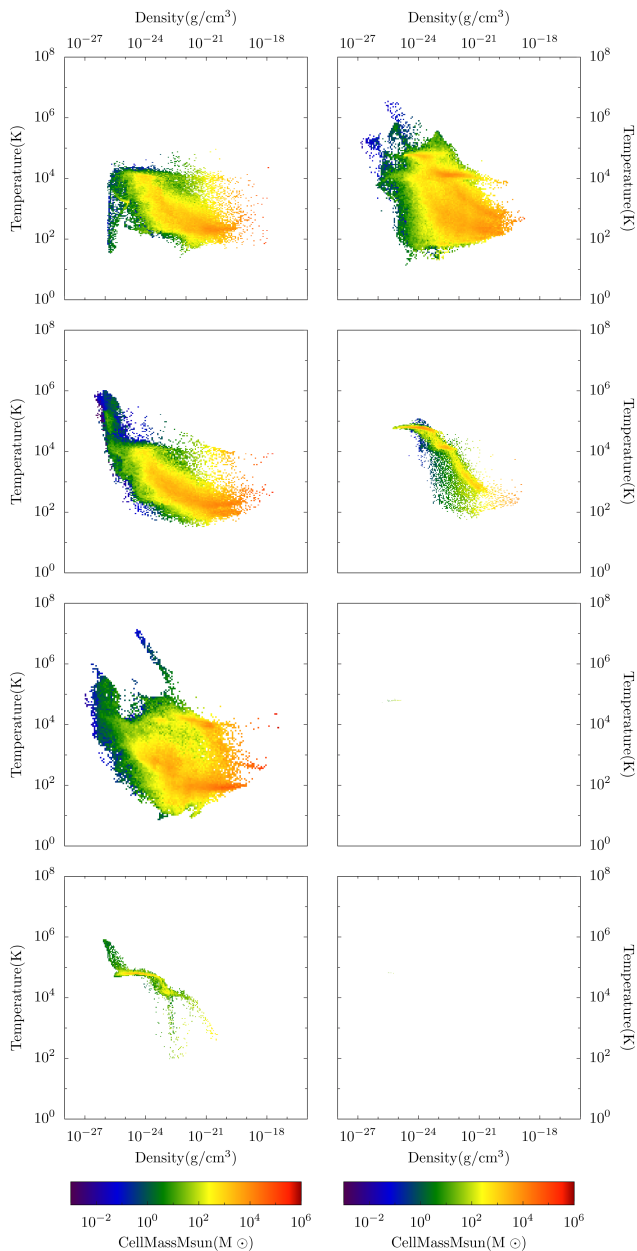the gas column, viewed from the MBH, builds up much faster in the XDR_S case

Figure 4.1 – Density-temperature phase diagrams within a sphere of 200 pc diameter for the XDR$_S$ (left) and XDR$_Z$ (right) cases at z = 14.95, 14.78, 14.54 and 13.54, from top to bottom. Note the missing mass already at z = 14.54 in the XDR$_Z$ case.
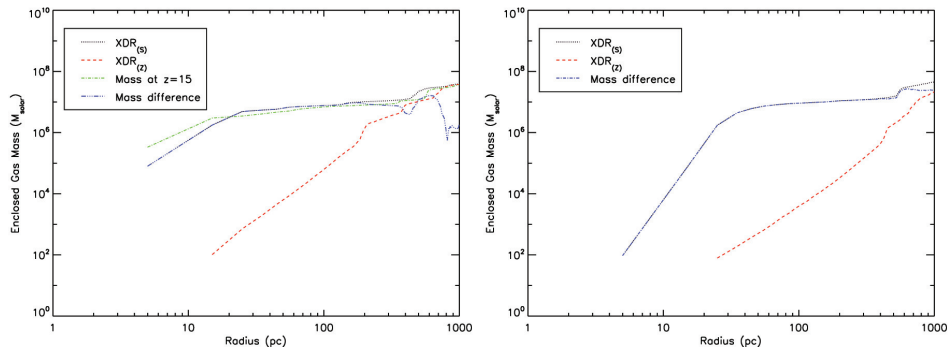
Figure 4.2 – Enclosed gas mass of the XDR$_S$ (black dotted line) run, the XDR$_Z$ (red dashed line) run, and the gas mass difference between the two runs (blue dotted dashed line) at z = 14.78 (left) and 14.54 (right) as a function of radius. The green dotted-dashed line in the left plot is the enclosed gas mass of the halo at z = 15.

due to the efficient accumulation of solar metallicity gas. Therefore, in the XDR$_Z$ case, the impinging X-ray flux onto the relatively low density gas that sits at larger radii is much higher. Hence, this forms an X-ray induced H II region.

The H II ionization front will sweep through the surrounding medium until the recombination rate inside the H II region balances the energy output of the MBH (see Figure 4.6 for the H I ionization fraction). As a consequence, in an attempt to establish pressure balance, the newly formed H II region will expand, thus driving large quantities of gas to larger radii. This also further lowers the column densities at small radii in the XDR$_Z$ case. A back of the envelope calculation, where we compare the gas kinetic energy to the energy in X-rays, shows that the energy input from the black hole ($L_{Edd} \sim 10^{42}$ erg s^{-1}) is sufficient to drive $\sim 10^7$ M$_\odot$ gas out with an average speed of ~ 100 km s^{-1} in 6.5 Myr.

4.4.1 Dynamics of the H II Regions

In Figure 4.7, we show the velocity field at z = 14.78 (top) and 14.54 (bottom) for the XDR$_S$ (left) and XDR$_Z$ (right) runs. Indeed, we see that in the XDR$_Z$ run there is an outflow, at a speed of ~ 100 km s^{-1}, which is caused by the X-ray induced H II region. However, in the XDR$_S$ case, due to the opacity wall, the X-rays are strongly attenuated. This leaves the gas at larger radii virtually unaffected. Due to the lack of a large scale H II region in the XDR$_S$ run, the bulk of the gas keeps falling towards the MBH, increasing the densities around the black hole. One thing to keep in mind here is that our smallest cell size is 3.6 pc, which means that we might be overestimating the metals' opacity effect and hence the energy deposition rate. It is possible that higher resolution simulations will show the formation of an H II region in the XDR$_S$ case as well, although at a much smaller
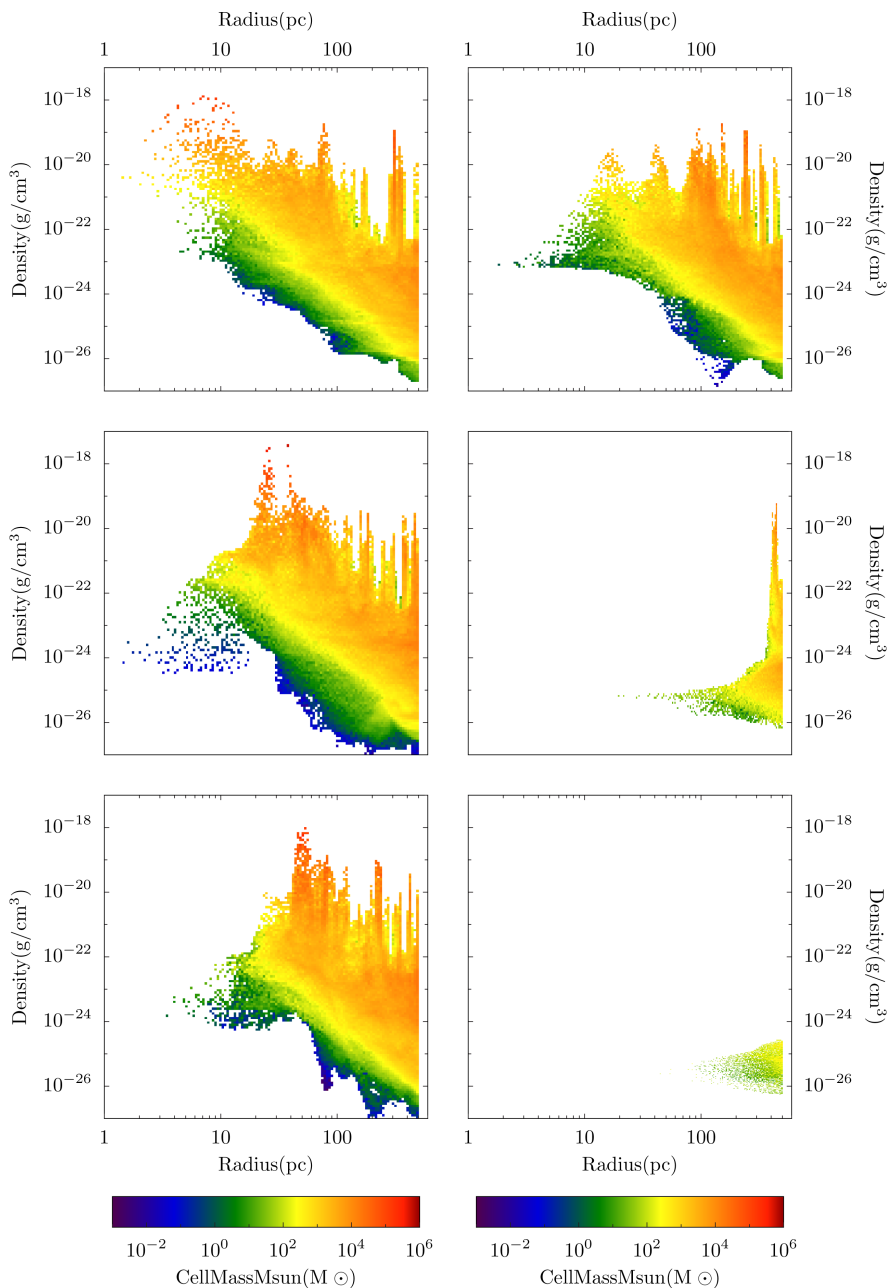
Figure 4.3 – 2D profiles of density versus radius for the XDR$_S$ (left) and XDR$_Z$ (right) at z = 14.95, 14.54, and 14.17, top middle bottom, respectively.
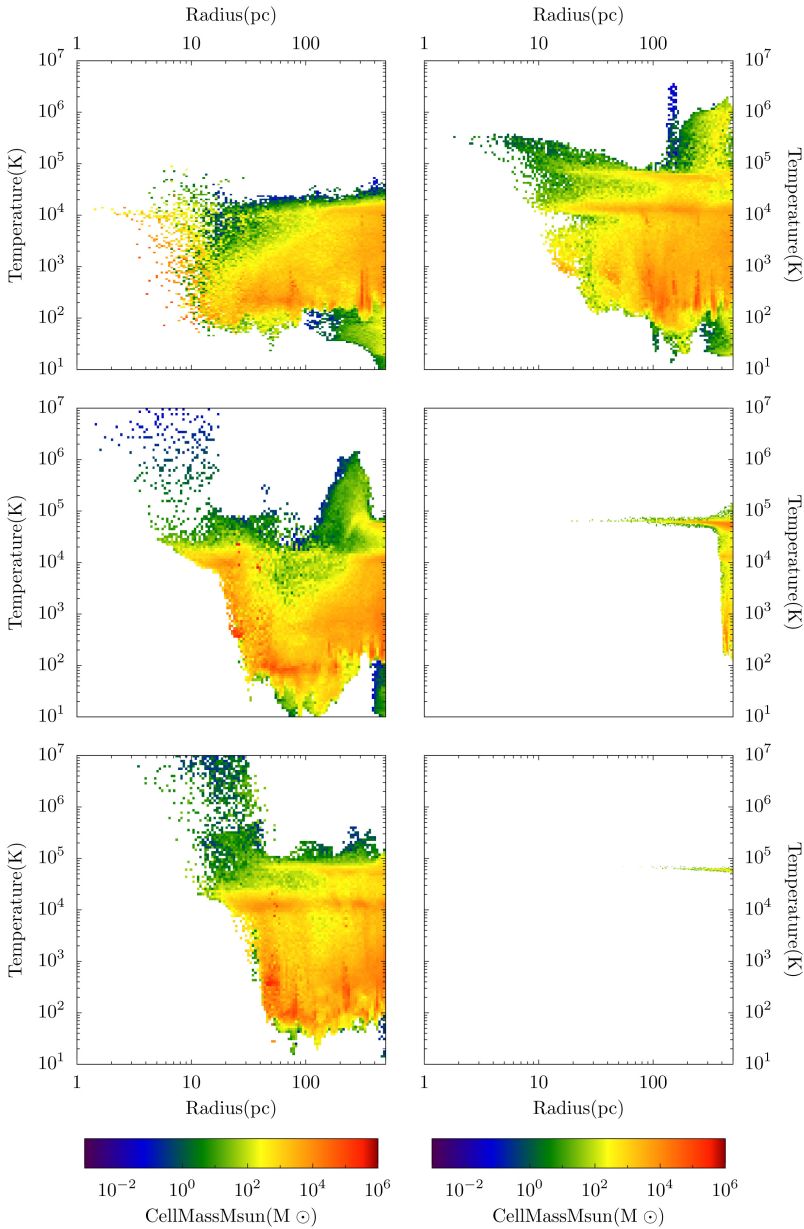
75

Figure 4.4 – 2D profiles of temperature versus radius for the XDR$_S$ (left) and XDR$_Z$ (right) at z = 14.95, 14.54, and 14.17, top middle bottom, respectively.
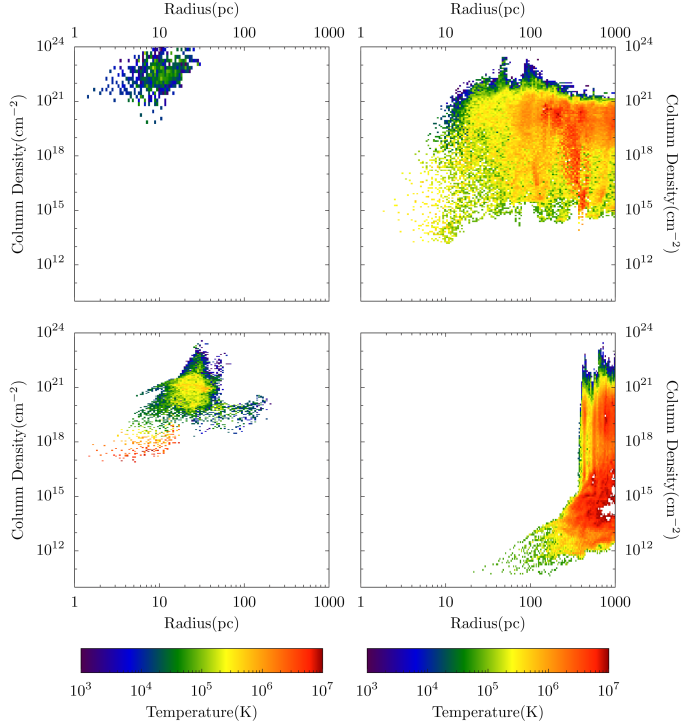
Figure 4.5 – 2D profiles of column density versus radius for the XDR$_S$ (left) and XDR$_Z$ (right) runs at z = 14.95 (top) and z = 14.54 (bottom).

spatial scale than in the XDR$_Z$ run. In fact, at z = 14.17, we see that X-rays start to penetrate much further (> 10 pc) in the XDR$_S$ case as well and drive an H II region, with a delay of 17 Myr, which pushes apart the central opacity wall with a speed of ∼ 200 km s^{-1}. This is shown in Figure 4.8 where we plot the X-ray flux, column density, velocity magnitude and the divergence of velocity slices along the x-axis for the XDR$_S$ run. The H II region forms at z = 14.17 (middle plots) and expands to a few kpc at z = 13.5 (bottom plots).

To understand this delay, two effects are relevant. First, in the XDR$_Z$ case, the initial H II region radius is larger because of the lower X-ray optical depth through zero metallicity gas. Consequently, in the XDR$_S$ case, the initial growth of the H II region is stiffened compared to the XDR$_Z$ case. Second, for a local ionizing photon rate S_i, the Strömgren radius scales as $R_S \propto (S_i/n^2)^{1/3}$, the recombination time as $t_s \propto 1/n$, and the ionization front velocity as $V_I \propto S_i/nR^2$. Because X-rays are absorbed in denser gas and at smaller radii in the XDR$_S$ run, the H II region grows more slowly when compared to the XDR$_Z$ case.
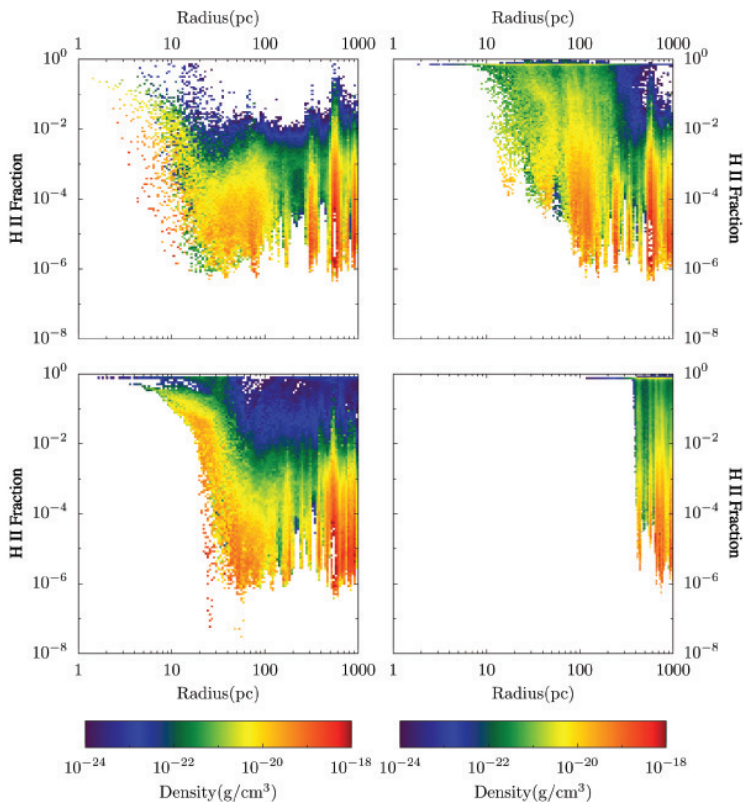
Figure 4.6 – 2D profiles of H I ionization fraction versus radius for the XDR$_S$ (left) and XDR$_Z$ (right) runs at z = 14.95 and 14.54.

4.4.2 Thermodynamics

At small radius (R ~ 20 pc), as a consequence of high metal opacity, the attenuated X-rays heat up the gas in the XDR$_S$ case as shown in Figure 4.4. Therefore, the temperature in the inner 20 pc in the XDR$_S$ case is more than an order of magnitude higher than in the XDR$_Z$ case at $z = 14.54$. Moreover, at $z = 14.17$, so after 17 Myr, the gas temperature in the central 10 pc increases from 10^5 to almost ~ 10^7 K in the XDR$_S$ case and the difference between the gas temperatures between the two runs becomes ~ 3 orders of magnitude (see Figure 4.4).

At large radius (R > 500 pc), we do not see much difference in the multiphase ISM of the XDR$_S$ and XDR$_Z$ runs. This is shown in Figure 4.9 where we plot the density-temperature phase diagrams within a sphere of 1 kpc radius for the XDR$_S$ (left column) and XDR$_Z$ (right column) runs at redshifts z = 14.95, 14.78, 14.54 and 13.54, from top to bottom. In a gas with modest ionization degree and weak X-ray radiation field the H$^-$ route will drive the formation of H$_2$ and HD, due to
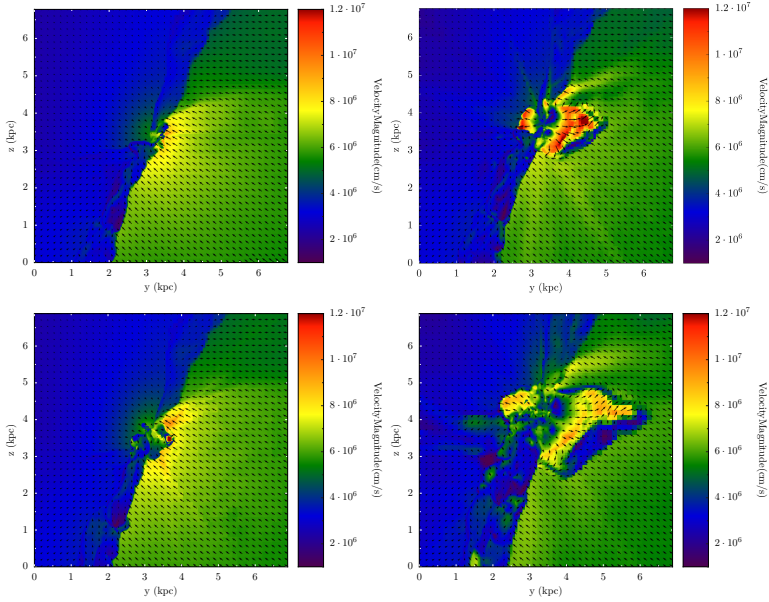
Figure 4.7 – Velocity magnitude slice along the x-axis overlaid with velocity vectors for the XDR$_S$ (left) and XDR$_Z$ (right) runs at z = 14.78 (top) and 14.54 (bottom).

the availability of free electrons. The presence of dust will boost the formation of H$_2$ (Cazaux & Spaans 2009). However, an increase in H$_2$ abundance will also increase the H$_2$ ionization rate, and hence the gas heating rate, when X-rays are present. In our simulations, most of the gas has temperatures of a few thousand K, and at those thermally unstable temperatures H$_2$ is the dominant cooling and heating channel. Therefore, we do not see a fundamental difference between the two runs.

In the XDR$_S$ run we see that at redshifts z = 14.78, as well as slightly later z = 14.54, high density gas (> 10^{-20} g cm^{-3}) is more abundantly present at temperatures of $\geq$ 500 K. There are two effects that play a role here. First of all, in the XDR$_S$, run the opacity is large enough to absorb any X-ray photon below 5–10 keV. Also, we reach column densities of 10^{24} cm^{-2} at small distances from the BH, as shown in Figure 4.5. This explains the lower HI ionization rates in the XDR$_S$ case as shown in Figure 4.6. Along these large columns, the X-ray flux is almost completely absorbed by the gas and thus the gas at larger distances is not much affected. Secondly, as mentioned before, solar metallicity gas can cool down and evolve to higher densities faster than zero metallicity gas, which was also found in the PDR studies of Aykutalp & Spaans (2011). During the fast collapse, adiabatic heating raises the temperature of the gas in the XDR$_S$ case as $\propto n^{3/2}$ while for X-ray heating this goes as $\propto n$. However, in the XDR$_Z$ run the maximum column
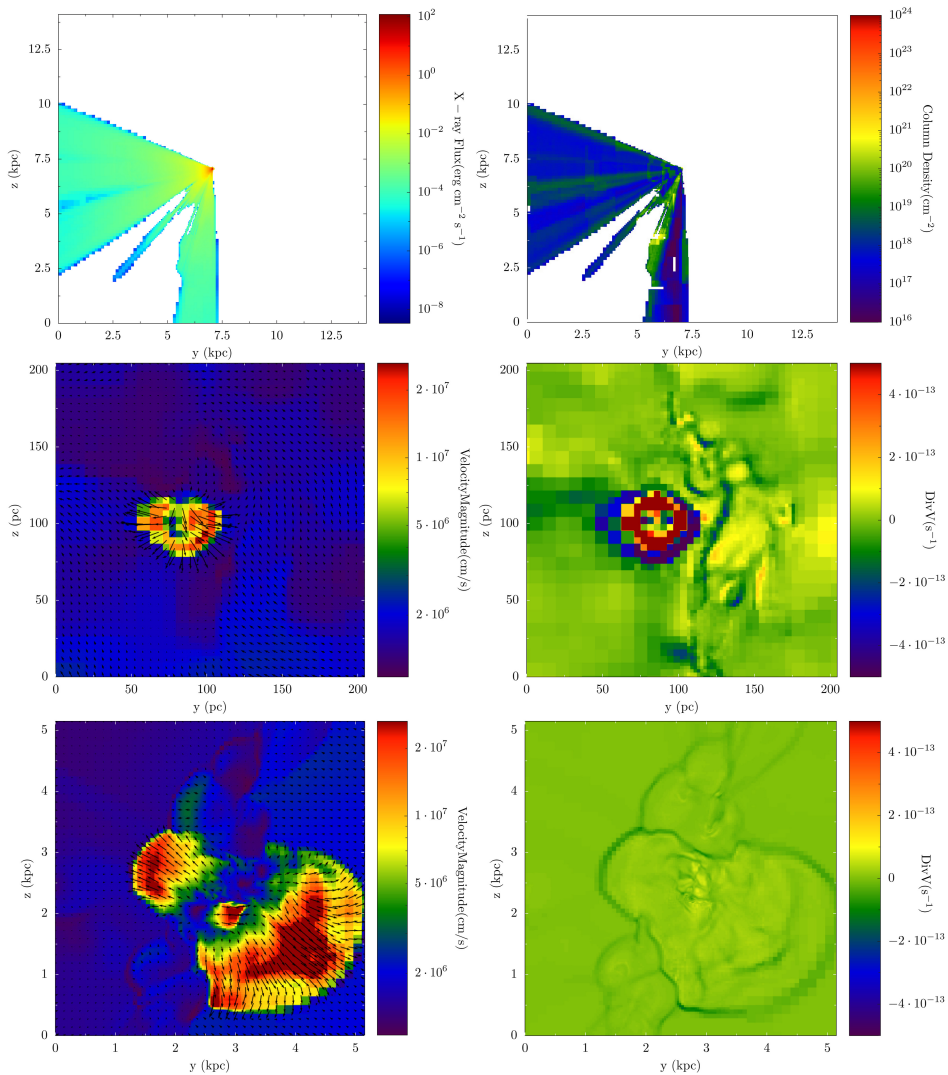
Figure 4.8 – X-ray flux (top-left) and column density (top-right) at z = 14.17. Velocity magnitude (left) and divergence of velocity (right) slices along the x-axis for the XDR$_S$ run at z = 14.17 (middle), 13.54 (bottom). The velocity plot is overlaid with velocity vectors in order to show the outflow.
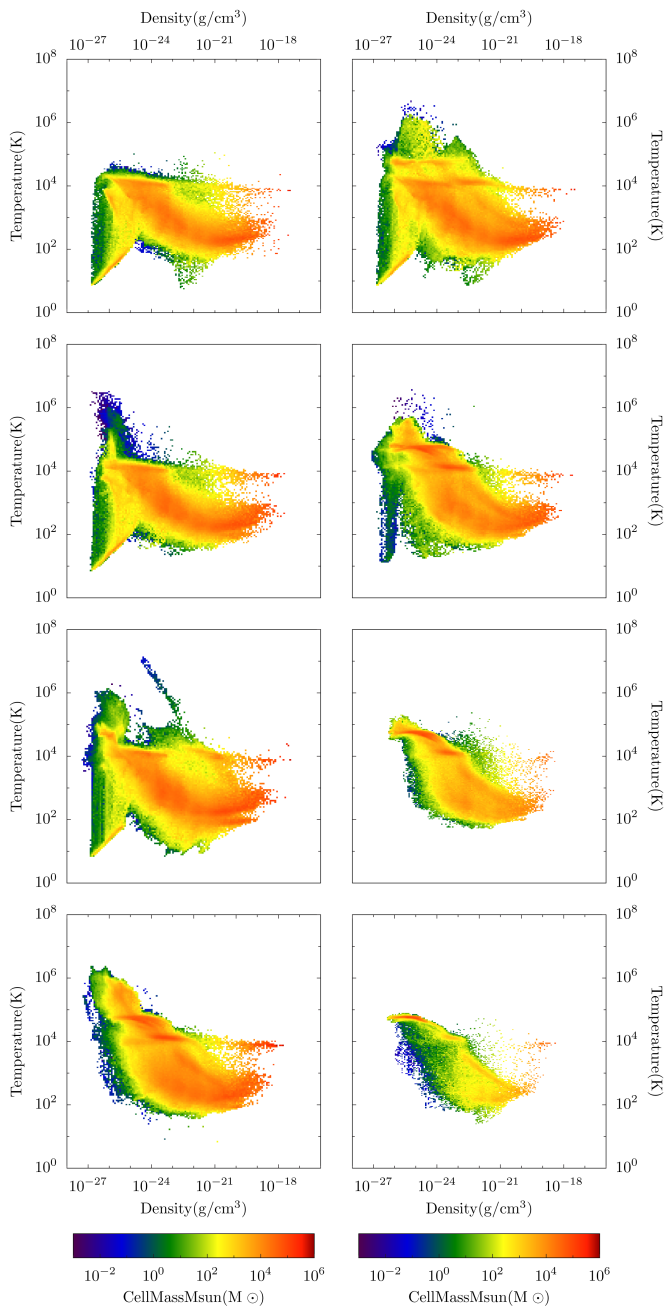
Figure 4.9 – Density-temperature phase diagram within a sphere of 1 kpc diameter for the XDR$_S$ (left) and XDR$_Z$ (right) cases at z = 14.95, 14.78, 14.54 and 13.54, from top to bottom.

density, within the central 200 pc, is only 10^{20} cm^{-2}, and the X-rays are not fully attenuated in this central region. Thus, the incident X-ray flux at large distances is high, leading to a high heating rate and H$_2$ formation rate. Furthermore, due to the long cooling times of the zero metallicity gas in the XDR$_Z$ case, it takes longer to reach high densities and adiabatic heating is not significant.

4.5   Discussion

As a proof of concept, we investigated the importance of metals in the vicinity of an Eddington-limited X-ray emitting MBH. The high temperatures (> 10^6 K, Figure 4.4) that are found in the inner regions around the MBH in the XDR$_S$ case might have severe consequences. These high temperatures can quench the gas accretion onto the black hole. Consequently, the accretion power decreases and thus negative radiative feedback becomes self-limiting. Furthermore, high opacity due to metals might aid star formation in some regions by shielding the high density gas against X-ray irradiation and allow gas to cool and collapse. On the other hand, in metal-poor regions, if an X-ray induced H $\textsc{ii}$ region forms, the latter can either quench star formation by removing gas or induce star formation by gas compression: As shown in our zero metallicity simulations, the X-ray driven H $\textsc{ii}$ region sweeps out a significant amount of mass which means that the growth of the black hole will be reduced. Moreover, this would also quench the star formation in the inner regions around the black hole. But, the H $\textsc{ii}$ ionization front might also induce star formation by compressing gas where otherwise stars would not form in gravitationally stable gas. Also, the redistribution of gas will cause a much flatter density profile in the central region than in the high metallicity case.

In this work, we showed that the difference between zero and solar metallicity gas irradiated by X-rays is very large and that in order to study the Magorrian relation a self-consistent treatment of the effects of metals on X-ray physics should be included. In paper II, we will include a star formation recipe and a Bondi Hoyle accretion rate for the growth of the MBH (Kim et al. 2011). We will also take into account metal enrichment by Pop III stars and its distribution in the central region by using XDR tables for different metallicities. This may shed further light on the origin of the Magorrian relation.
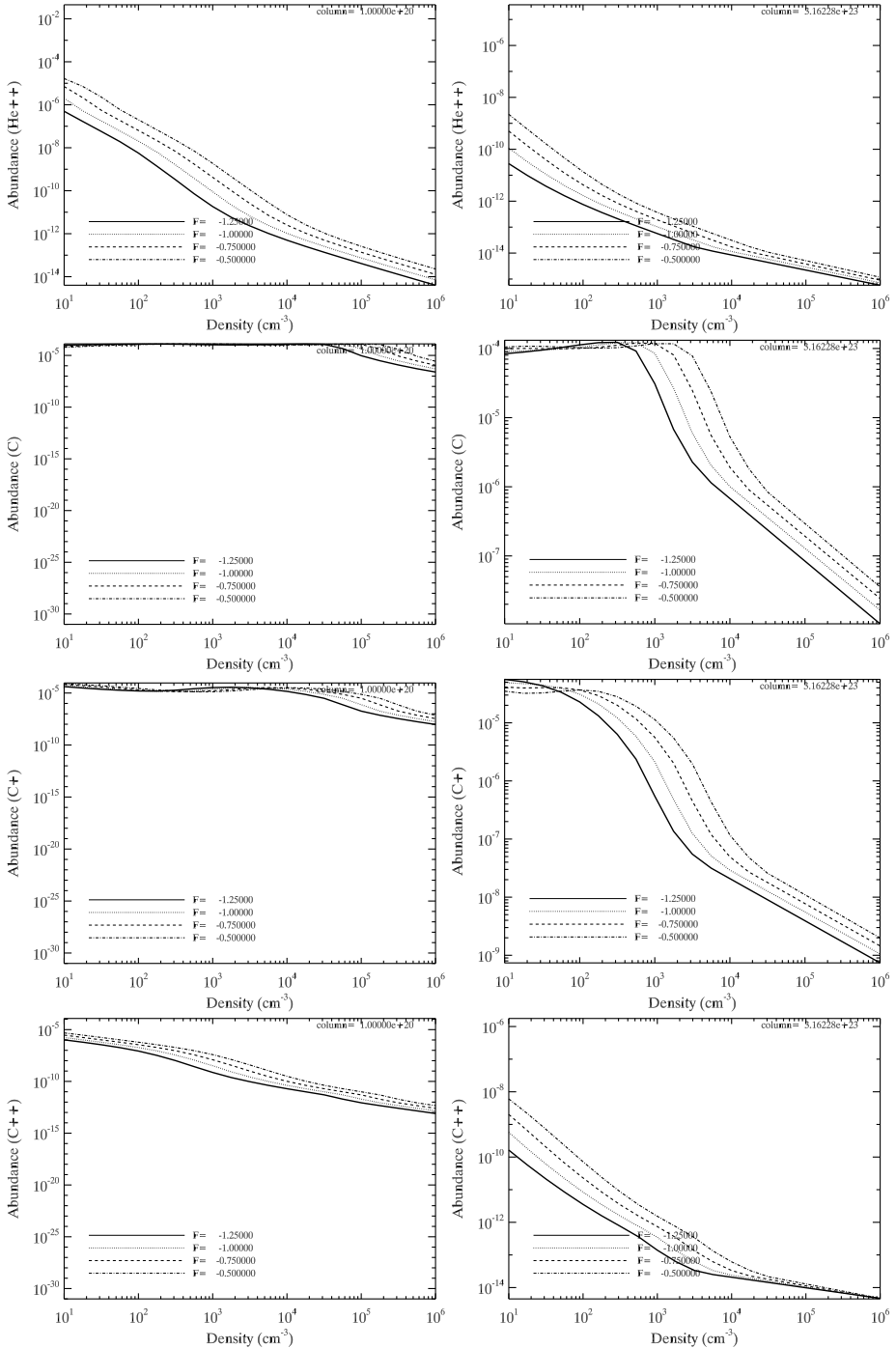
Appendix

In the following, we show a few models from the grid of XDR models. These are merely intended to illustrate the dynamic range and variety in XDR physics that Enzo has been augmented with.
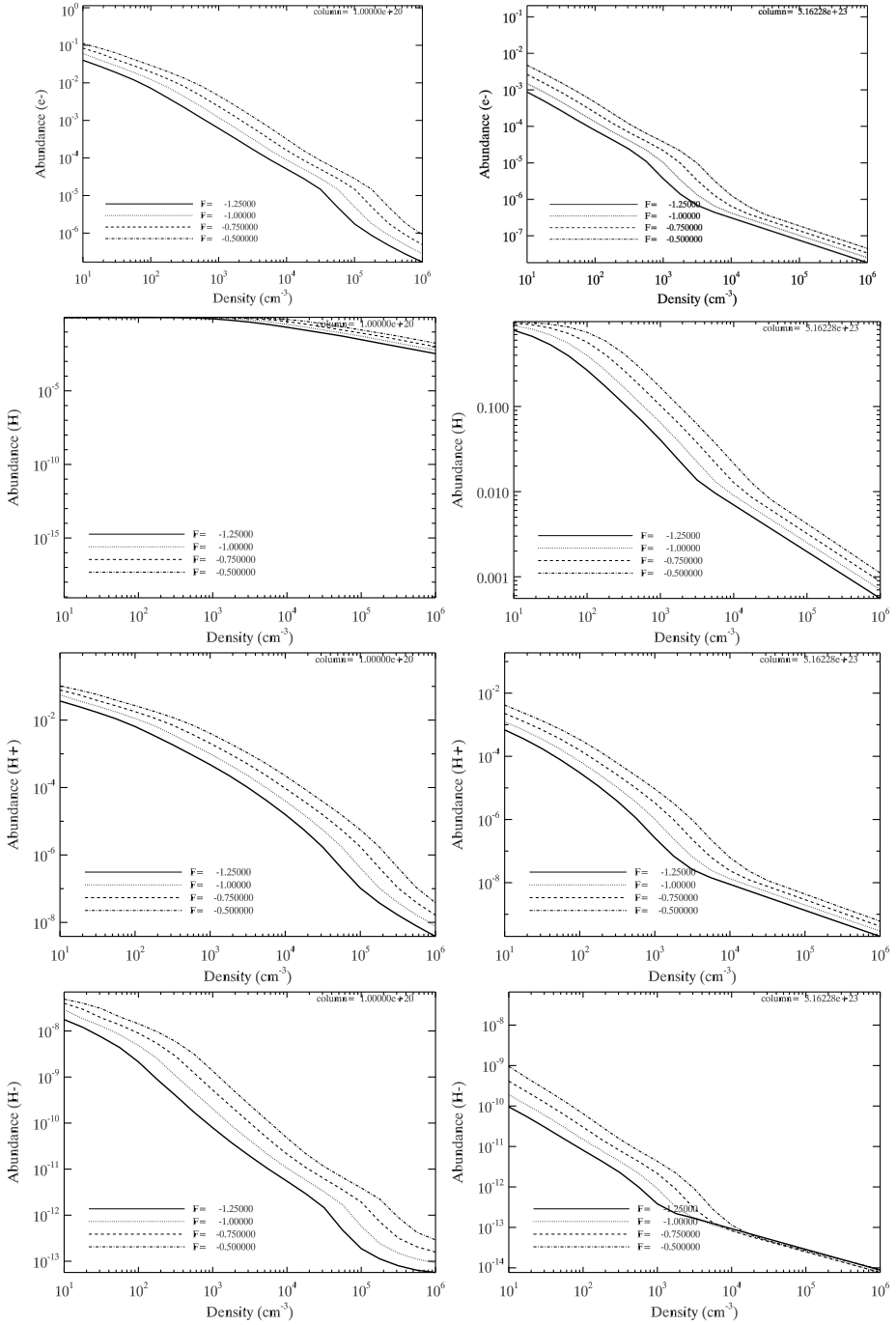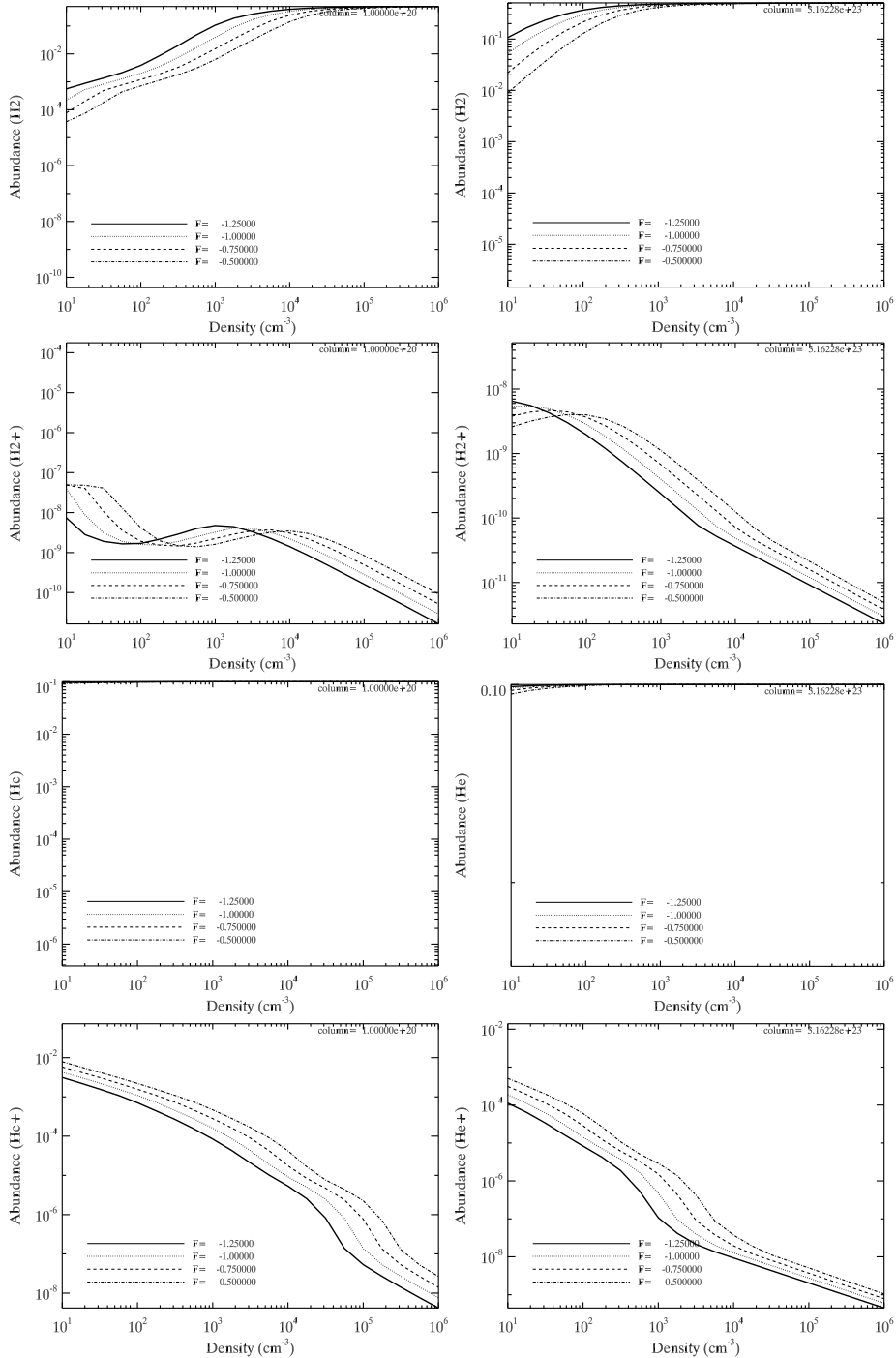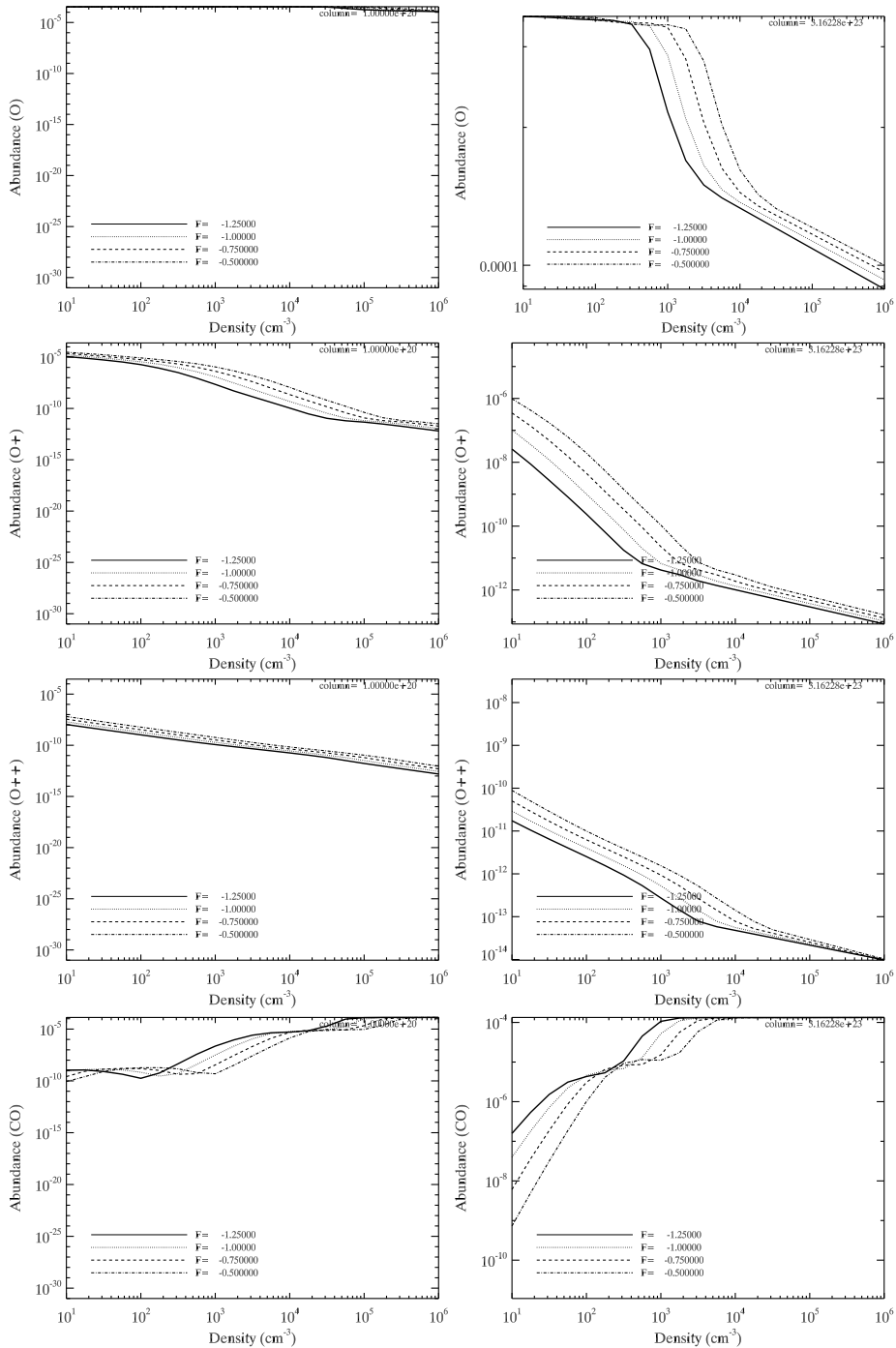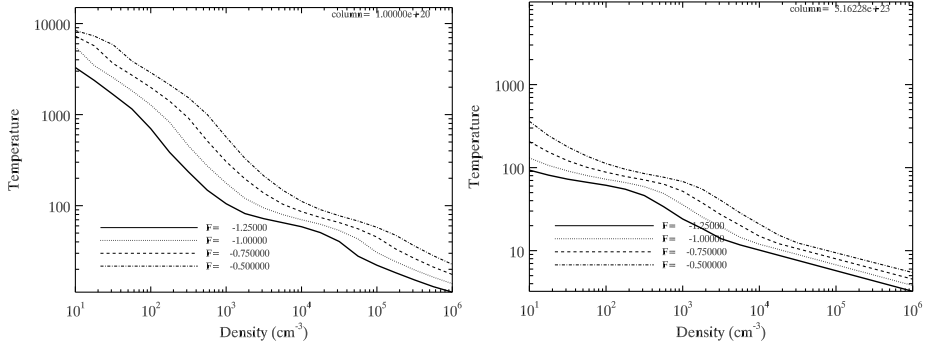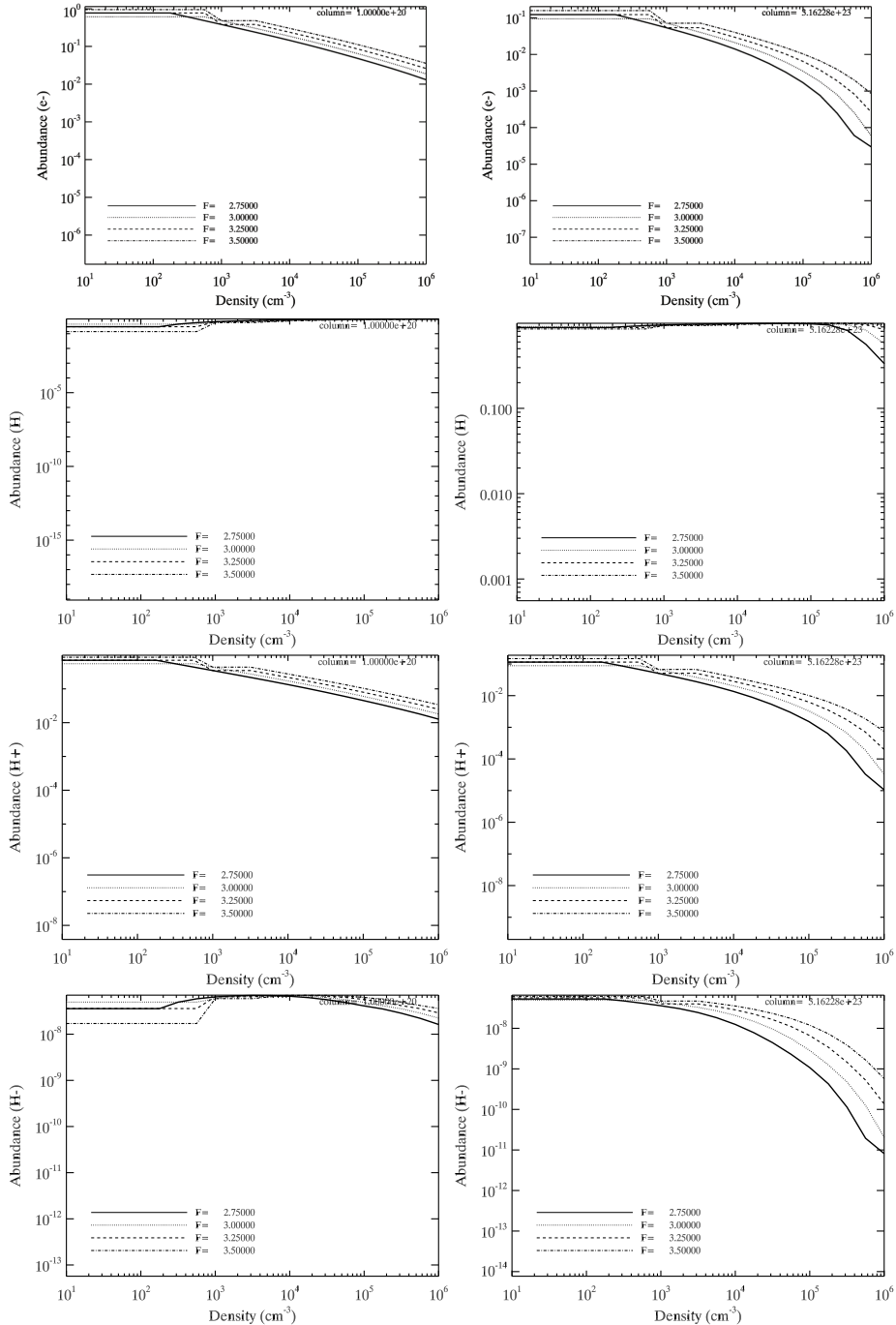
Figure 4.10 – Abundances of e^-, H, H^+, H^-, H_2, H_2^+, He, He^+, He^{2+}, C, C^+, C^{2+}, O, O^+, O^{2+}, CO and temperature for column densities of 10^{20} cm^{-2} (left column) and 10^{24} cm^{-2} (right column) for a X-ray flux of log F = -1.25 - -0.5 erg s^{-1} cm^{-2}.
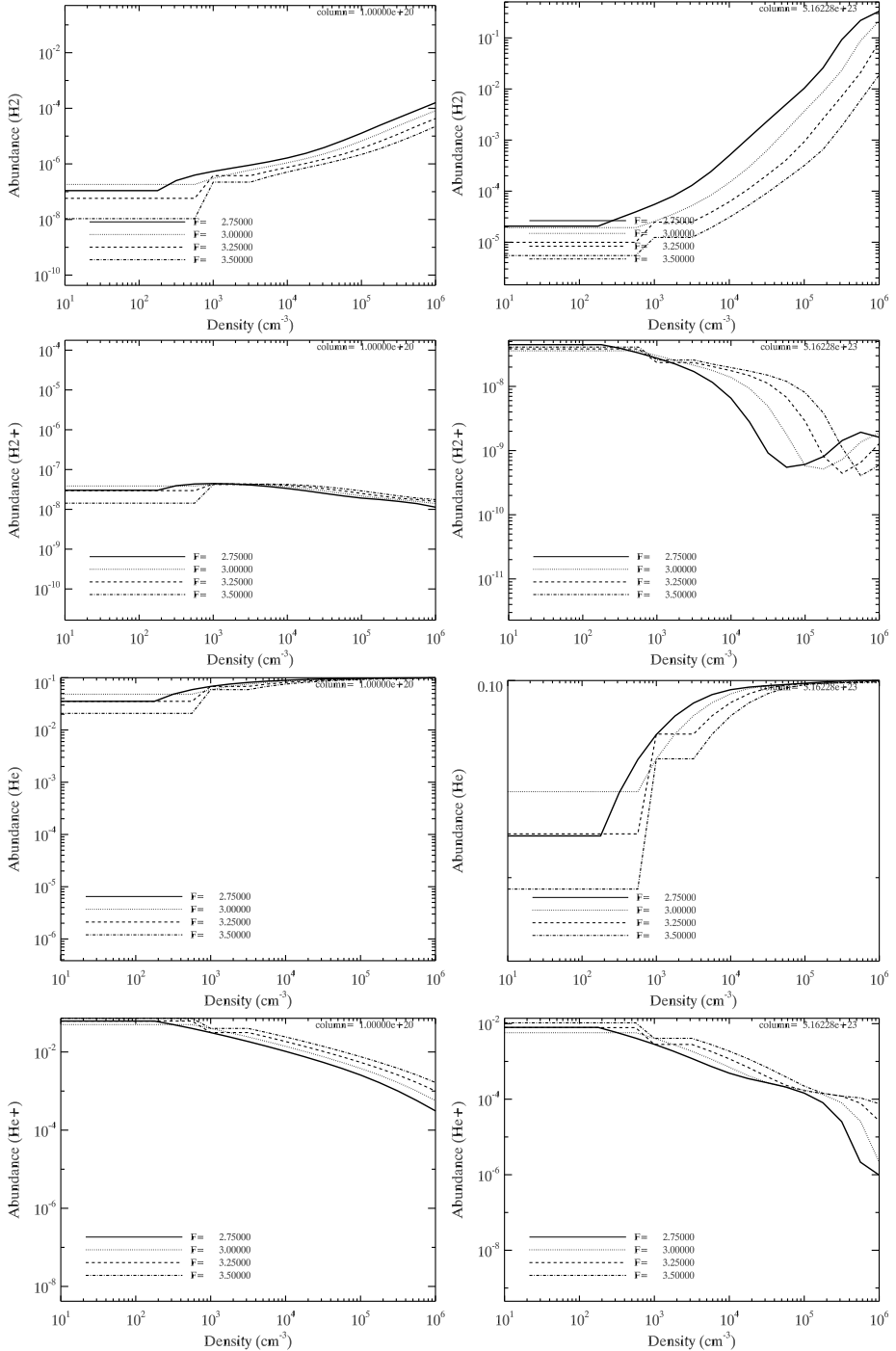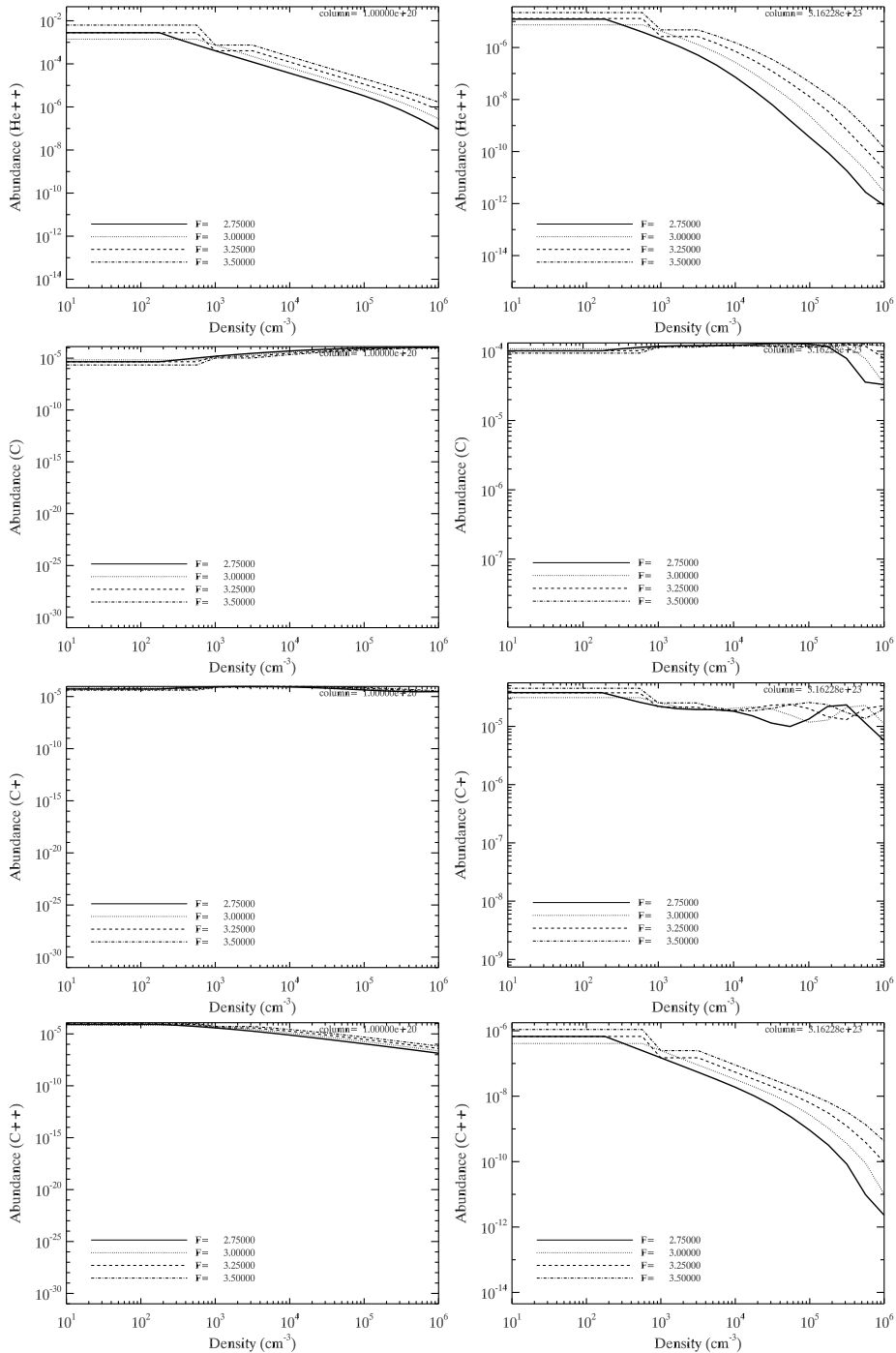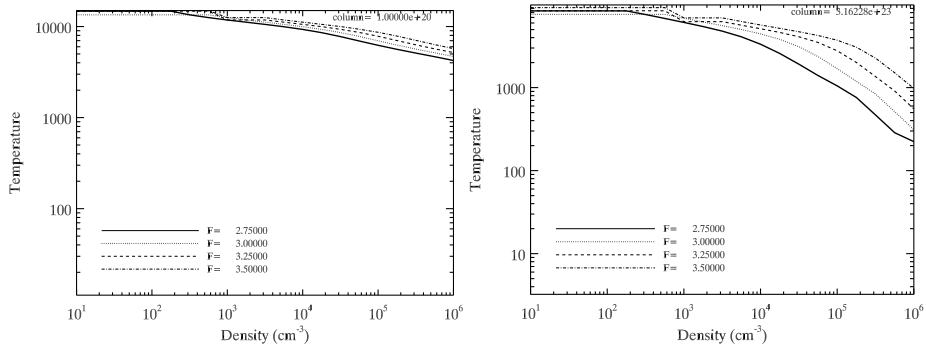
Figure 4.11 – Abundances of e^-, H, H^+, H^-, H_2, H_2^+, He, He^+, He^{2+}, C, C^+, C^{2+}, O, O^+, O^{2+}, CO and temperature for column densities of 10^{20} cm^{-2} (left column) and 10^{23} cm^{-2} (right column) for a X-ray flux of log F = 2.75 - 3.5 erg s^{-1} cm^{-2}.
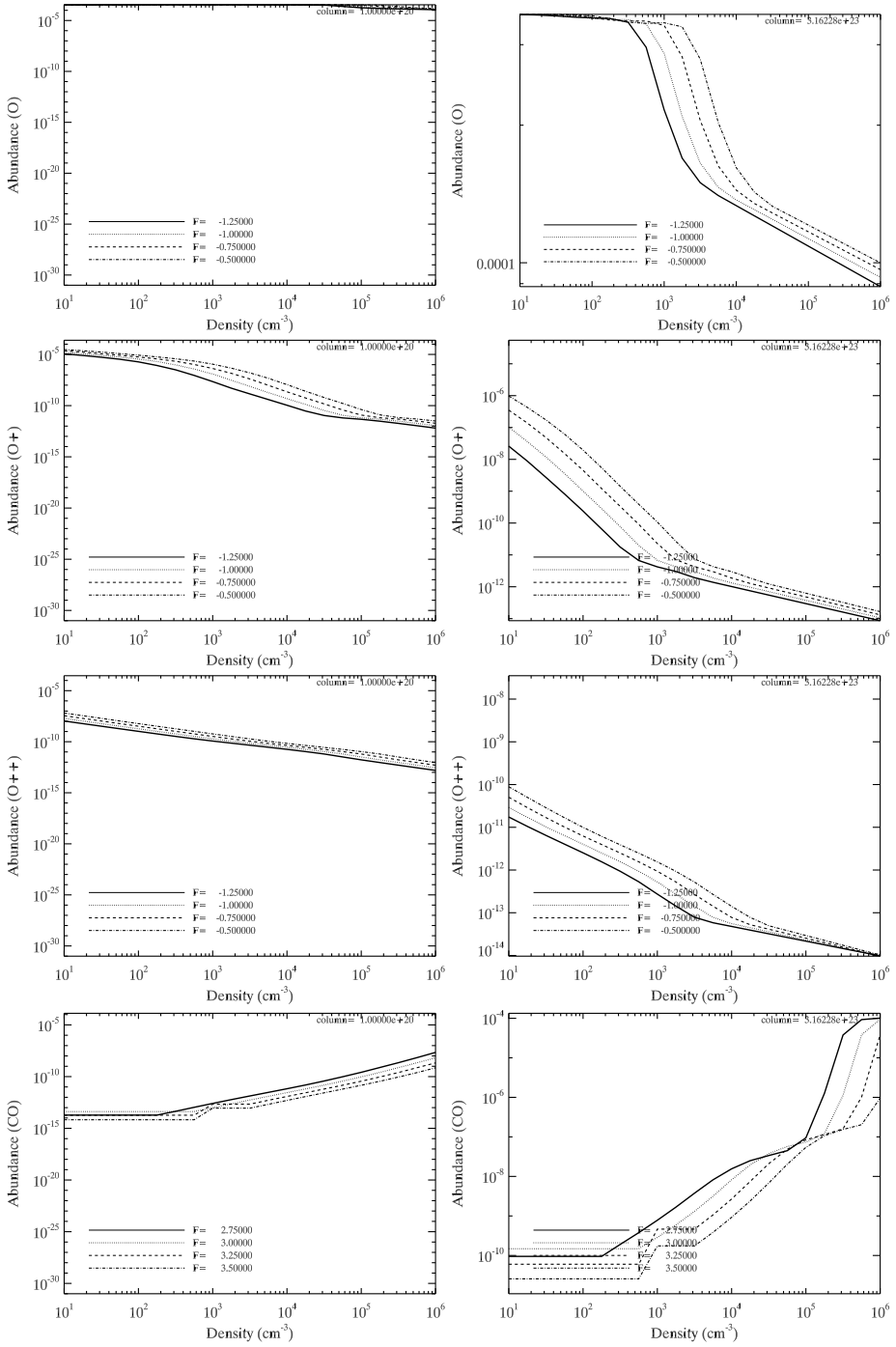
The Origin of SMBHs at z = 6: The Singular Collapse Scenario in the Presence of a UV Background Radiation Field

"You do not take from this universe. It grants you what it will".
Paul Atreides, Dune

A. Aykutalp, J. H. Wise, M. Spaans, R. Meijerink
To be submitted to ApJ, 2012

Abstract

In order to investigate the origin of SMBHs with masses on the order of 10^9 $M_\odot$ at z = 6, we performed two simulations by using the adaptive mesh refinement hydrodynamical code Enzo. In this, we simulate the singular collapse scenario in the presence of a UV background radiation field of 10^5 and 10^3 J_{21}. In our simulations we take into account the X-ray irradiation from a seed black hole with an initial mass of 5×10^4 $M_\odot$. We use XDR grid tables produced for a wide range of X-ray flux $F_X = 10^{-1.25}$-$10^{5.5}$ erg cm^{-2} s^{-1}, density n = $10 - 10^6$ cm^{-3}, column density $N_H = 10^{20} - 10^{24}$ cm^{-2}, and metallicity $Z/Z_\odot = 10^{-6}$, 10^{-4}, 10^{-2}, 1 values. To calculate the radiative transfer we employed the radiation transport module *Moray* and we use a polychromatic spectrum. Furthermore, we added H_2 self-shielding and use two different star formation recipes for the creation of Pop III and PopII/I stars and their feedback effects. We find that in the high UV background radiation case, we do not form Pop III stars until at least z = 10, due to the low H_2 fractions (10^{-8}). Moreover, the accretion rate is so low that at z = 12 (100 Myr after we insert the MBH) our MBH accreted only 100 $M_\odot$. Hence, we conclude that MBHs with masses of 5×10^4 $M_\odot$, which are formed through the singular collapse of an atomic cooling halo under the influence of strong UV background radiation field ($J = 10^5 J_{21}$), cannot be the origin of the SMBHs that we see at z = 6.

5.1   Introduction

In the last decade, the growth of supermassive black holes (SMBHs) in the centers of galaxies, and their role in shaping the evolution of galaxies and their star formation histories, has become the central topic for cosmology.

Observations of high redshift ($z > 6$) quasars suggest that these objects are powered by SMBHs with masses on the order of 10^9 $M_\odot$ (Fan et al. 2003, 2006b, Kurk et al. 2007). SMBHs are thought to be formed (in less than 1 billion years) through the accretion of gas onto seed black holes of masses between $10^2 - 10^5$ $M_\odot$. Central to the question of how these SMBHs with inferred masses of $M \sim 10^9$ $M_\odot$ can exist at such high redshifts, is how their seed black holes are formed. There are two plausible scenarios for the formation of these seed black holes: a) they are the remnants of the first stars ($M_{BH} \sim 10^2$ $M_\odot$, Volonteri et al. (2003), Volonteri & Rees (2005), Johnson & Bromm (2007)) and b) they are formed by the direct collapse of isothermal gas in atomic cooling halos ($M_{BH} \sim 10^4 - 10^6$ $M_\odot$, Haehnelt & Rees (1993), Umemura et al. (1993), Bromm & Loeb (2003a), Spaans & Silk (2006), Wise et al. (2008)) at the centers of the first galaxies.

In this work we simulate the latter scenario for the formation of a massive black hole (MBH, $M_{MBH} \sim 10^4 - 10^6$ $M_\odot$). In order to form a MBH through direct collapse, fragmentation into stars needs to be prevented. In metal-free gas the dominant coolant below 10^4 K is molecular hydrogen, H_2, which can cool the gas down to 200 K via ro-vibrational transitions. Hence, to avoid fragmentation the formation of H_2 needs to be suppressed. Indeed, in their studies Bromm & Loeb (2003a) and Spaans & Silk (2006) have shown that in the absence of H_2 fragmentation is sufficiently prevented. H_2 is fragile and can easily be dissociated by photons in the Lyman-Werner (LW) bands ($E = 11.2 - 13.6$ eV). Recent works on the photodissociation of H_2 in protogalaxies by Wolcott-Green et al. (2011) and Shang et al. (2010) have shown that a UV flux in the range of $10^3 - 10^5$ J_{21} is sufficient to prevent H_2 formation, and hence fragmentation, in halos with $T_{vir} = 10^4 - 10^5$ K.

Once the seed black hole is formed it can grow in mass through the accretion of gas. The amount of gas available for the MBHs to accrete depends on mergers and/or interactions between galaxies. In their work, Barnes & Hernquist (1991, 1996) have investigated the dynamics of gas in merging galaxies. They find that during major mergers, due to the gravitational tidal torques, there are events of rapid inflows of gas onto the central SMBHs. Furthermore, it has been long known that quasar activity and active galactic nuclei (AGN) are powered by the accretion of gas onto SMBHs (Salpeter 1964). Moreover, there is growing evidence that quasar activity is preceded by intense star formation (starbursts) in galactic nuclei (Sanders et al. 1988). In more recent work, Di Matteo et al. (2005) investigate the effect of energy input from quasars onto the host galaxy. They find that a major merger causes both starburst and rapid inflows of gas onto the SMBH. The latter enhances the quasar activity and the energy released by the SMBH expels the gas from the inner region thus quenching further star formation and the growth of the SMBH.

This led to the theory that an evolutionary sequence, caused by gas rich mergers, connects starbursts, quasars, SMBH growth, and the formation of red elliptical galaxies. Hopkins et al. (2006) suggest that right after the major merger, due to the ubiquitous presence of dust around the black hole, the quasar activity is obscured. Later on, when the black hole dominates the energetics of the central region, the energy input from the quasar quenches further star formation and expels the gas shrouding the quasar. This slows down the further growth of the SMBH and stops the quasar activity, which in turn leads to the formation of a normal spheroidal galaxy. Moreover, it has been found that nuclear star formation is tightly coupled to AGN activity (Hopkins & Quataert 2010). This theory is supported by observations of local galaxies, which have shown that ultraluminous infrared galaxies (ULIRGS) have similar bolometric luminosities as bright quasars and that they are often in mergers. Hence, ULIRGs are the possible candidates for the birthplaces of quasi-stellar objects (QSOs) (Sanders et al. 1988, van der Werf et al. 2011).

Observations of local galaxies in which a tight correlation between the mass of the central black hole and the velocity dispersion (Ferrarese & Merritt 2000, Gebhardt et al. 2000) or the mass of the host bulge (Magorrian et al. 1998) is seen, indicate that the formation and evolution of galaxies are coupled to the black hole's activities. Walter et al. (2004) derived the SMBH spheroidal bulge mass ratio in the high redshift universe to be an order of magnitude higher than what we observe in local galaxies, where the dynamical mass is estimated from the size and line width of the CO emission. This indicates that there might be an evolution in the $M_{BH} - M_{bulge}$ relation throughout cosmic time.

The accretion of gas onto the central black hole yields a luminous source of X-ray, UV, and optical photons. As studied in Aykutalp et al. 2012 (hereafter Paper I), the thermodynamics of the gas in the inner region of an AGN is dominated by the X-ray radiation produced by the infall of gas onto the central MBH. Thus, to understand the Magorrian relation it is crucial to include the X-ray radiation from the AGN.

In order to incorporate the effects of X-rays on the star formation around an AGN, and thus the coupling between the AGN and the central stellar spheroid, in a self-consistent manner, we have implemented the XDR/PDR chemical network of Meijerink & Spaans (2005) into Enzo (for details, see Paper I).

The aims of this paper are, for the singular collapse MBH formation scenario, to (1) investigate the possible connection between SMBHs and the formation and evolution of atomic cooling halos, (2) follow the accretion history of the seed black hole, and (3) assess the effects of episodic X-ray irradiation of the ambient gas by the MBH.

5.2   Simulations

In this work, we use the Eulerian adaptive mesh refinement (AMR) hydrodynamic code Enzo (Bryan & Norman 1997, 2000, O'Shea et al. 2004), which is modified to include metallicity dependent XDR physics, black hole physics, star formation recipes and H_2 self-shielding. We perform simulations in a three-dimensional periodic box with a side length of 3 h^{-1} Mpc, initialized at $z = 99$. The size of the root grid is 128^3 with three nested subgrids, each refined by a factor of two. The finest grid has an effective resolution of 1024^3 with a side length of 375 h^{-1} kpc. Refinement is restricted to the finest grid and occurs during the simulations whenever the baryonic matter or dark matter density is greater than the mean density by a factor of four. The maximum level of refinement that is reached in the finest grid is 10, allowing us to have a resolution of 3.6 pc. The virial mass of our halo at redshift z = 15 is $M_{vir} = 2.6 \times 10^8$, where M_{vir} is the mass in a sphere that encloses an average dark matter overdensity of 200. We use Wilkinson Microwave Anisotropy Probe seven-year cosmological parameters (Komatsu et al. 2009), which have the following values: $\Omega_\Lambda = 0.734$, $\Omega_m = 0.266$, $\Omega_b = 0.0449$, $\sigma_8 = 0.81$, and $h = 0.701$. Here, Ω_Λ is the vacuum energy, Ω_m is the matter density, Ω_b is the baryon density, σ_8 is the variance of random mass fluctuations in a sphere of radius 8 h^{-1} Mpc, and h is the Hubble parameter in units of 100 km s^{-1} Mpc^{-1}.

5.2.1   Black Hole Formation and Accretion

For our MBH to form at z = 15 through the direct collapse scenario, we need to avoid fragmentation due to H_2 cooling. Therefore, we introduce a UV background radiation field. In this, we assume that an early star formation epoch in a nearby minihalo is sufficient to build up such a UV background. We perform two simulations, one with a UV background radiation of 10^3 J_{21} (hereafter BG_3) and one for 10^5 J_{21} (hereafter BG_5), where $J_{21} = 10^{-21}$ erg s^{-1} cm^{-2} sr^{-1} Hz^{-1}. We turn on the LW background radiation field at z = 30. Recent work by Wolcott-Green et al. (2011) has shown that such J_{LW} values are sufficient to keep our halo almost H_2 free.

H_2 self-shielding is crucial for the formation of stars in regions where the H_2 column densities exceed 10^{14} cm^{-2}. Thus, we take into account H_2 self-shielding as well as optical depth effects in H I, He I, and He II. In this, we use a local approximation for the H_2 self-shielding and multiply the H_2 photo-dissociation rate by a self-shielding factor f_{sh} to correct the impinging UV flux in the LW band (Draine & Bertoldi 1996). We use the equation given by Shang et al. (2010) for f_{sh}

$$f_{sh} \;=\; min\left[1, \left(\frac{N_{H_2}}{10^{14} \mathrm{cm}^{-2}}\right)^{-3/4}\right], \tag{5.1}$$

$$N_{H_2} \;=\; f_{H_2} n_{tot} \lambda_J. \tag{5.2}$$

Here, N_{H_2} is the H_2 column density, n_{tot} is the total particle number density, and λ_J is the jeans length ($\lambda_J = \sqrt{\frac{15 k_b T}{4\pi G \mu \rho}}$).

At redshift z = 15 we insert a MBH with a mass of $M = 5 \times 10^4$ $M_\odot$. We follow the radiative feedback from the MBH using the Enzo radiation transport module *Moray* (Wise & Abel 2011b). To calculate the gas temperature, we use an XDR grid of models produced for a large parameter space in density n, X-ray Flux F_X, column density N_H and metallicity $Z/Z_\odot$ (see section 5.2.3). We employ *Moray* to compute the full (chemical, thermal and hydrodynamic) response of X-ray exposed gas. To trace the propagation of the X-rays through the ISM in a self-consistent manner we use a polychromatic X-ray spectrum. The details of this approach are described in Paper I.

For the accretion of gas onto the MBH we use the prescription of Kim et al. (2011). We calculate the accretion rate by using the Eddington-limited spherical Bondi-Hoyle equation

$$
\begin{aligned}
\dot{M}_{BH} &= min(\dot{M}_B, \dot{M}_{Edd}) \\
&= min\left(\frac{4\pi G^2 M_{BH}^2 \rho_B}{c_s^3}, \frac{4\pi G M_{BH} m_p}{\epsilon \sigma_T c}\right),
\end{aligned}
\tag{5.3}
$$

where G is the gravitational constant, M_{BH} is the mass of the MBH, ρ_B is the density at the Bondi radius, c_s is the sound speed, m_p is the mass of a proton, ϵ is the radiative efficiency, and σ_T is the Thomson scattering cross-section.

5.2.2 Star Formation and Feedback

In order to model the interplay between stellar and black hole feedback, we employ different recipes for Pop III and PopII/I star formation. We turn on the star formation recipes at z = 30 and constrain the star formation to occur only in the finest subgrid. For the Pop III star formation we modified the star formation algorithm of Cen & Ostriker (1992) as follows. In our simulation a Pop III star particle is created when all of the following criteria are met:

(1) the metallicity of the gas is less than $10^{-3.5}$ solar,

(2) the molecular hydrogen fraction is greater than 5×10^{-4},

(3) the cooling time t_{cool} is shorter than the dynamical time t_{dyn},

(4) the velocity flow is converging; i.e., $\nabla \cdot \mathbf{v} < 0$.

For the Pop II/I star formation recipe we use the algorithm of Cen & Ostriker (1992) in Enzo with an additional metallicity criterion. Hence, in our simulation a Pop II/I star particle is formed when the following criteria are met: (1) the metallicity of the gas is greater than $10^{-3.5}$ solar, (2) the velocity flow is converging; i.e., $\nabla \cdot \mathbf{v} < 0$, (3) t_{cool} is smaller than t_{dyn}. For every star particle that is created, ionizing

radiation transport is included following the prescriptions of Wise et al. (2012). I.e., every star particle produces its own H II region. The energy injection by the supernova explosions (SNe) of Pop III stars is computed from the stellar mass and is deposited in a sphere of 10 pc radius.

5.2.3 XDR Grids

We tabulated XDR grids using a modified version of the XDR/PDR chemical network of Meijerink & Spaans (2005). Our chemical network consists of 176 species and more than 1000 reactions.

The main heating mechanism in X-ray dominated regions (XDRs) is Coulomb heating when fast electrons interact with thermal electrons. Consequently, the heating efficiency in XDRs is high, 10 - 30%. Moreover, X-rays have small absorption cross-sections, which roughly scale as $1/E^3$, and thus they can penetrate large columns. The important parameter in XDRs, for the chemical and thermal structure of the gas, is the energy deposition rate to the total gas density. In Paper I, we find that the energy deposition rate in a solar metallicity gas is much higher than for the zero metallicity case, which causes high temperatures ($\sim 10^7$ K) in the central region. Moreover, earlier work on the X-ray effects from an AGN by Pérez-Beaupuits et al. (2011) has shown that X-ray exposed molecular gas has temperatures 5 times higher than gas in a starburst of equal bolometric power. This has important consequences for the initial mass function (IMF) of stars, because the Jeans Mass (M_J) scales with the temperature of the ambient gas as $M_J \propto T^{3/2}$.

In XDRs, at high temperatures (T > 5000 K) the gas cooling is dominated by collisional excitation of Lyα, and forbidden and semi-forbidden transitions of [O I] ($\lambda\lambda$ 6300, 6363 μm), [C I] ($\lambda\lambda$ 9823, 9850 μm), [Fe II]($\lambda\lambda$ 1.26, 1.64 μm), and [Si II] ($\lambda\lambda$ 6716, 6731μm). At low temperatures, below a few 1000 K, gas cooling is dominated by the fine-structure lines of [OI] 63 μm, [SiII] 35 μm, [CII] 158 μm, [CI] 269 and 609 μm, as well as rotational lines of CO and H_2O. For further details, we refer the interested reader to Meijerink & Spaans (2005) and Paper I.

We constructed tables for species abundances and gas temperatures over a wide range of X-ray flux $F_X = 10^{-1.25} - 10^{5.5}$ erg cm^{-2} s^{-1}, density n = $10 - 10^6$ cm^{-3}, column density $N_H = 10^{20} - 10^{24}$ cm^{-2} and metallicity $Z/Z_\odot = 10^{-6}, 10^{-4}, 10^{-2}, 1$. This large parameter space enables us to model the ISM properties close to an AGN properly. We use Enzo's 9 species (H, H$^+$, H$^-$, He, He$^+$, He^{2+}, H$_2$, H$_2^-$, and e$^-$) non-equilibrium chemical network for zero metallicity gas. We follow the metal production by SNe and thus determine which of the XDR tables is appropriate for the gas thermodynamics.

5.3 Results & Discussions

We have performed two simulations, one with a UV background radiation field of 10^3 and one for 10^5 J_{21}, where we turn on the radiation field, H_2 self-shielding and the star formation recipes at z = 30. Both simulations have a seed MBH with a mass of M = 5×10^4 $M_\odot$ in the center of our halo, which we insert at z = 15.

The main difference between the BG_5 and BG_3 runs is the H_2 fraction. In the BG_5 run, the strong UV background radiation photo-dissociates the H_2 more efficiently than in the BG_3 case. Therefore, in the BG_5 run the H_2 fraction in the central 100 pc is as low as $\sim 10^{-8}$, whereas in the BG_3 run it is 10^{-6}. This is shown in Figure 5.1, where we plot density, temperature and H_2 fraction slices in the y-plane at z = 15 for the BG_5 (top) and BG_3 (bottom) runs. The corresponding H_2 column density (for a typical density of 10^{-21} g cm^{-3}) over a scale of 30 pc is 10^{15} and 10^{17} cm^{-2} in the BG_5 and BG_3 runs, respectively. Thus, self-shielding occurs but it is not very strong yet, given the broad line wings in the H_2 dissociative bands. Under these initial conditions, in our atomic cooling halo with $T_{vir} \sim 10^4$ K, we therefore do not form any Pop III stars in either of the runs prior to z = 15. Hence, our direct collapse scenario for the formation of the seed MBH is appropriate.

2 Myr after we insert the MBH into the center of our halo, the accretion rate in the BG_5 case is $\sim 10^{-6}$ $M_\odot$ yr^{-1}. This corresponds to a total energy production of 2×10^{53} ergs over 1 Myr for an efficiency of 10% Eddington, which is about the same as the energy produced by 200 supernova explosions, as shown in Figure 5.2 (left panel). This energy input, produced by the accretion of matter onto the central MBH, drives an H II region that expels the gas from the inner region of the halo with a velocity of $\sim$ 100 km s^{-1}. This is shown in Figure 5.3, where we plot the divergence of the velocity field and velocity magnitude slices in the y-plane at z = 14.1 (so 25 Myr after we insert the MBH). In Figures 5.4 and 5.5, where we plot the phase diagrams and enclosed mass, respectively, the removal of the mass from the inner 1 kpc is clearly seen. Moreover, radiative feedback from the central MBH helps to maintain the gas temperatures around 10^4 K. Combined, the accretion rate decreases to 10^{-10} $M_\odot$ yr^{-1} about 25 Myr after we insert the MBH (see Figure 5.2). Furthermore, the strength of the X-ray flux is also changing with time, dependant on the episodes of accretion that the MBH enjoys. We find that black hole growth is self-regulating, i.e., when accreting the MBH produces strong X-ray radiation, which then shuts down the accretion. This, in turn, decreases the X-ray flux and hence allows gas to cool and flow to the black hole again. As shown in Figure 5.6, where we plot the X-ray flux slices in the x-, y-, and z-plane for the BG_5 case at redshifts z = 14.95, 14.39, 13.22, 12.86, 12.15, and 12.00, from left to right and top to bottom, the X-ray flux flickers in response to the changes in the accretion rate.

For the BG_5 case we do not find any Pop III star formation until at least z = 10. This is a direct consequence of the MBH feedback that drives an H II region through episodic accretion and the strong UV background radiation field that suppresses the H_2 abundance to $\sim 10^{-8}$. This is shown in Figure 5.7, where we plot the H_2 fraction with radius at z = 12. Thus, as also exemplified in Figure 5.4
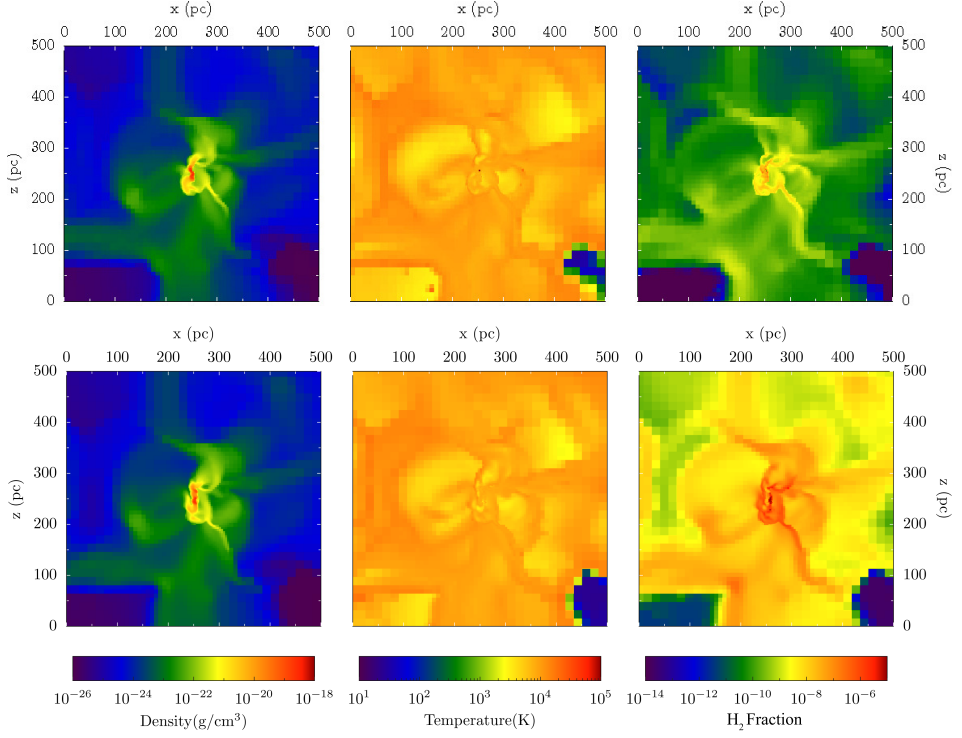
Figure 5.1 – Density, temperature and H_2 fraction slices in the y-plane at z = 15 for the BG_5 (top) and BG_3 (bottom) runs.
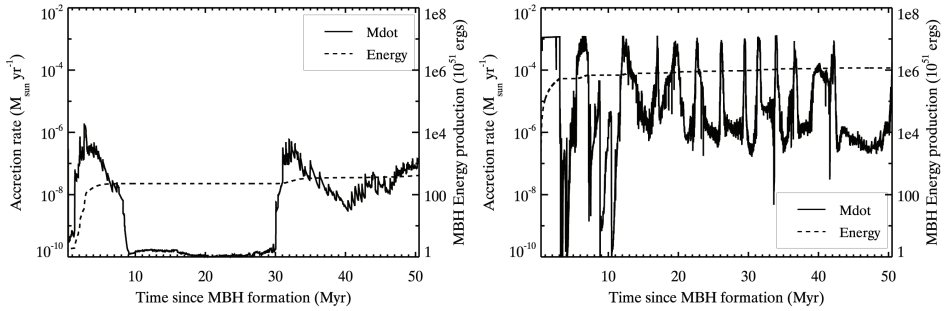

Figure 5.2 – Accretion rate and the corresponding total energy production of the central MBH over time for the BG_5 (left) and BG_3 (right) runs.
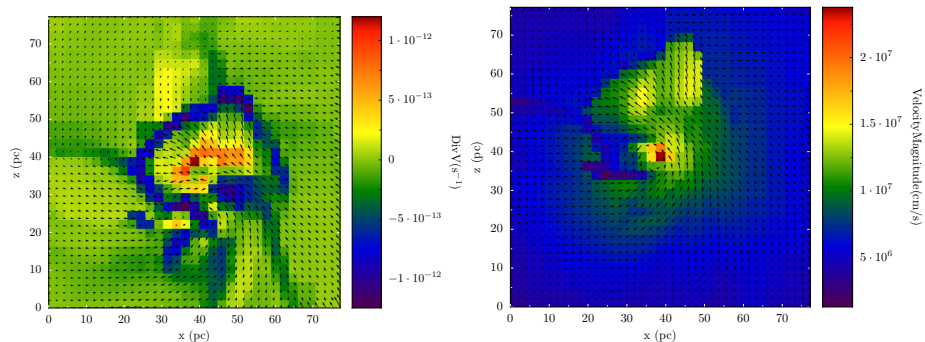
101

Figure 5.3 – Divergence of the velocity field and velocity magnitude slices in the y-plane for the BG_5 case at z = 14.1 (25 Myr after we inserted the MBH).

(right panel), there is no cool dense phase at z = 12 that may facilitate Pop III star formation.

On the other hand, in the BG_3 case right after we insert the MBH (0.265 Myr later), the first Pop III star forms. This is because, prior to z = 15, the H_2 abundance in the BG_3 case was already ∼ 2 orders of magnitude higher than in the BG_3 case (see Figure 4) and in a short period of time, about 0.3 Myr, it has reached a value where it meets our Pop III formation criterion (5×10^{-4}). In fact, for the BG_3 run we obtain a duty cycle of close to 50%. The BG_5 case yields more than an order of magnitude less (3-5%). These numbers are similar to Park & Ricotti (2012). Our high UV background run is in "mode I/6%" and our low UV one in "mode II/50%", in the terminology of Park & Ricotti (2012).

In Figure 5.8, we compare the H_2 abundances of the BG_5 and BG_3 cases at different timesteps. As is clearly seen at any time the H_2 fraction in the BG_3 case is higher and there is more mass compared to the BG_5 case with a higher H_2 fraction, despite the fact that there is additional radiative feedback from formed Pop III stars.

In Figure 5.9, we overplot Pop III star particles on a density projection in the y-plane at z = 14.95. At z = 14.95, there are 90 Pop III stars formed with a total stellar mass of 6930 $M_\odot$. Moreover, the accretion rate of the MBH after 1 Myr is 10^{-3} $M_\odot$ yr^{-1}, which is 3 orders of magnitude higher than in the BG_5 case (see Figure 5.2). Once again this is because of the ability of H_2 rich gas to cool efficiently, even on a short timescale, which in turn allows the MBH to accrete at a higher rate than the BG_5 case. Hence, the energy production by the MBH is 3 orders of magnitude higher. Thus, it also has a stronger impact on the ambient gas. In Figure 5.10, we plot the 2D radial profile of X-ray flux as a function of radius (left) and slices of the X-ray flux (middle) and the column density (right) in the y-plane at z = 14.95 for the inner 150 pc. Although in the BG_3 case X-ray fluxes are 6 orders of magnitude higher than in the BG_5 case, X-rays do not penetrate as far as in the BG_3 case. This
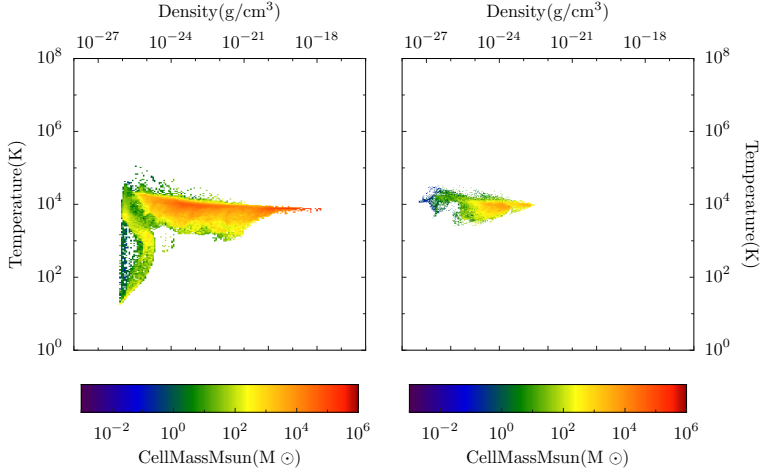
Figure 5.4 – Density-temperature phase diagrams within a sphere of 1 kpc diameter at z = 14.95 (left) and z = 12.05 (right) for the BG$_5$ case.
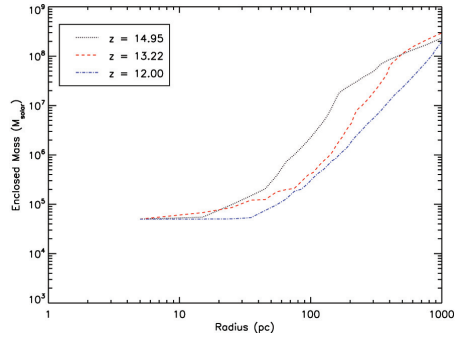

Figure 5.5 – Enclosed mass of the BG$_5$ run at z = 14.95 (black dotted line), 13.22 (red-dashed line) and 12.00 (blue dotted-dashed line)
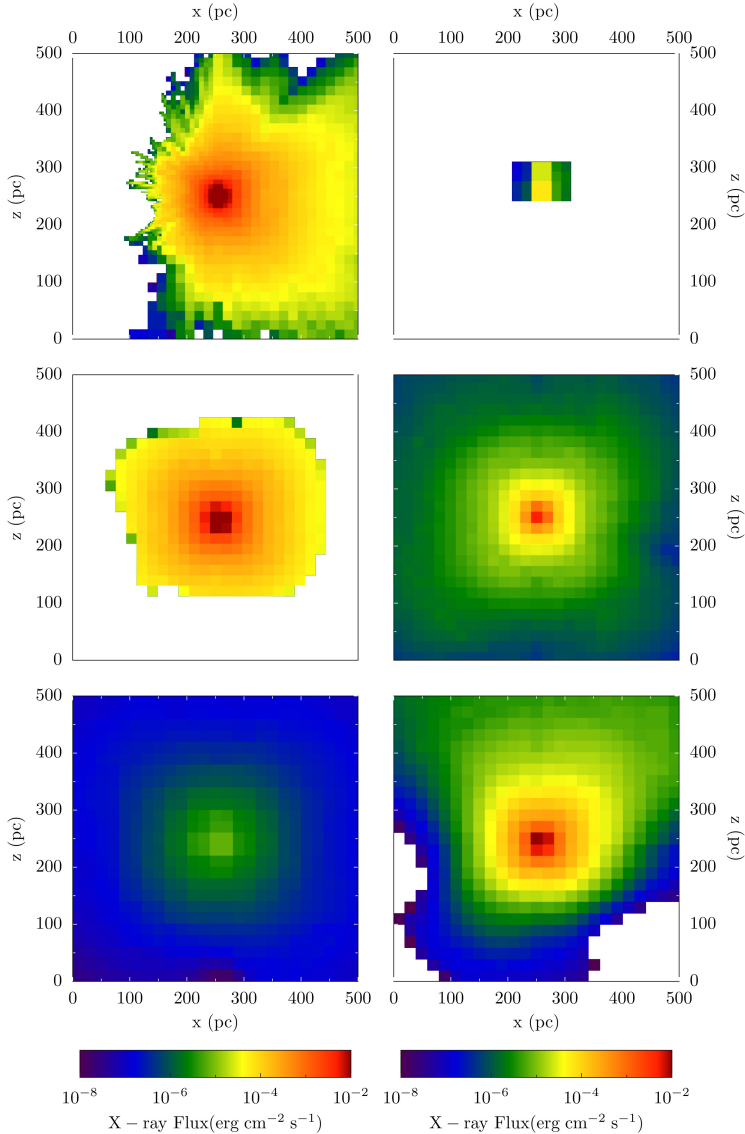
Figure 5.6 – Evolution of X-ray flux with time. The individual windows show slices through the, from left to right, x-, y-, z- planes centered on the MBH. The different redshifts shown are, from top to bottom (left) z = 14.95, 13.22, 12.15, and (right) z = 14.39, 12.86, 12.00.
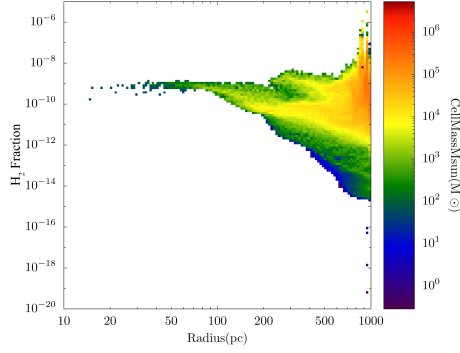
Figure 5.7 – 2D profile of H_2 fraction with respect to radius at z = 12.00 for the BG_5 case.
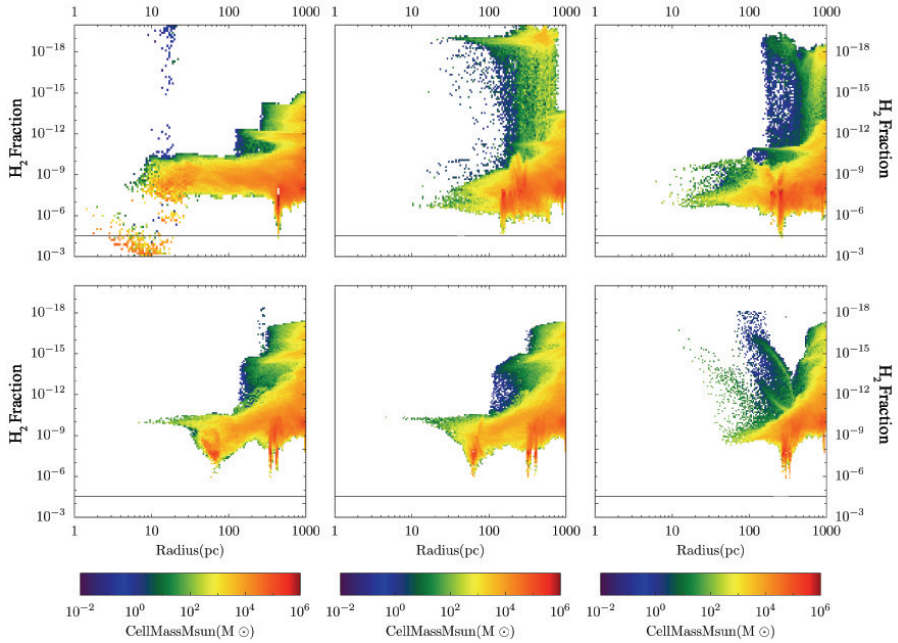

Figure 5.8 – 2D profile of H_2 fraction with respect to radius for the BG_5 (top) and BG_3 (bottom) cases at z = 14.95 (left), 14.86 (middle), 14.78 (right). The horizontal solid line in each plot represents the f_{H_2} threshold for Pop III star formation.
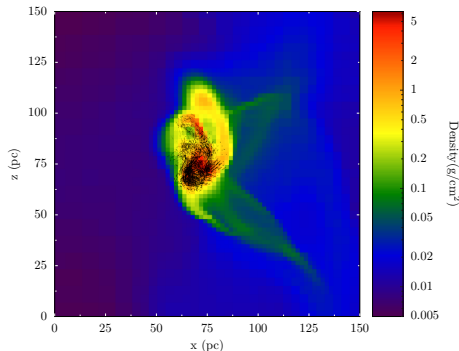
Figure 5.9 – Density projection in the y-plane at z = 14.95 for the BG_3 case. Black dots represent Pop III stars.

is due to the high column densities, on the order of 10^{23-24} cm^{-2}, that are reached in the center (see middle and right panels in Figure 5.10). Also, as shown in the left panel of Figure 5.10, in the inner 20 pc the X-ray flux is strongly attenuated by the interstellar matter. Therefore, the energy deposition rate into the medium is higher than in the BG_5 case.

At z = 14.86, the first SNe go off and enrich our halo up to solar metallicities. We show the metal enrichment of our halo in Figure 5.11, where we plot the phase diagram with metallicity color coded (left) for a sphere of 1 kpc diameter, a slice of the metallicity field (middle) and the metal density (right), in the y-plane at z = 14.78. This metal enrichment further enhances the inflow of matter onto the MBH by cooling the gas efficiently. Moreover, it gives a rise to the formation of the next generation (Pop II/I) of stars. Note in the left panel of Figure 5.11 that the high metallicity ($\sim 1 \, Z_\odot$) dense (≥ 1 cm^{-3}) gas is warmer than low ($\leq 10^{-2} Z_\odot$) metallicity gas. This is a result of the high X-ray opacity of metal-rich gas, which leads to a large energy deposition rate (Paper I). Furthermore, the fast metal enrichment for the BG_3 run, see Figure 5.11, provides a high opacity for X-ray absorption because the local metallicity reaches almost solar and absorptions by inner shell electrons of C, N and O have large cross sections above 1 keV. Consequently, at 3 pc one already reaches an optical depth of unity for ~ 2 keV X-ray photons, as indicated by the warm metal-rich gas. The BG_5 run stays metal-free and > 1 keV X-rays can travel out to > 50 pc before reaching an optical depth of unity. Therefore, the typical time scale for accretion to occur, i.e., the response time of ambient gas to X-ray feedback, is more than an order of magnitude longer in the high UV run.

According to our results, it seems unlikely that the bulk of the 10^9 M$_\odot$ SMBHs at z $\sim$ 6 is formed through the direct collapse of an 10^8 M$_\odot$ atomic halo under the influence of a strong 10^5 J$_{21}$ UV background radiation field. However, these slowly evolving MBHs might find a natural habitat inside dwarf galaxies that we see in the local universe today. Star formation and MBH growth in such systems

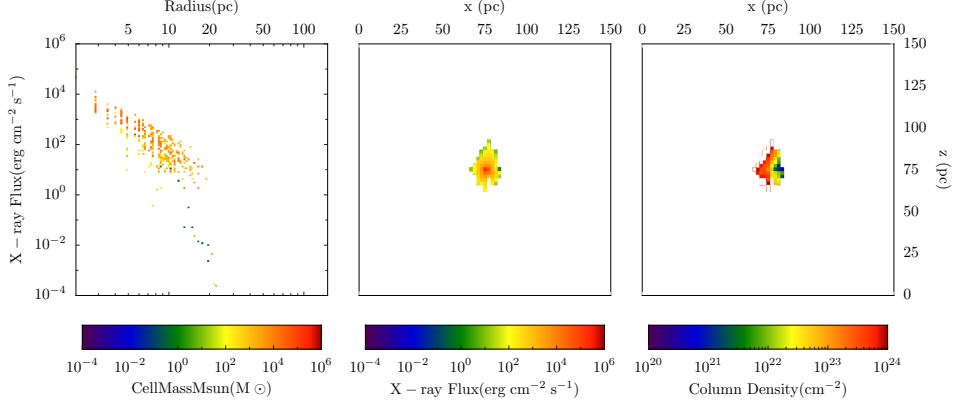**Figure 5.10** – 2D radial profile of X-ray flux as a function of radius (left) and slices of the X-ray flux (middle) and the column density (right) in the y-plane at z = 14.95 for the BG$_3$ case.
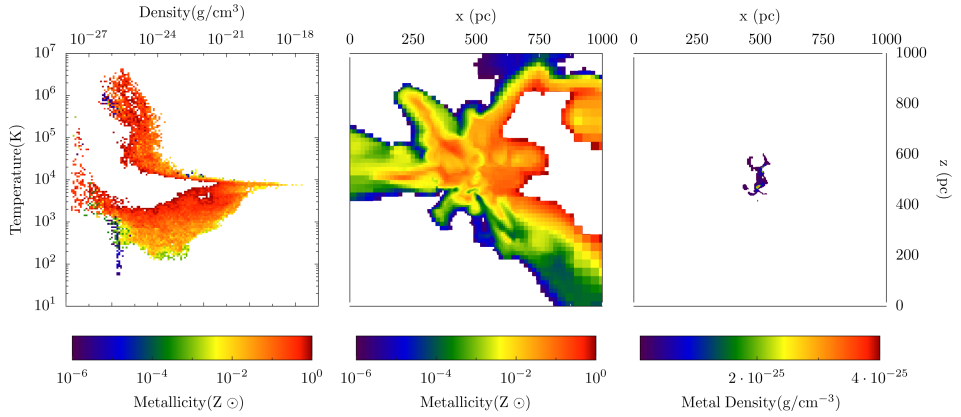

Figure 5.11 – Phase diagram with metallicity color coded for a sphere of 1 kpc diameter (left), a slice of the metallicity field (middle) and the metal density (right), in the y-plane at z = 14.78 for the BG$_3$ case.
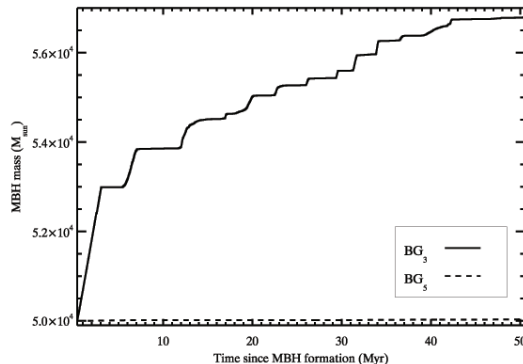
Figure 5.12 – Growth of the MBH for the BG_5 (dashed line) and BG_3 (solid line) cases.

would require a weakening of the UV background and/or some metal enrichment ($Z/Z_\odot > 10^{-3}$) by external sources (Aykutalp & Spaans 2011). On the other hand, in the BG_3 case the growth of the MBH is more rapid such that in only 7 Myr the MBH gains $\sim 4 \times 10^3$ $M_\odot$. We plot the growth of the MBH in the BG_5 and BG_3 runs in Figure 6. This indicates that within an Eddington time (in $\sim$ 100 Myr) the MBH will double its mass. Therefore, we conclude that MBHs in the presence of a mild UV background radiation field (10^3 J_{21}) are probable candidates for z = 6 SMBHs.

N_{H_2} is a non-local quantity, but because of the high computational expenses of determining self-shielding accurately, we have estimated the H_2 self-shielding effect by using a local approximation. This local approximation method has been shown to be accurate within an order of magnitude only (Shang et al. 2010). Our simulations assume a constant UV background, which might not be realistic since the source of the UV radiation field and its effect on our halo depends on the position and evolution of the source. Also, our spatial resolution is 3.6 pc. Hence, we do not resolve the region close to the MBH very well. Moreover, in this work we did not take into account the mechanical feedback from the central MBH. Jets that are produced by the MBH might further help to remove gas from the central region and hence quench accretion onto the MBH. On the other hand, at the edges of these jets, star formation might be enhanced due to the compression of ambient gas. We will include mechanical feedback effects from the central MBH in a follow-up paper.

Despite these caveats, our results indicate a strong interplay between the MBH and its global environment in establishing the Magorrian relation. In particular, the presence of a strong UV background renders a primordial atomic cooling halo of $\sim 10^8$ $M_\odot$ fragile to radiative feedback by a MBH.

Bibliography

Abel, T., Anninos, P., Zhang, Y., & Norman, M. L. 1997, New A, 2, 181

Abel, T., Bryan, G. L., & Norman, M. L. 2001, in Astronomical Society of the Pacific Conference Series, Vol. 222, The Physics of Galaxy Formation, ed. M. Umemura & H. Susa, 129–+

Abel, T., Bryan, G. L., & Norman, M. L. 2002, Science, 295, 93

Abel, T., Norman, M. L., & Madau, P. 1999, ApJ, 523, 66

Abel, T., Wise, J. H., & Bryan, G. L. 2007, ApJ, 659, L87

Ádámkovics, M., Glassgold, A. E., & Meijerink, R. 2011, ApJ, 736, 143

Alvarez, M. A., Bromm, V., & Shapiro, P. R. 2006, ApJ, 639, 621

Amanullah, R., Lidman, C., Rubin, D., et al. 2010, ApJ, 716, 712

Anninos, P., Zhang, Y., Abel, T., & Norman, M. L. 1997, New A, 2, 209

Asplund, M., Grevesse, N., & Sauval, A. J. 2005, in Astronomical Society of the Pacific Conference Series, Vol. 336, Cosmic Abundances as Records of Stellar Evolution and Nucleosynthesis, ed. T. G. Barnes III & F. N. Bash, 25–+

Astier, P., Guy, J., Regnault, N., et al. 2006, A&A, 447, 31

Aykutalp, A. & Spaans, M. 2011, ApJ, 737, 63

Bahcall, J. N., Kirhakos, S., & Schneider, D. P. 1996, ApJ, 457, 557

Bakes, E. L. O. & Tielens, A. G. G. M. 1994, ApJ, 427, 822

Baldry, I. K. & Glazebrook, K. 2003, ApJ, 593, 258

Barnes, J. & Efstathiou, G. 1987, ApJ, 319, 575

Barnes, J. E. & Hernquist, L. 1996, ApJ, 471, 115

Barnes, J. E. & Hernquist, L. E. 1991, ApJ, 370, L65

Bromm, V., Coppi, P. S., & Larson, R. B. 2002, ApJ, 564, 23

Bromm, V., Ferrara, A., Coppi, P. S., & Larson, R. B. 2001, MNRAS, 328, 969

Bromm, V. & Loeb, A. 2003a, ApJ, 596, 34

Bromm, V. & Loeb, A. 2003b, Nature, 425, 812

Bromm, V., Yoshida, N., & Hernquist, L. 2003, ApJ, 596, L135

Bryan, G. L. & Norman, M. L. 1997, in Astronomical Society of the Pacific Conference Series, Vol. 123, Computational Astrophysics; 12th Kingston Meeting on Theoretical Astrophysics, ed. D. A. Clarke & M. J. West, 363–+

Bryan, G. L. & Norman, M. L. 2000, Institute for Mathematics and Its Applications, 117, 165

Burles, S., Nollett, K. M., & Turner, M. S. 1999, ArXiv Astrophysics e-prints

Casey, C. M., Chapman, S. C., Neri, R., et al. 2011, MNRAS, 415, 2723

Cazaux, S. & Spaans, M. 2004, ApJ, 611, 40

Cazaux, S. & Spaans, M. 2009, A&A, 496, 365

Cazaux, S. & Tielens, A. G. G. M. 2002, ApJ, 575, L29

Cen, R. & Ostriker, J. P. 1992, ApJ, 399, L113

Chabrier, G. 2003, PASP, 115, 763

Chevallier, M. & Polarski, D. 2001, International Journal of Modern Physics D, 10, 213

Ciardi, B., Ferrara, A., & Abel, T. 2000, ApJ, 533, 594

Clark, P. C., Glover, S. C. O., & Klessen, R. S. 2008, ApJ, 672, 757

Comastri, A. & Brusa, M. 2008, Astronomische Nachrichten, 329, 122

Cravens, T. E. & Dalgarno, A. 1978, ApJ, 219, 750

Dalgarno, A. & Lepp, S. 1987, in IAU Symposium, Vol. 120, Astrochemistry, ed.
    M. S. Vardya & S. P. Tarafdar, 109–118

Dalgarno, A., Yan, M., & Liu, W. 1999, ApJS, 125, 237

Di Matteo, T., Springel, V., & Hernquist, L. 2005, Nature, 433, 604

Dijkstra, M., Haiman, Z., & Loeb, A. 2004a, ApJ, 613, 646

Dijkstra, M., Haiman, Z., Rees, M. J., & Weinberg, D. H. 2004b, ApJ, 601, 666

Draine, B. T. & Bertoldi, F. 1996, ApJ, 468, 269

Fan, X., Strauss, M. A., Becker, R. H., et al. 2006a, AJ, 132, 117

Fan, X., Strauss, M. A., Richards, G. T., et al. 2006b, AJ, 131, 1203

Fan, X., Strauss, M. A., Schneider, D. P., et al. 2003, AJ, 125, 1649

Ferrarese, L. & Merritt, D. 2000, ApJ, 539, L9

Fujita, A., Mac Low, M.-M., Ferrara, A., & Meiksin, A. 2004, ApJ, 613, 159

Galli, D. & Palla, F. 1998, A&A, 335, 403

Garnavich, P. M., Jha, S., Challis, P., et al. 1998, ApJ, 509, 74

Gebhardt, K., Bender, R., Bower, G., et al. 2000, ApJ, 539, L13

Glassgold, A. E. & Langer, W. D. 1973, ApJ, 179, L147+

Glover, S. 2008, in American Institute of Physics Conference Series, Vol. 990, First Stars III,
    ed. B. W. O'Shea & A. Heger, 25–29

Glover, S. C. O. & Abel, T. 2008, MNRAS, 388, 1627

Górski, K. M., Hivon, E., Banday, A. J., et al. 2005, ApJ, 622, 759

Gould, R. J. & Salpeter, E. E. 1963, ApJ, 138, 393

Graham, A. W., Onken, C. A., Athanassoula, E., & Combes, F. 2011, MNRAS, 412, 2211

Haehnelt, M. G. & Rees, M. J. 1993, MNRAS, 263, 168

Haiman, Z., Abel, T., & Rees, M. J. 2000, ApJ, 534, 11

Haiman, Z., Rees, M. J., & Loeb, A. 1997, ApJ, 476, 458

Hawking, S. W. 1975, Communications in Mathematical Physics, 43, 199

Heckman, T. M., Bothun, G. D., Balick, B., & Smith, E. P. 1984, AJ, 89, 958

Heger, A. & Woosley, S. E. 2002, ApJ, 567, 532

Hetznecker, H. & Burkert, A. 2006, MNRAS, 370, 1905

Hocuk, S. & Spaans, M. 2010, A&A, 522, A24

Hocuk, S. & Spaans, M. 2011, A&A, 536, A41

Hollenbach, D. & McKee, C. F. 1979, ApJS, 41, 555

Hopkins, A. M. & Beacom, J. F. 2006, ApJ, 651, 142

Hopkins, P. F., Cox, T. J., Kereš, D., & Hernquist, L. 2008, ApJS, 175, 390

Hopkins, P. F., Hernquist, L., Cox, T. J., et al. 2006, ApJS, 163, 1

Hopkins, P. F. & Quataert, E. 2010, MNRAS, 407, 1529

Hosokawa, T., Omukai, K., Yoshida, N., & Yorke, H. W. 2011, Science, 334, 1250

Hořava, P. 2009, Phys. Rev. D, 79, 084008

Jacobson, T. 2010, Phys. Rev. D, 82, 129901

Jacobson, T. & Mattingly, D. 2001, Phys. Rev. D, 64, 024028

Jappsen, A., Klessen, R. S., Glover, S. C. O., & Mac Low, M. 2009, ApJ, 696, 1065

Jappsen, A.-K., Glover, S. C. O., Klessen, R. S., & Mac Low, M.-M. 2007, ApJ, 660, 1332

Jeans, J. H. 1928, Astronomy and cosmogony, ed. Jeans, J. H.

Jenkins, E. B. 2004, Origin and Evolution of the Elements, 336

Jiang, L., Fan, X., Vestergaard, M., et al. 2007, AJ, 134, 1150

Johnson, J. L. & Bromm, V. 2006, MNRAS, 366, 247

Johnson, J. L. & Bromm, V. 2007, MNRAS, 374, 1557

Johnson, J. L., Greif, T. H., & Bromm, V. 2008, MNRAS, 388, 26

Kauffmann, G. & Haehnelt, M. 2000, MNRAS, 311, 576

Kim, J.-h., Wise, J. H., Alvarez, M. A., & Abel, T. 2011, ApJ, 738, 54

Kitayama, T., Yoshida, N., Susa, H., & Umemura, M. 2004, ApJ, 613, 631

Komatsu, E., Dunkley, J., Nolta, M. R., et al. 2009, ApJS, 180, 330

Komatsu, E., Smith, K. M., Dunkley, J., et al. 2011, ApJS, 192, 18

Kormendy, J. & Gebhardt, K. 2001, in American Institute of Physics Conference Series,
    Vol. 586, 20th Texas Symposium on relativistic astrophysics, ed. J. C. Wheeler &
    H. Martel, 363–381

Kormendy, J. & Richstone, D. 1995, ARA&A, 33, 581

Kroupa, P. 2002, Science, 295, 82

Kuhlen, M. & Madau, P. 2005, MNRAS, 363, 1069

Kurk, J. D., Walter, F., Fan, X., et al. 2007, ApJ, 669, 32

Latter, W. B. & Black, J. H. 1991, ApJ, 372, 161

Le Bourlot, J., Pineau des Forêts, G., & Flower, D. R. 1999, MNRAS, 305, 802

Lepp, S. & Shull, J. M. 1983, ApJ, 270, 578

Li, Z., Wu, P., & Yu, H. 2012, ApJ, 744, 176

Linder, E. V. 2003, Physical Review Letters, 90, 091301

Mac Low, M.-M. & Ferrara, A. 1999, ApJ, 513, 142

Machacek, M. E., Bryan, G. L., & Abel, T. 2001, ApJ, 548, 509

Mackey, J., Bromm, V., & Hernquist, L. 2003, ApJ, 586, 1

Madau, P., Ferrara, A., & Rees, M. J. 2001, ApJ, 555, 92

Madejski, G. M., Zdziarski, A. A., Turner, T. J., et al. 1995, ApJ, 438, 672

Magorrian, J., Tremaine, S., Richstone, D., et al. 1998, AJ, 115, 2285

Maloney, P. R., Hollenbach, D. J., & Tielens, A. G. G. M. 1996, ApJ, 466, 561

McConnell, N. J., Ma, C.-P., Gebhardt, K., et al. 2011, Nature, 480, 215

McKee, C. F. & Tan, J. C. 2008, ApJ, 681, 771

Meijerink, R. 2006, PhD thesis, Leiden Observatory

Meijerink, R. & Spaans, M. 2005, A&A, 436, 397

Mellema, G., Iliev, I. T., Alvarez, M. A., & Shapiro, P. R. 2006, New A, 11, 374

Merloni, A. 2004, MNRAS, 353, 1035

Mori, M., Ferrara, A., & Madau, P. 2002, ApJ, 571, 40

Morrison, R. & McCammon, D. 1983, ApJ, 270, 119

Murray, S., Gilli, R., Tozzi, P., et al. 2009, in ArXiv Astrophysics e-prints, Vol. 2010,
    astro2010: The Astronomy and Astrophysics Decadal Survey, 217–+

Nagakura, T. & Omukai, K. 2005, MNRAS, 364, 1378

Nakamura, F. & Umemura, M. 2002, ApJ, 569, 549

Narayanan, D., Cox, T. J., Hayward, C. C., Younger, J. D., & Hernquist, L. 2009, MNRAS, 400, 1919

Narayanan, D., Hayward, C. C., Cox, T. J., et al. 2010, MNRAS, 401, 1613

Nishi, R. & Susa, H. 1999, ApJ, 523, L103

Nozawa, T., Kozasa, T., Umeda, H., Maeda, K., & Nomoto, K. 2003, ApJ, 598, 785

Oh, S. P. & Haiman, Z. 2002, ApJ, 569, 558

Oh, S. P. & Haiman, Z. 2003, MNRAS, 346, 456

O'Leary, R. M., O'Shaughnessy, R., & Rasio, F. A. 2007, Phys. Rev. D, 76, 061504

Omukai, K., Tsuribe, T., Schneider, R., & Ferrara, A. 2005, ApJ, 626, 627

O'Shea, B. W., Abel, T., Whalen, D., & Norman, M. L. 2005, ApJ, 628, L5

O'Shea, B. W., Bryan, G., Bordner, J., et al. 2004, ArXiv Astrophysics e-prints

O'Shea, B. W. & Norman, M. L. 2007, ApJ, 654, 66

Page, D. N. & Hawking, S. W. 1976, ApJ, 206, 1

Palla, F., Salpeter, E. E., & Stahler, S. W. 1983, ApJ, 271, 632

Park, K. & Ricotti, M. 2012, ApJ, 747, 9

Peebles, P. J. E. 1969, ApJ, 155, 393

Peebles, P. J. E. 1980, The large-scale structure of the universe, ed. Peebles, P. J. E.

Peebles, P. J. E. 1993, Principles of Physical Cosmology, ed. Peebles, P. J. E.

Peebles, P. J. E. & Dicke, R. H. 1968, ApJ, 154, 891

Pérez-Beaupuits, J. P., Wada, K., & Spaans, M. 2011, ApJ, 730, 48

Perlmutter, S., Aldering, G., della Valle, M., et al. 1998, Nature, 391, 51

Perlmutter, S., Aldering, G., Goldhaber, G., et al. 1999, ApJ, 517, 565

Poelman, D. R. & Spaans, M. 2005, A&A, 440, 559

Pounds, K. A., Nandra, K., Stewart, G. C., George, I. M., & Fabian, A. C. 1990, Nature, 344, 132

Press, W. H. & Schechter, P. 1974, ApJ, 187, 425

Puy, D., Alecian, G., Le Bourlot, J., Leorat, J., & Pineau Des Forets, G. 1993, A&A, 267, 337

Rawlings, J. M. C., Drew, J. E., & Barlow, M. J. 1993, MNRAS, 265, 968

Richstone, D., Ajhar, E. A., Bender, R., et al. 1998, Nature, 395, A14

Riess, A. G., Filippenko, A. V., Challis, P., et al. 1998, AJ, 116, 1009

Salpeter, E. E. 1964, ApJ, 140, 796

Salvaterra, R., Ferrara, A., & Schneider, R. 2004, New A, 10, 113

Sanders, D. B. & Mirabel, I. F. 1996, ARA&A, 34, 749

Sanders, D. B., Scoville, N. Z., Young, J. S., et al. 1986, ApJ, 305, L45

Sanders, D. B., Soifer, B. T., Elias, J. H., et al. 1988, ApJ, 325, 74

Sanders, R. H. 2011, Phys. Rev. D, 84, 084024

Santoro, F. & Shull, J. M. 2006, ApJ, 643, 26

Saslaw, W. C. & Zipoy, D. 1967, Nature, 216, 976

Scannapieco, E., Ferrara, A., & Madau, P. 2002, ApJ, 574, 590

Schleicher, D. R. G., Spaans, M., & Klessen, R. S. 2010, A&A, 513, A7+

Schmidt, B. P., Suntzeff, N. B., Phillips, M. M., et al. 1998, ApJ, 507, 46

Schneider, R., Ferrara, A., Natarajan, P., & Omukai, K. 2002, ApJ, 571, 30

Seljak, U., Makarov, A., McDonald, P., et al. 2005, Phys. Rev. D, 71, 103515

Shakura, N. I. & Sunyaev, R. A. 1973, A&A, 24, 337

Shang, C., Bryan, G. L., & Haiman, Z. 2010, MNRAS, 402, 1249

Shapiro, P. R., Iliev, I. T., & Raga, A. C. 2004, MNRAS, 348, 753

Shapiro, P. R. & Kang, H. 1987, ApJ, 318, 32

Sheth, R. K. & Tormen, G. 1999, MNRAS, 308, 119

Shull, J. M. & van Steenberg, M. E. 1985, ApJ, 298, 268

Silk, J. 1983, MNRAS, 205, 705

Smith, B. D. & Sigurdsson, S. 2007, ApJ, 661, L5

Smith, B. D., Turk, M. J., Sigurdsson, S., O'Shea, B. W., & Norman, M. L. 2009, ApJ, 691, 441

Soltan, A. 1982, MNRAS, 200, 115

Spaans, M. 1997, Nuclear Physics B, 492, 526

Spaans, M. & Meijerink, R. 2008, ApJ, 678, L5

Spaans, M. & Silk, J. 2000, ApJ, 538, 115

Spaans, M. & Silk, J. 2005, ApJ, 626, 644

Spaans, M. & Silk, J. 2006, ApJ, 652, 902

Springel, V., Di Matteo, T., & Hernquist, L. 2005a, ApJ, 620, L79

Springel, V., Di Matteo, T., & Hernquist, L. 2005b, MNRAS, 361, 776

Springel, V. & Hernquist, L. 2003, MNRAS, 339, 289

Stancil, P. C., Lepp, S., & Dalgarno, A. 1998, ApJ, 509, 1

Stiavelli, M. 2009, From First Light to Reionization: The End of the Dark Ages, ed. Stiavelli, M.

Sugiyama, N. 1995, ApJS, 100, 281

Sullivan, M., Guy, J., Conley, A., et al. 2011, ApJ, 737, 102

Tacconi, L. J., Genzel, R., Smail, I., et al. 2008, ApJ, 680, 246

Tan, J. C. & Blackman, E. G. 2004, ApJ, 603, 401

Taylor, C. L., Hüttemeister, S., Klein, U., & Greve, A. 1999, A&A, 349, 424

Tegmark, M., Silk, J., Rees, M. J., et al. 1997, ApJ, 474, 1

Tielens, A. G. G. M. & Hollenbach, D. 1985, ApJ, 291, 722

Truelove, J. K., Klein, R. I., McKee, C. F., et al. 1997, ApJ, 489, L179+

Tumlinson, J. 2006, ApJ, 641, 1

Tumlinson, J. 2007a, ApJ, 665, 1361

Tumlinson, J. 2007b, ApJ, 664, L63

Turk, M. 2008, in Proceedings of the 7th Python in Science Conference, ed. G. Varoquaux, T. Vaught, & J. Millman, Pasadena, CA USA, 46 – 50

Turk, M. J., Clark, P., Glover, S. C. O., et al. 2011a, ApJ, 726, 55

Turk, M. J., Smith, B. D., Oishi, J. S., et al. 2011b, ApJS, 192, 9

Umemura, M., Loeb, A., & Turner, E. L. 1993, ApJ, 419, 459

Urry, C. M. & Padovani, P. 1995, PASP, 107, 803

Vader, J. P. 1986, ApJ, 305, 669

van der Werf, P. P., Berciano Alba, A., Spaans, M., et al. 2011, ApJ, 741, L38

Vasiliev, E. O. & Shchekinov, Y. A. 2006, Astronomy Reports, 50, 778

Verner, D. A. & Yakovlev, D. G. 1995, A&AS, 109, 125

Vishniac, E. T. 1983, ApJ, 274, 152

Voit, G. M. 1991, ApJ, 377, 158

Volonteri, M., Haardt, F., & Madau, P. 2003, ApJ, 582, 559

Volonteri, M. & Rees, M. J. 2005, ApJ, 633, 624

Wada, K., Papadopoulos, P. P., & Spaans, M. 2009, ApJ, 702, 63

Wada, K. & Venkatesan, A. 2003, ApJ, 591, 38

Walter, F., Carilli, C., Bertoldi, F., et al. 2004, ApJ, 615, L17

Wang, Y. 2012, ArXiv e-prints

Watson, D., Denney, K. D., Vestergaard, M., & Davis, T. M. 2011, ApJ, 740, L49

Whalen, D., Abel, T., & Norman, M. L. 2004, ApJ, 610, 14

Whalen, D., van Veelen, B., O'Shea, B. W., & Norman, M. L. 2008, ApJ, 682, 49

Wheeler, J. A. 1957, Annals of Physics, 2, 604

Wise, J. H. & Abel, T. 2008, ApJ, 685, 40

Wise, J. H. & Abel, T. 2011a, MNRAS, 414, 3458

Wise, J. H. & Abel, T. 2011b, MNRAS, 414, 3458

Wise, J. H., Turk, M. J., & Abel, T. 2008, ApJ, 682, 745

Wise, J. H., Turk, M. J., Norman, M. L., & Abel, T. 2012, ApJ, 745, 50

Wolcott-Green, J., Haiman, Z., & Bryan, G. L. 2011, MNRAS, 418, 838

Wyithe, J. S. B. & Loeb, A. 2003, ApJ, 595, 614

Yoshida, N., Abel, T., Hernquist, L., & Sugiyama, N. 2003, ApJ, 592, 645

Yoshida, N., Oh, S. P., Kitayama, T., & Hernquist, L. 2007, ApJ, 663, 687

Yoshida, N., Omukai, K., Hernquist, L., & Abel, T. 2006, ApJ, 652, 6

Zdziarski, A. A., Johnson, W. N., Done, C., Smith, D., & McNaron-Brown, K. 1995, ApJ, 438, L63

Zlosnik, T. G., Ferreira, P. G., & Starkman, G. D. 2007, Phys. Rev. D, 75, 044017

Samenvatting

"Behind it all is surely an idea so simple, so beautiful, that when we grasp it
- in a decade, a century, or a millennium - we will all say to each other,
how could it have been otherwise? How could we have been so stupid?"

John Archibald Wheeler

Astronomie is de oudste wetenschap, het heeft de menselijke nieuwsgierigheid
vanaf het begin gestimuleerd. Alle klassieke culturen, van de Babyloniërs (~ 1600
v.Chr.) tot de Chinese en de oude Grieken, vroegen zich af hoe het Heelal, de
Aarde en de mensen zijn ontstaan. In feite komt het woord Astronomie uit het
oude Grieks en betekent het astron = ster en nomos = wet, de wet van de sterren
dus. In dit proefschrift volgen we de nieuwsgierigheid van onze voorouders en
blijven we vragen stellen met het doel de wetten van de natuur beter te begrijpen.

De overvloed aan structuur die we vandaag de dag over onze nachtelijke hemel
verspreid zien, zoals sterrenstelsels, clusters en vele andere objecten, zijn het ge-
volg van dichtheidsfluctuaties in het zeer jonge heelal. In de huidige literatuur
wordt de theorie die het vormen van structuur in het heelal verklaart de theo-
rie van de 'gravitationele instabiliteit' genoemd. Volgens de gravitationele insta-
biliteit theorie heeft het heelal in het begin kleine dichtheidsfluctuaties die onder
de invloed van de zwaartekracht worden vergroot. Dit betekent dat kleine klonten
als eerste ineenstorten en structuren vormen die vervolgens grotere objecten vor-
men door samensmeltingen en de aanwas van materie. Dit proces wordt hiërar-
chisch structuur vorming genoemd.

Het kosmologische model dat vandaag de dag de observaties van deze struc-
turen het best verklaart is het zo genoemde Lambda Koude Donkere Materie
(ΛKDM) model. Volgens ΛKDM model bestaat het heelal uit 73% Donkere Ener-
gie (DE), 23% donkere materie (DM) en 4% baryonische materie. In dit model
dragen DE+DM 96% bij aan het heelal. Hun eigenschappen moeten echter nog
worden begrepen.

De natuur van DE is een grote uitdaging in kosmologie en is één van de cen-
trale interesses van actief onderzoek. Recente observaties van type Ia supernovas,
die dienen als een meetlat voor afstandsmetingen, tonen aan dat het tempo waar-
mee het heelal uitdijt toeneemt (Amanullah et al. 2010, Perlmutter et al. 1999,

1998, Garnavich et al. 1998, Schmidt et al. 1998, Riess et al. 1998). Dit was een interessant resultaat omdat men verwachtte dat het uitdijingstempo juist zou afnemen door de zwaartekracht. Er wordt gedacht dat deze recentelijke versnelling in de uitdijing van het heelal wordt veroorzaakt door de DE. In hoofdstuk 2 van dit werk bestuderen we de aard van DE. We verkennen de connectie tussen de DE dichtheid en het aantal macroscopische zwarte gaten, voorgesteld door Spaans 1997 (hierna S97). In deze innovatieve theorie word een topologie in Einstein's Algemene Relativiteitstheorie geïntroduceerd zonder de toevoeging van extra vrije parameters. In S97 bestaat het heelal uit een raamwerk van Planck-schaal (10^{-33} cm) drie-tori met macroscopische zwarte gaten daar aan vastgemaakt en het is meervoudig verbonden in de 4-dimensionale tijd-ruimte. Op deze manier worden de globale eigenschappen van het heelal bepaald door lokale.

Volgens de theorie neemt DE de vorm aan van Planck-schaal zwarte gaten die worden geïnduceerd door macroscopische zwarte gaten in elk Planck-volume. Daarom wordt een verandering van het aantal macroscopische zwarte gaten geprojecteerd op de DE dichtheid. Dit houdt in dat wanneer het aantal macroscopische zwarte gaten verdubbelt van $z = 2 - 1$ dat dan de DE dichtheid twee keer hoger zal zijn op $z = 1$ dan op $z = 2$. In ons werk hebben we de type II supernova (SN) dichtheid in een mee-expanderend coördinatenstelsel afgeleid van waargenomen data (Hopkins & Beacom 2006) voor de roodverschuivingen tussen $z = 6 - 0$, waarbij $z = 0$ nu is. Hier zijn type II SNs de dood van zeer massieve sterren met massa's tussen 8–50 zonsmassa's ($M_\odot$). We nemen hierbij aan dat het gros van de macroscopische zwarte gaten worden gevormd door type II SNs. Om de relatieve verandering in het aantal macroscopische zwarte gaten te schatten hebben we de type II SN dichtheid geïntegreerd over de tijd ($z = 6 - 0$) en genormaliseerd met de huidige waarde. In S97 correspondeert deze verandering één op één met de verandering van de DE met de tijd. We vinden dat de DE dichtheid met een factor 5 toeneemt van $z = 3 - 1$. Dit wordt getoond in Figuur 1 waar we de tijdsevolutie van de donkere energie dichtheid plotten (Λ). Deze toename in de DE dichtheid kan de recente versnelling van de uitdijing van het heelal verklaren. Ook wordt de verandering in DE dichtheid minder dramatisch en neemt deze maar met een factor 1.5 toe van $z = 1-0$. Dit is consistent met de waarnemingen waarin de stervorming piekt op $z = 2-3$. Omdat het gros van de macroscopische zwarte gaten wordt gevormd door het type II SNs zien we de meest sterke verandering in de DE dichtheid rond $z = 3-1$. Enige tijd later, wanneer de stervorming afneemt, neemt het aantal zwarte gaten dat wordt gevormd ook af. Daarom zien we nog maar weinig verandering in de DE dichtheid tussen $z = 1-0$. Sterker nog, wanneer een macroscopisch zwart gat eenmaal is gevormd kan het niet meer worden vernietigd. Het kan hooguit samensmelten met een ander zwart gat maar de kans dat dat gebeurt is niet groot. Daarom neemt de DE dichtheid toe of blijft deze gelijk met het verstrijken van de tijd.

De schoonheid van bovenstaande theorie is dat deze gemakkelijk kan worden bevestigd of weerlegd met toekomstige waarnemingen. Op het moment zijn er niet genoeg data waargenomen voor $z > 1$ om een onderscheid te maken tussen
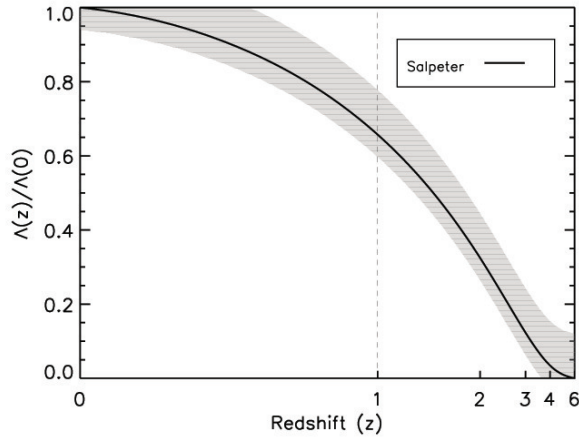
Figure 1 – Roodverschuivingsevolutie van Λ afgeleid van de type II SN dichtheidsdata van Hopkins & Beacom (2006). De schaduw geeft de onzekerheid in het afleiden van de type II SN dichtheid weer.

de verschillende DE scenario's. Echter, in de nabije toekomst zullen nieuwe metingen met hogere precisie en nieuwe waarneemtechnieken hun licht werpen op de natuur van de DE, en dus het heelal.

In hoofdstuk 3 bestuderen we de vorming van de eerste sterren, één van de eerste objecten die vanuit de kleine dichtheidsperturbaties werden gevormd in het vroege universum. Hierbij concentreren we ons op de oorspronkelijke condities waaronder de eerste sterren werden gevormd, hun terugkoppelingseffecten op de omgeving en hoe ze het heelal doen oplichten en aanleiding geven tot een volgende generatie van sterren en objecten in het universum. In ons werk gebruiken we de kosmologische hydrodynamische code Enzo. Kosmologische simulaties, gebaseerd op het ΛKDM model van hiërarchisch structuurvorming, voorspellen dat de eerste sterren ($30-300\,M_\odot$) op roodverschuivingen $z \sim 20-30$ zijn gevormd in donkere materie halo's met een massa van $10^6\,M_\odot$ (Tegmark et al. 1997, Abel et al. 2002, Bromm et al. 2002, Yoshida et al. 2003, O'Shea & Norman 2007).

Of een ster vormt of niet hangt af van het vermogen van het interstellaire gas om te koelen en dichte moleculaire wolken te vormen. De effectiviteit van stralingskoeling wordt bepaald door de dichtheid en de chemische samenstelling van het gas. Theoretisch gezien is de natuurkunde van de eerste sterren relatief simpel in vergelijking met hedendaagse stervorming. Het oergas in het vroege universum was zonder metalen. Bij conventie noemen astronomen alle elementen zwaarder dan Helium een metaal. Ook waren er geen magnetische velden die de structuurvorming konden beïnvloeden. Bovendien waren er ook geen stofdeeltjes die de straling, uitgeproduceerd door de proto-ster of winden van andere sterren,

aan het gas konden koppelen. Daarom hing de koeling voornamelijk af van de abondanties van atomair en moleculair waterstof en deuterium (HD). Neutraal atomair waterstof (H I) is de belangrijkste koeler voor temperaturen $T \geq 10^4$ K en moleculair waterstof (H_2) domineert de koeling in een gas zonder metalen voor $200 < T < 10^4$ (Saslaw & Zipoy 1967, Peebles 1969).

Men kan de massa van de sterren schatten door middel van het Jeans massa (M_J) criterium. De Jeans massa geeft een maximale waarde voor een wolk die in evenwicht kan zijn en deze massa schaalt met de temperatuur van het omringende gas als $M_J \propto T^{3/2}$. Door waarnemingen van het nabije heelal weten we dat de huidige stellaire massa schaal $\sim 1\ M_\odot$ is. Echter, door het gebrek aan metalen in het vroege heelal waren de temperaturen in de stervormingsgebieden toen veel hoger ($T \sim 100 - 300$ K) in vergelijking met het lokale heelal ($T \sim 10$ K). Zoals men kan zien volgens het M_J criterium waren daarom de eerste sterren veel massiever ($M \sim 100\ M_\odot$). De eerste sterren staan ook bekend als Populatie III (Pop III) sterren. In de literatuur zijn er twee type Pop III sterren gedefinieerd: Pop III.1 zijn de allereerste sterren die zijn gevormd uit het oergas en Pop III.2 sterren zijn de sterren die zijn gevormd in een metaal-arm gas maar onder invloed van de straling van een eerdere generatie sterren. De levensduur van de eerste sterren is erg kort omdat ze zo massief zijn. Aan het einde van hun leven eindigen ze of als SN of ze storten ineen tot een zwart gat. In het geval van SNs verrijken ze hun omgeving met de metalen die nucleaire reacties in het binnenste van sterren produceren. De initiële massa functie (IMF) van Pop III en Pop II sterren (sterren die zijn gevormd uit een gas dat is verrijkt met metalen) is niet goed bekend omdat er een gebrek aan waarnemingen is.

Middels simulaties van het ontstaan van de eerste sterren is het aangetoond dat door het gebrekkige vermogen van een metaal-vrij gas om te koelen de IMF van de eerste sterren een aantal orders van grootte meer massieve sterren bevat dan de huidige IMF, zoals hierboven uitgelegd. De overgang van een zware IMF voor de eerste sterren naar een lichtere IMF is dus belangrijk om te begrijpen. Om de onderliggende natuurkunde van deze overgang te bestuderen hebben we een aantal simulaties uitgevoerd met abondanties van 10^{-4}, 10^{-3}, 10^{-2}, and $10^{-1}\ Z_\odot$ en een ultraviolet (UV) achtergrond stralingsveld van $G_0 = 10^{-1}$ and 10^{-2}. We zien dat de roodverschuiving waarop een meer-fase interstellair medium (ISM) wordt gevormd, waarin heet ijl en koud dicht gas naast elkaar bestaan, afhangt van de abondantie. Als UV straling afwezig is dan is deze kritieke abondantie consistent met Bromm & Loeb (2003b) en Smith & Sigurdsson (2007), en is $(Z/Z_\odot)_{crit} \sim 10^{-3.5}$. Echter de koude dichte fase is gevoelig voor de UV straling voor abondanties $Z/Z_\odot \leq 10^{-3}$ en robuust voor abondanties $Z/Z_\odot \geq 10^{-2}$. Dit word getoond in Figuur 2 waarin we de intensiteit van het stralingsveld tegen de roodverschuiving plotten voor de verschillende stralingsvelden en abondanties. De symbolen markeren de roodverschuivingen waarop een koude dichte gasfase, waaruit de sterren ontstaan, wordt gevormd. Dus het metaal-arme stervormende ISM is fragiel onder de invloed van UV straling en de toevoeging van een constant achtergrond stralingsveld verhoogd de kritische abondantie waarbij de Pop III–Pop II transitie
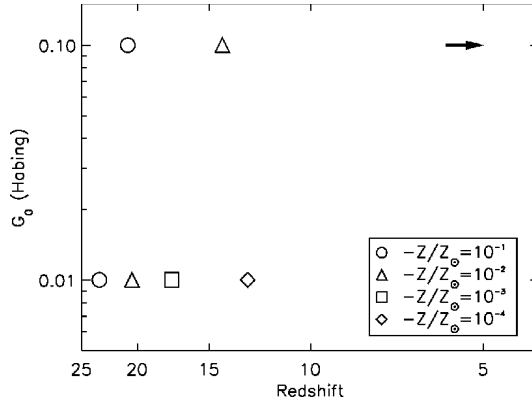
Figure 2 – Intensiteit van het stralingsveld. Symbolen markeren de roodverschuivingen waar een koude dichte gas fase is gevormd. De pijl vertegenwoordigt de runs met $Z/Z_\odot=10^{-3}$ en $Z/Z_\odot=10^{-4}$, voor een stralingsveld van $G_0=10^{-1}$.

plaatsvindt van $Z_{cr} \sim 10^{-3.5} Z_\odot$ naar $Z_{cr} \sim 10^{-2} Z_\odot$ wanneer $F_0 > 10^{-5}$ erg s^{-1} cm^{-2}. Dit is in goede overeenstemming met de waardes die worden gevonden voor de onderdrukking van H$_2$ door Shang et al. (2010). Bovendien neemt de koelingseffectiviteit van het aanwezige gas niet meer toe voor een abondantie die hoger is dan 1% die van de zon, en de Jeans massa's in halo's die reeds zijn verrijkt tot abondanties van $Z/Z_\odot = 10^{-2}$ en $Z/Z_\odot = 10^{-1}$ zijn dus vergelijkbaar.

In de literatuur zijn de eerste sterrenstelsels gedefinieerd als de halo's die zelf-regulerende stervorming in een meer-fase ISM kunnen ondersteunen en hierbij het door straling verwarmde gas kunnen behouden (Dijkstra et al. 2004a, Mac Low & Ferrara 1999, Madau et al. 2001, Oh & Haiman 2002, Scannapieco et al. 2002, Wada & Venkatesan 2003). Waarnemingen van quasars op hoge roodverschuiving (z > 6) impliceren dat deze worden aangedreven door supermassieve zwarte gaten (SMZG) met massa's rond de 10^9 M$_\odot$ (Fan et al. 2003, 2006a, Kurk et al. 2007). Men denkt dat deze SMZG worden gevormd (in minder dan 1 miljard jaar) door de aanwas van gas op kiem zwarte gaten met massa's tussen de $10^2 - 10^5$ M$_\odot$. Echter, de oorsprong van deze kiem zwarte gaten is nog een open vraag. Vandaag de dag denkt men dat de meeste sterrenstelsels een SMZG herbergen in hun centrum. Bovendien tonen dynamische studies van de centrale zwarte gaten in nabije sterrenstelsels aan dat er een sterke correlatie is tussen de massa van het zwarte gat (M$_{BH}$) en de massa van de bult (de centrale bolvormige verdeling van sterren, M$_B$) van een sterrenstelsel ($\frac{M_{BH}}{M_B} \sim 10^{-3}$), de zogeheten Magorrian relatie. Echter, de onderliggende fysica van deze relatie is nog niet goed begrepen.

In hoofdstuk 4 & 5 van dit proefschrift bekijken we de volgende vragen: Hoe verandert het tempo van aanwas van deze centrale zwarte gaten door de tijd heen? Wat zijn de effecten van X-ray bestraling door actieve kernen (AK) op het omringende gas? Hoe veranderen de relatieve bijdragen van AK en supernova feedback

door de tijd heen? Om deze vragen te beantwoorden hebben we kosmologische simulaties gedaan met de Enzo code. In deze code hebben we de X-ray chemie gebied (XDR) code van Meijerink & Spaans (2005) geïmplementeerd. We gebruiken de stralingstransport module *Moray* om het stralingstransport voor een polychromatisch spectrum te berekenen. In de omgeving van een zwart gat is de implementatie van de X-rays het belangrijkste punt. Omdat de aanwas van gas op het centrale zwarte gat een heldere bron van X-ray, UV en optische fotonen veroorzaakt. Hier drijven de UV en X-ray straling de chemische samenstelling van het aanwassende en stervormende gas en ze beïnvloeden de thermodynamica van het ISM. Slechts 10% van de straling van het centrale zwarte gat wordt uitgestraald in de vorm van X-rays. Echter, omdat de X-rays niet erg sterk interageren met materie (men noemt dit een kleine interactie-doorsnede) dringen ze veel dieper in het medium door en dus beïnvloeden ze het omringende gas op grotere straal dan de UV fotonen. In ons werk worden voor de eerste keer de interacties tussen de X-rays en metalen meegenomen in de berekeningen.

Als een bewijs van concept, om te begrijpen wat de X-rays met het omringende gas doen, hebben we twee simulaties gedaan. In die simulaties plaatsen we een zwart gat in het centrum van onze halo met een massa van 5×10^4 M$_\odot$ op z=15. Het verschil tussen de twee runs was uitsluitend de abondantie van het omringende gas waarbij we in de ene run een gas met een metaal abondantie van 0 hebben (hierna XDR$_Z$) en in de andere run een abondantie gelijk aan die van de zon (hierna XDR$_S$). We zien dat in de XDR$_Z$ run de X-rays een H II gebied vormen. Dit komt omdat de X-rays een kleine interactie-doorsnede hebben met gas zonder metalen en dus dringen ze diep door in het medium en deponeren ze hun energie op grote afstand. Bovendien veegt dit door de X-rays veroorzaakte H II gebied, dat een snelheid heeft van enkele 100 km s^{-1}, het gas uit het centrale deel en verhindert het de aanwas van materie op het centrale zwarte gat. Echter in de XDR$_S$ run zien we dat in het begin er geen H II gebied vormt. Dit komt omdat de X-rays op kleinere afstand worden geabsorbeerd door het met metalen verrijkte gas, en dus deponeren ze hun energie uitsluitend lokaal. Daarom is er nog steeds veel materiaal dat kan zorgen voor de groei van het centrale zwarte gat. Dit wordt getoond in figuur 3 waar we dichtheid-temperatuur fase diagrammen tonen van de XDR$_S$ (links) en XDR$_Z$ (rechts) runs, ongeveer 12 miljoen jaar nadat we het zwarte gat hebben toegevoegd.

In hoofdstuk 5 onderzoeken we de mogelijke voorlopers van de SMZGs die we zien op z ~ 6. In de literatuur zijn er 2 mogelijke scenario's: a) Stellaire kiem zwarte gaten: de overblijfselen van de zeer massieve eerste sterren met massa's van 10^{2-4} M$_\odot$, b) Singuliere ineenstorting: waarbij een atomair koelende halo direct ineenstort en een 10^{4-6} M$_\odot$ zwart gat vormt. In ons werk simuleren we het laatste scenario. Om een zwart gat te vormen door middel van singuliere ineenstorting van een atomaire halo moet de vorming van H$_2$ worden onderdrukt zodat fragmentatie wordt voorkomen. We doen twee simulaties en in deze simulaties zetten we de recepten voor de vorming van Pop III en Pop II/I sterren aan en nemen we hun feedback effecten mee in de berekeningen. Het enige verschil tussen
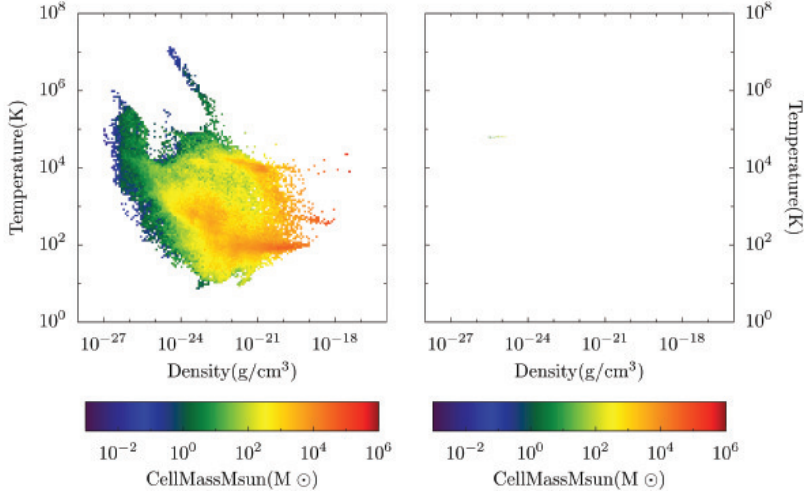
Figure 3 – Dichtheid-temperatuur fase diagrammen voor een bol van 200 pc diameter voor de XDR_S (links) en XDR_Z (rechts) runs op z = 14.54, 12 miljoen jaar nadat we het zwarte gat hebben toegevoegd.

de twee simulaties is dat we in de één een UV achtergrond stralingsveld van 10^3 J_{21} (hierna BG_3) hebben en in de andere 10^5 J_{21} (hierna BG_5), met $J_{21} = 10^{-21}$ erg s^{-1} cm^{-2} sr^{-1} Hz^{-1}. We zetten het Lyman-Werner (LW, E = 11.2–13.6 eV) achtergrond stralingsveld aan op z = 30. Recent werk door Wolcott-Green et al. (2011) heeft aangetoond dat zulke J_{LW} waarden genoeg zijn om onze halo H_2 vrij te houden. Op z = 15 voegen we ons zwarte gat met een massa van 5×10^4 $M_\odot$ toe. We zien dat in het geval van BG_5 de sterke UV achtergrondstraling H_2 effectiever foto-dissocieert dan in het BG_3 geval. Daarom is in de BG_5 run de H_2 fractie in de centrale 100 pc zo laag als $\sim 10^{-8}$ terwijl in de BG_3 run deze 10^{-6} is. Bovendien vormen er in de BG_5 run geen Pop III sterren tot op zijn minst z = 11. Echter, in het geval van BG_3 vormen de eerste Pop III sterren onmiddellijk nadat we het massieve zwarte gat (MZG) toevoegen (0.265 Myr later). Dit komt doordat voor z = 15 de H_2 abondantie al $\sim$ 2 ordes van grootte hoger was dan in het BG_5 geval. Bovendien stimuleert de X-ray ionisatie de vorming van H_2 via de H^- route, en in ongeveer 0.3 Myr heeft de H_2 abondantie een waarde bereikt waarbij het voldoet aan ons criterium voor Pop III vorming van 5×10^{-4}. Dit wordt getoond in figuur 4 waar we het 2D profiel van de H_2 abondantie tegen de straal plotten voor de BG_5 (boven) en BG_3 (onder) gevallen op z = 14.95 (links), 14.86 (midden), 14.78 (rechts). De horizontale continue lijn in elke plot vertegenwoordigt de H_2 fractie drempel voor Pop III ster formatie.

We zien dat X-ray feedback en de groei van zwarte gaten zelfregulerend is. Wanneer het centrale zwarte gat aanwast versterkt het de X-ray straling. Dit onder-drukt vervolgens de aanwas van materie op het zwarte gat en daarom verzwakt
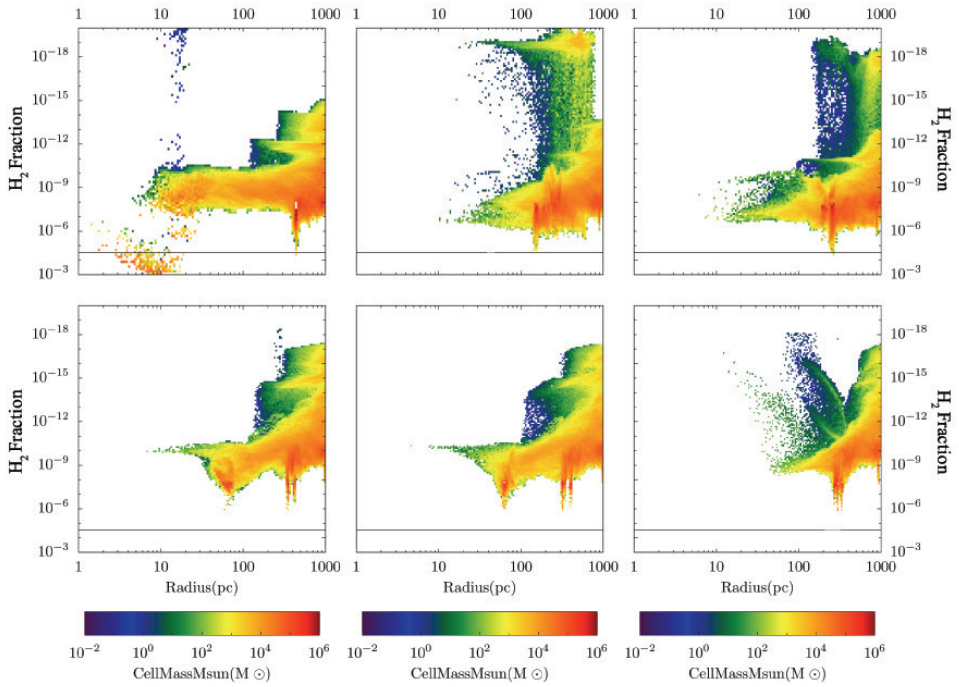
Figure 4 – 2D profiel van de H$_2$ abondantie tegen straal voor de BG$_5$ (boven) en BG$_3$ (onder) gevallen op z = 14.95 (links), 14.86 (midden), 14.78 (rechts).
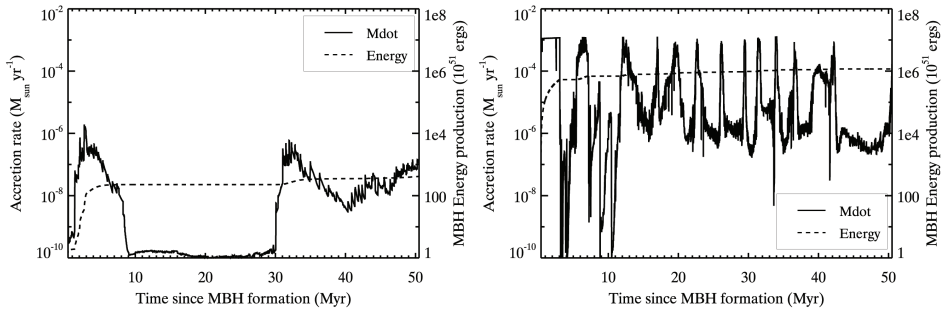
Figure 5 – Aanwas en de overeenkomstige totale energieproductie van het centrale zwarte gat tegen de tijd wordt geplot voor de BG$_5$ (links) en BG$_3$ (rechts) runs.

de X-ray straling. Dan kan er weer meer materie op het zwarte gat vallen en dus neemt de X-ray straling weer toe. Bovendien is in het geval van BG$_5$ de aanwas $\sim 10^{-6}$ M$_\odot$ yr^{-1} 2 Myr nadat we de MZG toevoegen in het centrum van de halo. Dit komt overeen met een totale energieproductie van 2×10^{53} erg over 1 Myr voor een efficiëntie van 10% Eddington; dit is ongeveer hetzelfde als de energie die wordt geproduceerd door 200 SNs. Dit wordt getoond in figuur 5 waar de aanwas en de overeenkomstige totale energieproductie van het centrale zwarte gat tegen de tijd wordt geplot voor de BG$_5$ (links) en BG$_3$ (rechts) runs. Wanneer de eerste SN afgaat in de BG$_3$ run, wordt het medium verrijkt met metalen. Deze verrijking met metalen versterkt de instroom van materie naar het centrale zwarte gat door het gas efficiënt te koelen. Daarom is de aanwas na 1 Myr 10^{-3} M$_\odot$ yr^{-1} in de BG$_3$ run, wat ongeveer 3 orders van grootte meer is dan in het BG$_5$ geval, zie figuur 5. De BG$_5$ run blijft vrij van metalen en dus is de reactietijd van het aanwezige gas op de X-ray feedback langer dan in de BG$_3$ run. De groei van het zwarte gat wordt dus voldoende onderdrukt door de X-ray feedback. Daarom lijkt het onwaarschijnlijk dat het gros van de SMZG op $z \sim 6$ is gevormd door de directe ineenstorting van een atomaire halo met een massa van 10^8 M$_\odot$ onder de invloed van een sterk UV achtergrond stralingsveld van 10^5 J$_{21}$. Anderzijds, in het geval van de BG$_3$ run is de groei van het centrale zwarte gat veel sneller. Dit kan men zien in figuur 6 waar we de groei van het zwarte gat tegen de tijd plotten. Daarom concluderen we dat centrale zwarte gaten in een milder UV achtergrond stralingsveld waarschijnlijke kandidaten zijn voor de z = 6 SMZG.

In dit proefschrift maken we een grote stap voorwaarts om de aard van het heelal en de wegen die naar de vorming van SMZG leiden te begrijpen. Er zijn echter nog vele open vragen: Is het mogelijk om deze SMZG van stellaire kiem zwarte gaten te maken? Hoe veelvoorkomend zijn deze singuliere ineenstortingen tot zwarte gaten? Hoe veranderen de relatieve contributies van AK en SN feedback op het gastheer sterrenstelsel door de tijd heen? Wat drijft de Magorrian relatie? We beogen om in de nabije toekomst simulaties te doen met daarin stellaire
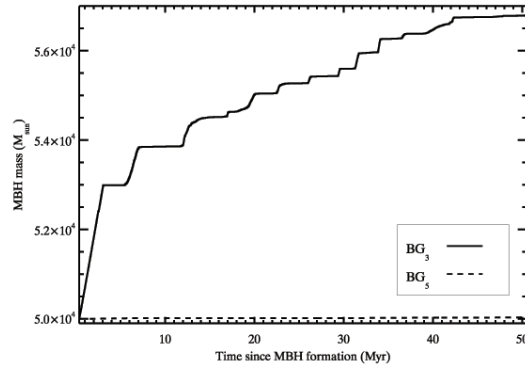
Figure 6 – Groei van het centrale zwarte gat voor de BG_5 (gestreepte lijn) en BG_3 (continue lijn) runs.

kiem zwarte gaten en X-ray feedback effecten. Bovendien kan men, om uit te vinden hoe vaak singuliere ineenstortingen tot zwarte gaten voorkomen, simulaties doen met een groter volume (100 Mpc/h) met een resolutie hoog genoeg om de X-ray fysica te onderscheiden. Ook zouden we deze simulaties moeten laten lopen tot z = 2–3 zodat we de onderliggende fysica van de Magorrrian relatie en het samenspel tussen AK en SN feedback kunnen bestuderen. In de volgende decennia, met nieuwe waarneemtechnieken en instrumenten en toenemende rekenkracht, krijgen we de kans om een glimp op te vangen van de eerste momenten van het heelal en dit zal meer licht werpen op haar aard. Dit maakt het mogelijk voor ons om de bestaande theoriën en ons huidige begrip van het heelal te testen. Zoals sir Eddington al zei: "We should be unwise to trust scientific inference very far when it becomes divorced from opportunity for observational test". Oftewel, "Het zou onverstandig zijn om wetenschappelijke gevolgtrekking erg te vertrouwen als deze te ver wordt gescheiden van de mogelijkheid om haar met waarnemingen te toetsen".

Summary

"Behind it all is surely an idea so simple, so beautiful, that when we grasp it - in a decade, a century, or a millennium - we will all say to each other, how could it have been otherwise? How could we have been so stupid?"

John Archibald Wheeler

Astronomy is the oldest science, it has incited human curiosity from the beginning. All the ancient cultures, from the Babylonians (~ 1600 B.C.) to the Chinese and Greeks, were questioning how the universe, the earth and humans came into existence. In fact, the word 'Astronomy' comes from Greek and means astron = star and nomos = law, so law of the stars. In this thesis, we follow the curiosity of our ancestors and continue asking questions in order to better our understanding of the laws of nature.

The wealth of structures we observe today, such as galaxies, clusters and many other objects which are spread over our night sky, are the result of primordial density fluctuations. In the current literature, the theory that explains the formation of structure in the universe is called the 'gravitational instability theory'. According to the gravitational instability theory the universe has small fluctuations in the beginning and these density fluctuations are amplified under the influence of gravity. This means that small clumps are the first to collapse and form structures and then they build up larger structures by mergers and the accretion of matter. This process is called hierarchical structure formation.

The cosmological model that currently matches the observations of those structures best is the so called Lambda Cold Dark Matter (ΛCDM) model. According to the ΛCDM model the universe consists of 73% dark energy (DE), 23% dark matter (DM), and 4% baryonic matter. In this model, DE+DM contribute to 96% of the universe. However, their nature is still to be understood.

The nature of DE is a major challenge in cosmology and is one of the central interest of active research. Recent observations of type Ia supernovae, which serve as rulers for distance measurements, have shown that the rate of the cosmic expansion of the universe is accelerating (Amanullah et al. 2010, Perlmutter et al. 1999, 1998, Garnavich et al. 1998, Schmidt et al. 1998, Riess et al. 1998). This was an interesting result, because the growth rate of the universe was expected

to slow down due to the gravitational attraction. This recent-time acceleration in the expansion of the universe is thought to be caused by DE. In chapter 2 of this work, we study the nature of DE. We explored the connection between the DE density and number of macroscopic black holes, proposed by Spaans (1997) (hereafter S97). In this novel theory, a topology is introduced to Einstein's theory of GR without the addition of any free parameters. In S97, the universe is made up of a lattice of Planck scale three-tori with macroscopic black holes attached to it, and is multiply-connected in 4 dimensional space-time. This way, the global properties of the universe determine local ones.

According to the theory, DE takes the form of Planckian black holes that are induced by macroscopic black holes in every Planckian volume. Therefore, the change in the number of macroscopic black holes with time is projected onto the DE density such that, if the number of macroscopic black holes doubles from $z = 2 - 1$ then the DE density will be twice higher at $z = 1$ than $z = 2$. In our work, we used the co-moving type II supernova (SN) rate density derived from the observational data (Hopkins & Beacom 2006) for redshifts between $z = 6 - 0$, where $z = 0$ corresponds to now. Here, type II SN are the death of a very massive stars with masses between 8–50 solar masses ($M_\odot$). In this, we assume that the bulk of the macroscopic black holes are formed from the type II SNe. We integrated the type II SN rate density over time ($z = 6 - 0$) and normalized it to todays value in order to estimate the relative change in the number of macroscopic black holes. In S97, this change corresponds directly to the change of the DE density with time. We find that, the DE density increases by a factor of 5 from z=3-1. This is shown in Figure 1, where we plot the time evolution of dark energy density (Λ). Hence, this boost to the DE density density can explain the recent-time acceleration of the universe. Furthermore, the change in DE density becomes less dramatic and increases only by a factor of 1.5 from $z = 1 - 0$. This is consistent with observational data where the star formation rate peaks at $z = 2 - 3$. Because, the bulk of the macroscopic black holes are formed by type II SNe, we see the most violent change in DE density around $z = 3 - 1$. Later on when the star formation rate goes down, so does the number of black holes that are formed. Therefore, we do not see much change in the DE density between $z = 1 - 0$. Moreover, when a macroscopic black hole is formed it cannot be destroyed. It can only merge with another black hole but the probability of such an event is not so high. Hence, the DE density of the universe either increases with time or stays the same.

The beauty of the above theory is that it can easily be confirmed or disproved with upcoming observations. At the moment, there is not enough observational data for $z > 1$ in order to distinguish between possible DE scenarios. However, in the near future new higher precision measurements and new observational techniques will shed light on the nature of DE, hence the universe.

In chapter 3, we study the formation of the first stars, one of the first objects that is formed through the small density perturbations in the early universe. In this, we focus on the initial conditions in which the firsts stars are formed, their feedback effects on to surroundings, and how they enlighten the universe and give birth to
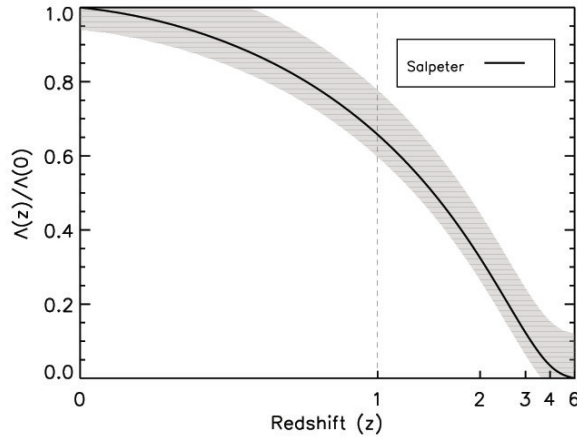
Figure 1 – Redshift evolution of Λ derived from the type II SN rate data of Hopkins & Beacom (2006). The shading represents the observational uncertainty in deriving the type II SN rate.

further generations of stars and objects in the universe. In our work, we use the cosmological, hydrodynamical simulation code Enzo. Cosmological simulations, based on the ΛCDM model of hierarchical structure formation, predict that the first stars ($30 - 300$ M$_\odot$) have formed at redshifts $z \sim 20 - 30$, in dark matter halos with masses of 10^6 M$_\odot$ (Tegmark et al. 1997, Abel et al. 2002, Bromm et al. 2002, Yoshida et al. 2003, O'Shea & Norman 2007).

The formation of a star depends on the ability of interstellar gas to cool and form dense molecular clouds. And the efficiency of radiative cooling is determined by the density and the chemical composition of the gas. Theoretically, the physics of the first stars is rather simple compared to the physics of present day star formation. The primordial gas in the early universe was metal free. Here, astronomers call metals all the elements heavier than He, and there were no magnetic fields that could affect the formation of structure. Moreover, there were no dust grains to couple the gas to radiation emitted by the protostar or winds from other stars. Therefore, cooling depends mostly on the abundances of atomic and molecular H, and deuterium, HD. Neutral atomic hydrogen, H I, is the major coolant for temperatures $T \geq 10^4$ K, and molecular hydrogen, H_2, dominates cooling in a metal free gas for $200 < T < 10^4$ (Saslaw & Zipoy 1967, Peebles 1969).

One can estimate the mass of the stars from the Jeans mass (M_J) criterion. The Jeans mass gives a maximum mass value for a cloud that can be in an equilibrium and it scales with the temperature of the ambient gas as $M_J \propto T^{3/2}$. From observations of the nearby universe we know that the present day stellar mass scale is 1 M$_\odot$. However, because of the lack of metals in the early universe, temperatures

127

of the star forming regions were much higher (T $\sim$ 100 – 300 K) compared to the local universe (T $\sim$ 10 K). Hence, as one can see from the M_J criterion the first stars were much more massive (M $\sim$ 100 $M_\odot$). The first stars are also known as Population III (Pop III) stars. There are two types of Pop III stars defined in the literature: Pop III.1, corresponds to the first stars that are ever formed from the primordial gas and Pop III.2, the stars that are formed from metal-poor gas but under influence of the radiation from a previous generation of stars. The lifetimes of the first stars are very short due to their high masses. And they end their lifes either as supernova explosions or they collapse into a black hole. In the case of SNe, they enrich their surroundings by the metals that are produced in the core of stars through the nuclear reactions. The initial mass function (IMF) of Pop III stars and Pop II stars (stars that are formed from metal enriched ambient gas) is poorly known due to a lack of observations.

In simulations of the formation of the first stars, it has been shown that, due to the limited ability of metal-free primordial gas to cool, the IMF of the first stars is a few orders of magnitude more massive than the current IMF, as explained above. The transition from a high-mass IMF of the first stars to a lower-mass current IMF is thus important to understand. To study the underlying physics of this transition, we performed several simulations for metallicities of 10^{-4}, 10^{-3}, 10^{-2}, and 10^{-1} $Z_\odot$ and ultraviolet (UV) background radiation fields of $G_0 = 10^{-1}$ and 10^{-2}. We find that the redshift at which a multi-phase interstellar medium (ISM) is established, where hot-diffuse and cold-dense gas co-exists, depends on metallicity. In the absence of UV radiation, this critical metallicity is consistent with Bromm & Loeb (2003b) and Smith & Sigurdsson (2007), and is $(Z/Z_\odot)_{crit} \sim 10^{-3.5}$. However, the cold dense gas phase is fragile to UV radiation for metallicities of $Z/Z_\odot \leq 10^{-3}$ and robust to UV radiation for metallicities of $Z/Z_\odot \geq 10^{-2}$. This is shown in Figure 2, where we plot radiation field strength versus redshift for different metallicity and UV background radiation field. Symbols mark the redshifts to show when a cold dense gas phase is formed, from which new stars will form. Thus, the metal-poor star-forming ISM is fragile to UV radiation, and inclusion of a constant radiation background raises the critical metallicity value for the Pop III–Pop II transition from $Z_{cr} \sim 10^{-3.5}$ $Z_\odot$ to $Z_{cr} \sim 10^{-2}$ $Z_\odot$ when $F_0 > 10^{-5}$ erg s^{-1} cm^{-2}. This is in good agreement with the values that are found for the suppression of H_2 by Shang et al. (2010). Furthermore, above a metallicity of 1% solar the cooling efficiency of ambient gas no longer increases with a rise in metallicity (Spaans & Meijerink 2008), and therefore the Jeans masses in halos that are pre-enriched to metallicities of $Z/Z_\odot = 10^{-2}$ and $Z/Z_\odot = 10^{-1}$ are comparable.

In the literature, the first galaxies are defined as the halos that can maintain self-regulated star formation in a multi-phase ISM and retain gas photoheated by the first stars (Dijkstra et al. 2004a, Mac Low & Ferrara 1999, Madau et al. 2001, Oh & Haiman 2002, Scannapieco et al. 2002, Wada & Venkatesan 2003). Observations of high redshift (z > 6) quasars suggest that they are powered by SMBHs with masses on the order of 10^9 $M_\odot$ (Fan et al. 2003, 2006a, Kurk et al. 2007). These SMBHs are thought to be formed (in less than 1 billion years) through the accretion
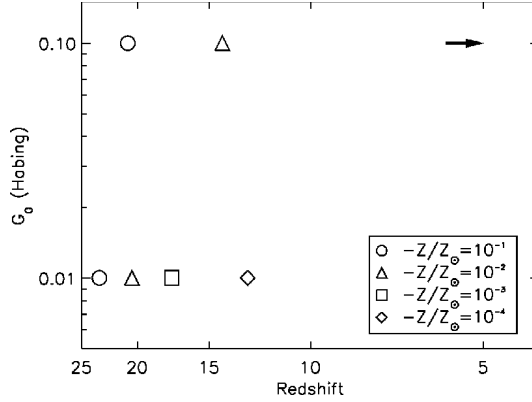
Figure 2 – Radiation field strength vs. redshift. Symbols mark the redshifts where a cold dense gas phase is established. The arrow represents the runs with $Z/Z_\odot=10^{-3}$ and $Z/Z_\odot=10^{-4}$, for a radiation field of $G_0 = 10^{-1}$, which do not develop a cold dense gas phase before z = 5.

of gas onto seed black holes of masses between $10^2 - 10^5\ M_\odot$. However, the origin of these seed black holes is still an open question. Most galaxies today are believed to host supermassive black holes (SMBHs) in their centers. Moreover, dynamical studies of the central black holes of galaxies in the local universe have shown that there is a tight correlation between black hole mass (M_{BH}) and the bulge mass (M_B) of a galaxy ($\frac{M_{BH}}{M_B} \sim 10^{-3}$), the so called Magorrian relation. However, the underlying physics of this relation is not well understood.

In chapters 4 & 5 of this thesis, we address the following questions: How does the accretion rate of these central black holes evolve through cosmic time? What are the effects of X-ray irradiation from active galactic nuclei (AGN) on the ambient gas? How do the relative contributions of AGN and supernova feedback on the host galaxy evolve through time? In order to answer these questions we perform cosmological simulations by using the Enzo code in which we implemented the X-ray dominated region (XDR) code of Meijerink & Spaans (2005). And we use the radiation transport module *Moray* to calculate the radiative transfer for a polychromatic spectrum. Here, the implementation of X-rays are the key point. Because the accretion of gas onto the central black hole yields a luminous source of X-ray, UV, and optical photons. In this, UV and X-ray radiation drive the chemistry of the accreting and star-forming gas, and affect the thermodynamics of the ISM. Here, only 10% of the radiation from the central black hole is emitted in X-rays however, because X-rays have smaller cross-sections they penetrate further into the medium and influence the ambient gas at larger radii than UV photons. In our work, for the first time, the interactions of X-rays with the metals are taken into account.

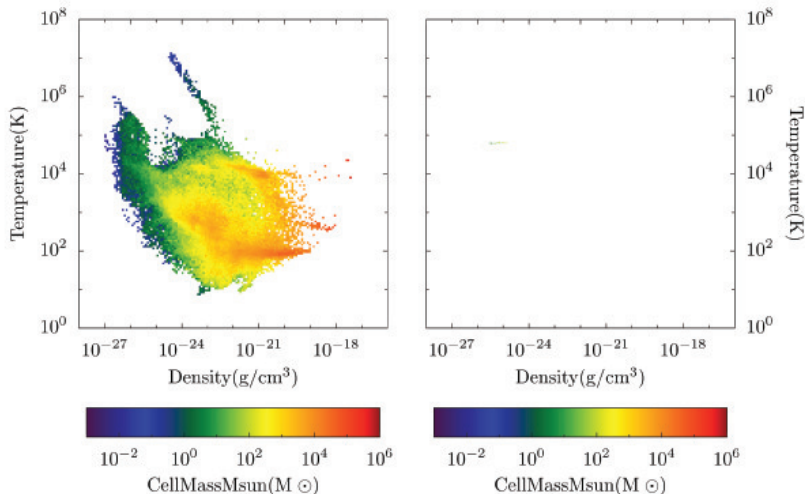As a proof of concept, to understand what X-rays do to the ambient gas, we

Figure 3 – Density-temperature phase diagrams within a sphere of 200 pc diameter for the XDR$_S$ (left) and XDR$_Z$ (right) cases at z = 14.54, 12 million years after we insert the black hole.

perform two simulations. In those simulations, we inserted a black hole into the center of our halo with a mass of 5×10^4 M$_\odot$ at z = 15. The differences in between the two runs was only the metallicity of the ambient gas where in one run we have a zero metallicity gas (hereafter XDR$_Z$) and in the other run we have solar metallicity gas (hereafter XDR$_S$). We find that, in the XDR$_Z$ run, an X-ray induced H II region is formed. This is because the X-rays have small cross-scetions with a zero metallicity gas, hence penetrates further into the medium and deposit its energy at larger radii. Furthermore, this X-ray induced H II region, which has a velocity of a few 100 km/s, sweeps out the gas from the central region and hence quenches the accretion of matter onto the black hole. However, in the XDR$_S$ run, we see that in the beginning there is no H II region formed. This is because, X-rays are attenuated by the metal enriched gas at smaller radii, and so they deposit their energy only locally. Therefore, there is still a lot of matter for the central black hole to accrete and grow. This is shown in Figure 3, where we plot the density-temperature phase diagrams of the XDR$_S$ (left) and XDR$_Z$ (right) runs, roughly 12 million years after we insert the black hole.

In chapter 5, we investigate the possible hosts of the SMBHs that we see at z ~ 6. In the literature there are two plausible scenarios: a) Stellar seed black holes: remnants of the very massive first stars with masses of 10^{2-4} M$_\odot$, b) Singular collapse: where an atomic cooling halo directly collapses and forms a 10^{4-6} M$_\odot$ black hole. In our work, we simulate the later scenario. In order to form a black hole through singular collapse of an atomic halo one needs to suppress the formation of H$_2$ and hence the fragmentation. We perform two simulations and

in these simulations we turn on the star formation recipes for Pop III and Pop II/I stars and take into account their feedback effects. The only difference between the two runs is that one has a UV background radiation of 10^3 J_{21} (hereafter BG_3) and another one has 10^5 J_{21} (hereafter BG_5), where $J_{21} = 10^{-21}$ erg s^{-1} cm^{-2} sr^{-1} Hz^{-1}. We turn on the Lyman-Werner (LW, E = 11.2-13.6 eV) background radiation field at z = 30. Recent work by Wolcott-Green et al. (2011) has shown that such J_{LW} values are sufficient to keep our halo almost H_2 free. At z=15, we insert our black hole with a mass of 5×10^4 M$_\odot$. We find that in the BG_5 case the strong UV background photo-dissociates H_2 more efficiently than in the BG_3 case. Therefore, in the BG_5 run the H_2 fraction in the central 100 pc is as low as $\sim 10^{-8}$, whereas in the BG_3 run it is 10^{-6}. Furthermore, in the BG_5 case no Pop III stars are formed until at least $z = 11$. On the other hand, in the BG_3 case, right after we insert the MBH (0.265 Myr later), the first Pop III stars form. This is because prior to $z = 15$ the H_2 abundance in the BG_3 case was already ~ 2 orders of magnitude higher than in the BG_5 case. Moreover, X-ray ionization drives the formation of H_2 through the H$^-$ route, and in about 0.3 Myr it has reached a value where it meets our Pop III formation criterion of 5×10^{-4}. This can be seen in Figure 4, where we plot 2D profile of H_2 fraction with respect to radius for the BG_5 (top) and BG_3 (bottom) cases at z = 14.95 (left), 14.86 (middle), 14.78 (right). The horizontal solid line in each plot represents the H_2 fraction threshold for Pop III star formation.

We also find that X-ray feedback and black hole growth are self-regulating. When the central black hole accretes matter it enhances X-ray radiation. This in return quenches further accretion of matter onto the black hole and hence, X-ray radiation weakens. Then, matter starts falling onto the black hole again and X-ray feedback is strengthened. Furthermore, 2 Myr after we insert the MBH into the center of our halo, the accretion rate in the BG_5 case is $\sim 10^{-6}$ M$_\odot$ yr^{-1}. This corresponds to a total energy production of 2×10^{53} erg over 1 Myr for an efficiency of 10% Eddington, which is about the same as the energy produced by 200 SNe. This is shown in Figure 5, where we plot accretion rate and the corresponding total energy production of the central black hole over time for the BG_5 (left) and BG_3 (right) runs. Furthermore, when the first SNe goes off in the BG_3 case, the medium is enriched by the metals. This metal enrichment enhances the inflow of matter onto the central black hole by cooling the gas efficiently. Hence, the accretion rate in the BG_3 run after 1 Myr is 10^{-3} M$_\odot$ yr^{-1}, which is 3 orders of magnitude higher than in the BG_5 case, see Figure 5. The BG_5 run stays metal-free and hence, the response time of ambient gas to X-ray feedback is longer than in the BG_3 case. Thus, the growth of the black hole is sufficiently suppressed by the X-ray feedback. Therefore, it seems unlikely that the bulk of the SMBHs at $z \sim 6$ is formed through the direct collapse of an 10^8 M$_\odot$ atomic halo under the influence of a strong 10^5 J_{21} UV background radiation field. On the other hand, in the BG_3 case the growth of the central black hole is more rapid. This is seen in Figure 6, where we plot the black hole growth versus time. Therefore, we conclude that central black holes in the presence of a milder UV background are probable candidates for $z = 6$ SMBHs.
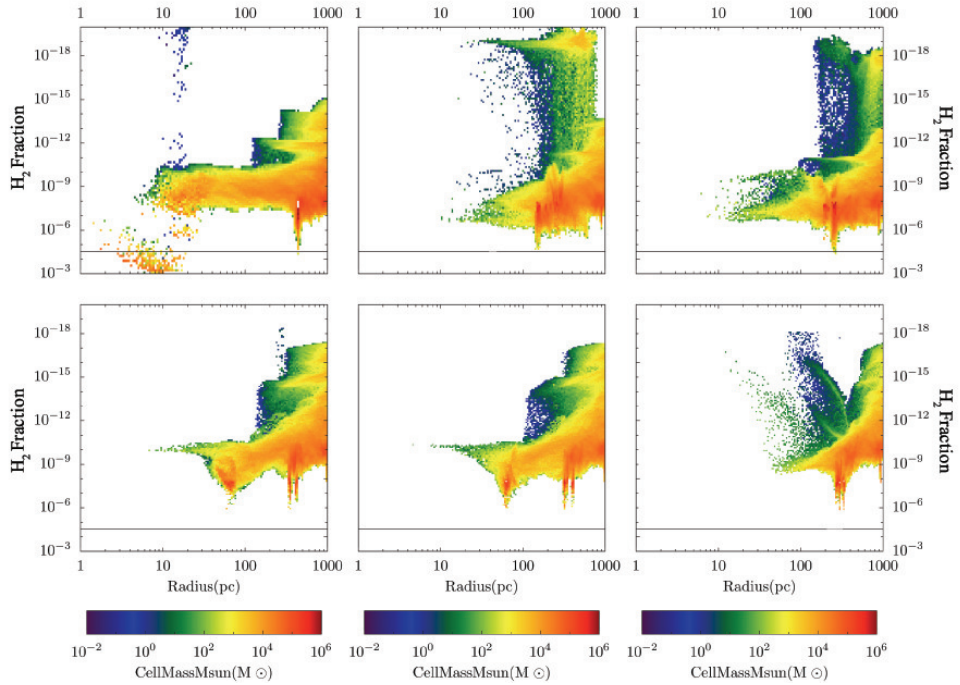
Figure 4 – 2D profile of H_2 fraction with respect to radius for the BG_5 (top) and BG_3 (bottom) cases at $z = 14.95$ (left), 14.86 (middle), 14.78 (right).
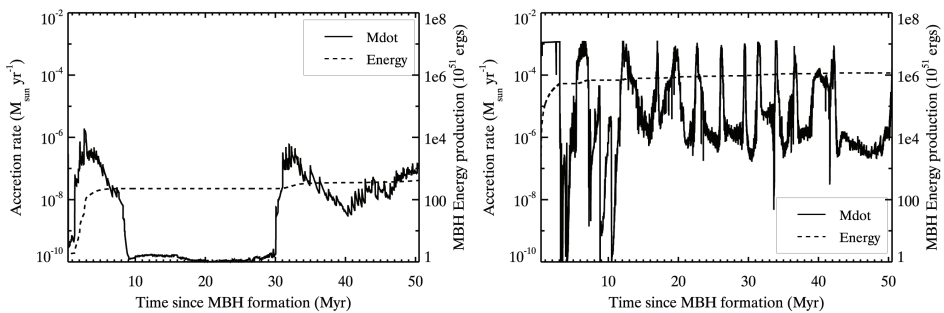

Figure 5 – Accretion rate and the corresponding total energy production of the central MBH over time for the BG_5 (left) and BG_3 (right) runs.
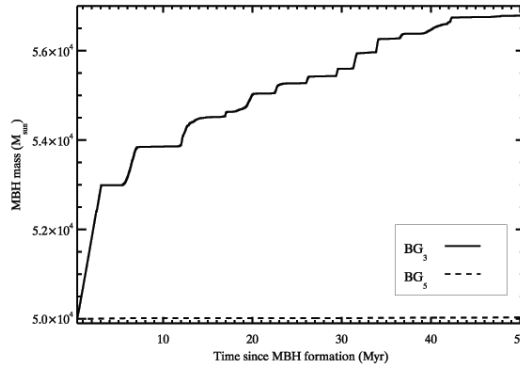
Figure 6 – Growth of the central black hole for the BG$_5$ (dashed line) and BG$_3$ (solid line) cases.

In this thesis, we make a step forward in understanding the nature of the universe and the pathways that lead to the formation of SMBHs in the early universe. However, there are still many open questions: Is it also possible to form these SMBHs through stellar seed black holes?, How common are these direct collapse black holes?, How do the relative contributions of AGN and SN feedback on the host galaxy evolve through time? What drives the observed Magorrian relation? In the near future, we are planning to perform simulations with stellar seed black holes including the X-ray feedback effect. Moreover, in order to find out how common this direct collapse black hole scenario is, one can run simulations with much bigger box sizes (100 Mpc/h) with high enough resolutions to resolve X-ray physics. Also, we should perform these high resolution simulations until z $= 2 - 3$ to address the underlying physics of the observed Magorrian relation and the interplay between AGN and SN feedback. In the next few decades, with new observational techniques and instruments, and increasing computational power, we will have an opportunity to have a glimpse at the earliest moments of the universe, which will enlighten us about its nature. This will enable us to test the existing theories and our current understanding of the universe. As sir Arthur Eddington says: "We should be unwise to trust scientific inference very far when it becomes divorced from opportunity for observational test".

Acknowledgements

Here we go, I finally made it to the point where I can thank the passengers of my last 6 years in Groningen. Some of these passengers now became permanent residents and some others were passing by. But both have made my years in Groningen a unique experience. I sincerely thank all of you!

Marco, in August 2007, early in the morning, I came to your office to ask If I could do my master project on the feedback effects of the first stars with you. You accepted of course ;), which resulted in 5 years of very nice collaboration and friendship. Both scientifically and personally, it was very educational and joyful for me. Thank you for encouraging me to develop my own scientific questions, and for letting me do so. I have realized that with seniority there is a big danger of becoming conservative about new ideas, however you retain your open mindedness. You are an inspirational scientist and an extraordinary person, and I feel privileged to have started my astronomy career with you. Thank you for all the discussions we have had about the nature of the universe and the world. I hope to continue collaborating with you and that we keep on counting together along with nature!

Wilfred, one of the oldest ISM group members, and my bro. It was more or less 3 years ago that we started hanging out together. We traveled to Australia, Chile and Japan together. The trip to Australia was fantastic from the beginning till the end, where we were almost missing the connecting flight from Singapore. Although we had like 5 hours in between the flights, due to consumption of quite a bit of Japanese whisky, we delayed the flight slightly. But hey, we ran and managed to catch the plane. I really am proud of you, how fast you could run under those conditions ;). Driving in the middle of nowhere in north-east Australia, sometimes confusing the lane, sometimes turning off the lights to enjoy the night sky and hunting for crocodiles, having a trip to the bushes with aboriginals were 'uitstekende' experiences. Of course the journey to Australia was not the only one that we were almost missing a flight, since Pisco is as good as whisky at that. Nevertheless, it was hell of a lot of fun traveling the world with you. I appreciate all your attempts to educate me, poor theoretician, with observational astronomy and introducing me to the wonders of single malt Scotch whisky. Hope to find other chances in the future to have new adventures. Cheers mate!!!

My salsa, football, tennis, go kart, sushi, ISM partner, and piano teacher, JP. Hmm , it looks like we have a lot in common. One more thing, we both like eating vegetarian cows ;), occasionally vegeterian JP. I do not know from where you find

the energy to do all those things, despite your age ;). I must say our Salsa dance course was an interesting experience. Since we were discussing half of the time how you must be leading me rather then dancing like others ;). We went to Rio de Janeiro together where we had a couple of days holiday in sunny Buzios. I remember enjoying pineapple caipirinhas and coconut milk. We had long nights together discussing various issues in Groningen. I feel lucky to have you as a friend. Thanks for all mental coaching, massages and fun. BTW, we shall finish our project and you should teach me how to play the rest of the song on the piano.

Hola Antonela! You are one of the persons who I have known from the beginning. The dinner occasions at your place like cooking kitchen in the chicken ;), your delicious strawberry tart, alfajores and of course empanadas, all yummy and famous Poker nights!!! We traveled to Turkey together, where they know you as Angelina, my dear friend! Also, we shared a house where your mother also joined us for a little while. Your mother Nora is a great person. She is full of joy and such an easy going person. Despite the fact that I do not speak a common language with you Nora, it was a lot of fun having you in Groningen. Many memorable moments. We run together, we laugh and cry together, and I am sure we will continue sharing moments and life independent of the geographical distances.

Facundo, you are absolutely the king of PES. The gatherings that we had at your place to play PES, just so you could kick our ... , which lasted till early in the mornings, were a lot of fun. Also, if you had not taken the initiative to organize it we would not have been playing real soccer every Sundays. You are a true River Plate fan. I am also grateful to you and Antonela for bringing me the official Argentinian T-shirt with my name on it ;))). I always enjoyed your company, I am sure we will stay in touch and hope to see you soon.

Ciao Paolo, you see I already speak Italian ;). You are a really nice, open minded and relax person. I always enjoyed your delicious Italian food, discussing various topics about the world and cultures, playing soccer and having long nights in de Minaar. I also would like to thank you and your family for hosting me at your place in Cagliari. I had a fantastic time.

Mirjam, you are one of the few non-astronomers whom I hanged out with in Groningen. I am sure every now and then I bored you with my fantasy world of Astronomy and hence I would like to thank you for your patience. It was a life experience running with you and Antonela together. Discussions of how to run and gossip during the runs showed the multi-task nature of women and were a lot of fun. Thank you for everything.

Sofietje, you are such a cute, joyful little girl who brought love not only to your parents but to all of us. I always enjoy spending time with you: playing in the sand, dancing, reading books. I also thank you for teaching me Dutch. I hope to see you grow and wish you the best in life.

Boris, you are such an enthusiastic person. Your passion for Astronomy and cars are known by everyone. I thank you a lot for educating me about the cars. It was a lot of fun discussing F1 results on Monday mornings. Thank you a lot for organizing the Go-kart events even though you were beating us every time.

I also remember one night picking up a telescope and going to the park in the south, in a very cold Groningen night! We could not stay long but it was worth it. Also, we went to Spa together which was an amazing experience. I know now how beautiful the Ferrari engine sounds!!! Thanks a lot man, and let me know if you want to go to *Monza* in the coming 2 years!

Burcu, I met you in my last 3 years of PhD and especially in my last year we got closer. You have an adventurous spirit and I enjoyed a lot trying your inventional cocktails, food, cakes, etc... I am grateful for all your all efforts trying to keep me social in my last year. We had some fun nights together hanging out in downtown Groningen right ;))). Thank you for feeding me and listening to my adventures with Enzo during the last couple of months. I wish you the strength, patience and luck for the rest of your PhD.

Christian, my office mate. Although, I joined in the last 2 years of your PhD, we get along quite well and I enjoyed sharing the office with you a lot. We had many enjoyable discussions about the issues of our PhD and life. You are also one of the F1 fans at the institute, as being from the country where 7 times winner of F1 is from, that was expected of course. Thanks a lot for introducing me to the various German beers and being such an enjoyable person.

Seyit, we only have 1 year difference in our PhDs and we are both members of the great ISM group. You are a really nice person. Thank you a lot for helping on all the defense procedures and everything.

Yang-Shyang, thank you for enligthening me with your Taiwanese culture. The sushi event, new years eve, glühwein, and carcassonne nights at your place were a lot of fun. I also thank you for introducing me to the piano and hope to stay in touch with you in the future.

Giamba, another ISM group member and soccer fan (fanta soccer!!!). Thank you a lot for arranging my holiday in Sardinia last year. I had an amazing time there with your friends Alessio and Michela. I enjoyed all your teasings and replied as such. You are about to finish and soon you will be writing your own acknowledgements hence I shall behave here although it is really tempting to tease you here. I wish you the best further and hope to see you in Italy.

Andrea, you cook the best brownie I have ever eaten. Thank you for helping me with all the Italian bureaucracy to get a visa. Thanks for all the fun time we had playing soccer and go-kart. I wish you the best.

Teresa and Oscar, thank you for teaching me how to cook Paella and giving me a proper Paella pan. I enjoyed a lot the Barcelona events at your place and all the food you guys cooked. Especially, the serrano ham (an actual pig leg) was fantastic. Thank you for keeping me social at the end of my PhD.

I would like to thank the secretaries and the computer group: Hennie, Jackie, Gineke, Lucia, Wim, Eite and Martin. Especially Hennie, Jackie and Wim. Hennie and Jackie, thank you for helping me every time with all the paper work, being such an easy going and practical people. You guys are a fortune for the institute. Wim, you were always there whenever I needed something, taking care of my health. I wouldn't manage to finish my PhD without your help. You are also my

greatest football fan. Thanks for coming to my matches and cheer for me. And I am happy that you finally got the correct coffee mug!!!

My office mates, Oscar and Patrick. Thank you for keeping the office silent and for your understanding to my loud music which was causing me a heart attack a couple of times. I wish you luck for the rest of your PhDs.

Drs Vijfje, de indoor voetbal club waarvoor ik 2 jaar heb gespeeld. Ik bedank alle leden van Dames 1 dat ze me hebben opgenomen in hun team ondanks mijn leeftijd en mijn gebrekkige Nederlands. Ik heb heel veel plezier gehad aan het samen voetbal spelen en het was een verhelderende ervaring om met Nederlandse niet Astronomen om te gaan. Allemaal bedankt!

Esra, we started the PhD about the same time, so you are about to finish and writing your own acknowledgements as well ;). Thank you for your company late at night at the institute and AH breaks. You are a really brave person. I cannot imagine myself finishing a PhD and have a baby at the same time along with other things. Good luck with everything.

Umut, I knew you from Ankara but only in Groningen we got close. It was really nice staying till late at the institute during our Masters. Sometimes we went out to the balcony to stare at the night sky, most of the time it was cloudy though, and later going into the city to have fries to get over the hangover we had from working till late or watching the beautiful sky. These were really nice times.

I would like to thank all the members of the ISM group. It was always educational for me, as a theoretician who runs cosmological simulations of the high redshift universe, to attend our bi-weekly meetings which was accompanied by delicious chocolates and cakes. It was also a lot of fun to have regular ISM dinners every year. Thank you all!

Kyle, you are such a pleasant person. You are one of the regular Sunday afternoon soccer players and an enthusiastic Salsa partner. I hope to see you at the dance floor at my defense party as well!!!

Peter, Paythor, Pitir!!! You are the one who I spent the most time with in these 6 years in Groningen. We shared a house and life for a long time. I must say you have a very different humor. Even for me it took a long time to get used to it. You are a fun person and we had a great time together. I do appreciate everything you have done for me. Thank you for being there for me every time I needed. Thank you for being you...

Matias, Matthijs, Thomas, Teffie, Stephanie, Edo, Alicia, Stefania, Beike, Germán, Carlos, Linda, Guliana, Idil, Koshy, Elif, Christoph, Dave, Parisa, Jelte, Niko and many others that I am forgetting now, I am happy to know you all and thank you for all the fun moments we had together in many different occasions!

After writing this fairly long acknowledgement I realize one more time that I had a great time in Groningen. I feel really lucky and thank you all once more for making Groningen my home.

Ayçin Aykutalp
August , 2012